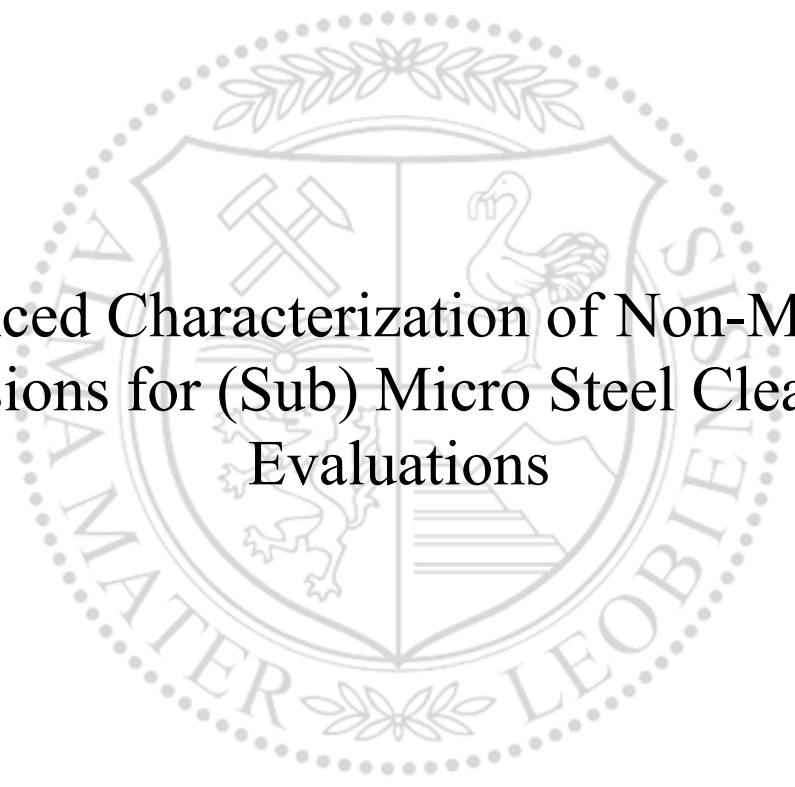




Chair of Ferrous Metallurgy

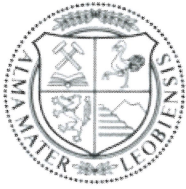
Doctoral Thesis



Enhanced Characterization of Non-Metallic
Inclusions for (Sub) Micro Steel Cleanness
Evaluations

Dipl.-Ing. Alexander Mayerhofer, BSc

May 2021



AFFIDAVIT

I declare on oath that I wrote this thesis independently, did not use other than the specified sources and aids, and did not otherwise use any unauthorized aids.

I declare that I have read, understood, and complied with the guidelines of the senate of the Montanuniversität Leoben for "Good Scientific Practice".

Furthermore, I declare that the electronic and printed version of the submitted thesis are identical, both, formally and with regard to content.

Date 03.05.2021

A handwritten signature in blue ink, appearing to read 'Alexander Mayerhofer', written over a horizontal line.

Signature Author
Alexander Mayerhofer

Preface

Since being a child, I have been fascinated by worlds invisible to the eye but explored by microscopes or telescopes. By the fact of metallurgy uniting invisible microstructures determining material properties and impressive production environments, dimensions, and temperatures, at the moment, my enthusiasm for metallurgy is culminated within this PhD thesis. For me, it's simply fascinating, that when utilizing extensive metallurgical knowledge you have the possibility to evaluate sub-micrometer inclusions to deduce production conditions of hot products which could potentially weigh tons.

First and foremost, I would like to thank my thesis advisor Susanne Michelic. Over the last years, she always helped me out with advice and giving me room for my scientific approaches realized in the thesis. I also want to thank Professor Helmut Clemens for his discussions about precipitations and physical metallurgy. Furthermore, I want to express my gratitude to the colleagues at the Chair of Ferrous Metallurgy and its professors Johannes Schenk and Christian Bernhard for being critical and inspiring discussion partners at any time. Special thanks to Bernd Lederhaas and Gerhard Wieser for their constructive feedback forming the basis of my judgement for microstructures, statistics and measurement accuracy; to Jan Piskernik for contributing to the present thesis through his ambitious problem solving ideas. Special thanks to my colleagues and friends Philipp Dorrer, Michael Zarl and Nora Fuchs, thank you for our lunch break "off-topic talks" and sharing your time at "moonshine-engineering" and complaining about life's frustrations. Cheers to my friends of the Leoben Party Squad for not taking things too seriously after sunsets.

Furthermore, I am grateful for my parent's belief and their encouragement. Christina, thank you for your support, your appreciation of long days, busy weekends and loving me as sometimes bad-tempered scatterbrain and a man always searching for reasons.

Abstract

A central part of research and development in metallurgy are analyses of steels' microstructure and containing phases. Due to ever-increasing demands on steel cleanness, the evaluation of endogenous and exogenous non-metallic phases with decreasing sizes is more and more important in research and industry. The current thesis deals with the limits and potentials of scanning electron microscopy and energy dispersive spectrometry (SEM/EDS) of non-metallic inclusions (NMI) to handle future demands on inclusion analytics. Comprehensive literature research of different approaches for steel cleanness evaluations and particle analysis reveals SEM/EDS as one of the most essential measurement systems for steel research and secondary metallurgical process development. Constantly improving image resolution and detectors' accuracy enables a wide range of chemical and morphological information of non-metallic inclusions.

A thesis's main task is to develop sound guidelines for a standardized inclusion detection and instructions for interpreting manual and automated SEM/EDS measurements in steel cleanness demands. Besides the influence of fundamental physical phenomena on the result, data post-processing and interpretation limits are discussed. The Potentials of SEM/EDS analysis are elaborated and summarized, leading to different approaches, guidelines, and innovative evaluation methods. Electron interaction simulations are used to better understand X-ray interaction volumes in non-metallic inclusions. As one result a particle size-depending mathematical model of the theoretical information share of matrix and inclusion composition is established. Comparing simulation of performed analysis and measurements, the potential of digital approaches dealing with metallurgical research problems is shown. A guide to manual point measurements and methods of electrolytic and chemical extraction are described to optimize SEM/EDS analysis experimentally. With the correct application of the procedures shown, composition and morphology evaluations, including matrix element contents in particles down to 300 nm in size, can be realized. First non-metallic inclusion standard samples for metallurgical demands are produced. To determine the iron content falsification at

automated inclusion analysis, reference and standard samples are correlated, resulting in 80 % Fe overestimation for 0.3 - 0.5 μm sized inclusions. Additionally, a mathematical correction of matrix interaction based on standard and reference samples has been developed to improve particle analysis's general output and evaluate particles' Fe contents at steel cleanliness evaluations. Furthermore, in addition to a new morphological categorization method, a size-dependent and direction-independent cluster identification method is developed based on inclusions' morphology and position data of automated measurements. This methodology of morphological particle evaluation and categorization can be applied to all inclusion classes of all product types. The work concludes with a guideline for proper correction, classification, and typification of typical non-metallic inclusions at steel cleanliness evaluations. The particle categorization methodology, defined as objective as possible, can be used to develop, evaluate and interpret particle populations or detailed analyses of specific metallurgical issues.

Finally, the application of data evaluation and interpretation is demonstrated using various industrial samples. The interpretable result of measurements is optimized and improved by enhanced data correction and evaluation. The potential of properly evaluated automated analyses is shown and discussed. By basic treatment of SEM/EDS - analytics in metallurgical applications, further knowledge is generated leading to an essential work for future research projects and industry developments.

Kurzfassung

Die Analyse der Mikrostruktur von Stählen und den darin enthaltenen Phasen ist ein wesentlicher Aspekt in Forschung und Entwicklung der Metallurgie. Durch immer höher werdende Anforderungen an die Stahlreinheit tritt die Detektion endogener und exogener nichtmetallischer Einschlüsse (NME) für immer kleiner werdende Partikel in den Vordergrund. Die vorliegende Arbeit beschäftigt sich mit den Grenzen und Möglichkeiten von Rasterelektronenmikroskopie (REM) und energiedispersiver Röntgenanalyse (EDX), um zukünftigen Anforderungen an die Einschlussanalyse gerecht zu werden. Eine umfassende Recherche verschiedenster Methoden der Reinheitsgrad- und Partikelanalyse zeigt die REM/EDX - Analyse als eine der wichtigsten Messmethoden für Stahlforschung und sekundärmetallurgische Prozessentwicklung.

Die Hauptaufgabe dieser Doktorarbeit ist es, fundierte Richtlinien und konkrete Anleitungen zur standardisierten Detektion und objektiven Interpretation von manuellen oder automatisierten REM/EDX-Messungen zu liefern. Die vorliegende Arbeit beschäftigt sich im Detail mit den Auswirkungen grundlegender physikalischer Phänomene auf Messergebnis, Datenbearbeitung und Interpretation. Mit Hilfe von Elektronen-Interaktions-Simulationen werden Röntgen-Interaktionsvolumina in nichtmetallischen Einschlüssen besser verstanden und die Datengenerierung bei der EDX Messung evaluiert. Ein Ergebnis ist die größenabhängige mathematische Beschreibung der Informationsverteilung zwischen Matrix und Einschluss. Erstmals wird ein digitales Abbild einer automatisierten Partikelanalyse kreiert und mit tatsächlichen Messungen verglichen. Es zeigt, welches Potenzial in der digitalen Behandlung von Problemen steckt und wie in Zukunft Phänomene der Stereologie untersucht werden können. Um die REM/EDX-Analyse versuchstechnisch zu optimieren, sind Leitfäden zur manuellen und automatisierten Analyse, sowie Methoden der elektrolytischen und chemischen Extraktion definiert, sie ermöglichen die Quantifizierung von Zusammensetzungen inklusive Matrixelementkonzentrationen für Partikel bis 300 nm Größe. Zur Bestimmung der Eisengehalte von Partikeln bei automatisierten Schlißanalysen, wurde

eine Methode entwickelt, die erstmalig Einschluss-Standards und Referenzproben erzeugt. Durch gezielte Korrelation von Schliff- und Extraktionsproben ist es möglich auf die entstehende Matrixinteraktion bei Partikeln von 0.3 - 0.5 μm auf 80 % zu quantifizieren. Zusätzlich ist durch die mathematische Beschreibung der Elektroneninteraktion eine Korrekturformel für den Matrixeinfluss bei automatisierten entwickelt worden. Basierend auf den Morphologie- und Positionsdaten von automatisierten Einschlussanalysen wird neben einer innovativen Methode der morphologischen Kategorisierung, eine größenabhängige und richtungsunabhängige Clusteridentifikation beschrieben. Diese Art der Auswertung und Kategorisierung der Partikelmorphologie kann erstmalig auf Einschlussklassen aller Produkttypen angewendet werden.

Abschließend wird in der Arbeit ein Leitfaden zur richtigen Korrektur, Klassifizierung und Typisierung nichtmetallischer Einschlüsse für Reinheitsgradbeurteilungen von Stählen vorgestellt. Richtige Dateninterpretation wird anhand von verschiedenen Industrieproben gezeigt und das Potenzial korrekt ausgewerteter automatisierter REM/EDX-Partikelanalysen diskutiert. Durch die grundlegende Aufarbeitung der Analytik bei metallurgischen Fragestellungen, konnte wichtiges Wissen generiert und Vorarbeit für andere Experimente geleistet werden. Gerade im Bereich der Entwicklung neuer Datenkorrektur- und Auswertemethoden ist ein großer Schritt zu noch besseren Ergebnissen erfolgt. Zukünftige Untersuchungen in nahezu alle Größenbereichen und in allen Stahlprodukten werden von den beschriebenen Herangehensweisen profitieren.

Content

Preface	I
Abstract	II
Kurzfassung	IV
Content	VI
1 Introduction	1
2 Methods of Inclusion Characterization	4
2.1 SEM/EDS in General.....	7
2.2 Application of SEM/EDS for Steel Cleanness Evaluations.....	9
2.3 Extraction extending the performance of SEM/EDS analysis.....	14
3 Phenomena and Potentials of SEM/EDS Analysis	17
3.1 Topography Causing Adsorption of X-rays	17
3.2 Influence of Inclusions' Cutting Position on the EDS data	19
3.3 Image Recording Influencing Detected Data.....	20
3.4 Automated Peak Identification Limiting the Interpretation of the Data.....	22
3.5 Scanning Parameters Influencing the Detected Iron Content	23
3.6 Inclusion Morphology, Clusters, and Strings Identified by Automated SEM/EDS Analysis	25
3.7 Improvement Potentials in Non-Metallic Inclusion Analysis	26
4 Solution Approaches for Improved Inclusion Analysis	28
4.1 Holistic Consideration of NMI Formation During Experiments	28
4.2 Simulation of Electron Interaction and X-ray Generation	30
4.2.1 X-ray Interaction Volume in Varied NMI Types	31
4.2.2 Simulation of X-ray Interaction of Different Inclusion Depths in an Iron Matrix.....	32
4.3 Digital Simulation of Automated Inclusion SEM/EDS Analysis.....	35

4.3.1	Description of Simulated Automated Steel Cleanness Measurements.....	35
4.3.2	Simulated SEM/EDS Analysis in Comparison to Performed Measurements.....	38
4.4	Consideration of X-ray interaction for single-point analysis.....	40
4.5	Inclusion Extraction Enabling Matrix-Free EDS Analysis	43
4.5.1	Electrolytic Extraction Applied to (Fe,Mn)oxides	44
4.5.2	Chemical Extraction Applied to Heterogeneous Oxy-Sulfide Inclusions	45
4.5.3	Twinjet-Polishing Performed as an Additional Dissolutive Preparation.....	49
4.6	Production of Inclusion Standard and Reference Samples Enabling Quantification of Matrix Interaction	50
4.6.1	Sample Selection, Including Thermodynamics and Kinetics.....	51
4.6.2	Production of Non-Metallic Inclusion Standards for Fe Quantification	53
4.6.3	Evaluation of NMI Standard Samples.....	54
4.7	Matrix Correction for Automated Inclusion Analysis	60
4.7.1	Interaction-Ring Correction.....	61
4.7.2	Interaction-Depth Correction	64
4.7.3	Iron Correction Applied to Research Samples with varied Fe Content.....	66
4.8	Morphology Categorization using M-Factors.....	68
4.9	Evaluation of Inclusions' Spatial Distribution.....	72
4.10	Implementation of gained knowledge by FET development and improvements	75
4.10.1	Correction of Artefacts.....	76
4.10.2	Classification Depending on Non-Metallic Partner	77
4.10.3	Typification for Metallurgical Steel Cleanness Evaluations.....	79
4.10.4	Data Representation and Interpretation	80
5	Implementation of Improved Steel Cleanness Evaluations for Industry Demands	83
5.1	Chemical Classification and Typification Beyond Standards.....	84
5.2	Morphological Categorization.....	88
5.3	Quantified Spatial NMI Distribution	90
5.4	Iron Correction at Industry Samples	92
6	Conclusion and Outlook	95
	Bibliography	98
	Acronyms.....	112
	List of Parameters	114
	List of Tables	116

List of Figures 118

A Appendix 122

A.1 Data correction for carbide steels 122

A.2 Morphology Parameters 122

A.3 SEM/EDS Parameters 123

A.4 Casino Simulation 124

1 Introduction

Over 100 years after A. McCane's [1] publication, non-metallic inclusions (NMI) are more than ever in the focus of ambitious metallurgical scientists and researchers. The share of these small particles in a steel's microstructure, often not visible in metallurgical considerations, can reach remarkable amounts. Considering a total oxygen content of 50 ppm entirely bonded to aluminum after deoxidation theoretically results in 10^7 spherical inclusions with 3 μm diameter. Therefore, steel can be seen as composite material of matrix and particles [2], and the relevance of improved metallurgical melt management is obvious. In the early 20th century, the first publications dealing with steel cleanliness were driven by investigations of particles' origin, behavior, and their influence on steels' mechanical properties [1,3–5]. With the continued development of high-performance applications for steel, accompanied by increasingly complex production routes, more research fields [6–10] dealing with steel cleanliness evolved. NMIs' number, size, distribution, morphology, and chemical composition, whether originated exogen (refractory or slag entrapments) or endogen (products of steel treatment), can, directly and indirectly, be correlated to the steel performance. On the one hand, negative effects often caused by large or clustered particles at unfavorable positions can provoke process instabilities like nozzle clogging during continuous casting [11–13], reduced fatigue strength [14–16], fracture initiation [17–20], worsened hot ductility [21] and minimized corrosion resistance [22,23]. Whereas, on the other hand, positive effects, including increased toughness [24], grain boundary pinning [25,26], acting as favored nucleation sight [27,28], or enabling better machinability [29,30] can be achieved with randomly dispersed inclusions of defined chemical composition and size. In general, low inclusion numbers are beneficial for most applications by reducing the probability of single large particles causing material failures. With higher mechanical loads, the required steel cleanliness level often increases. According to the literature [10], maximum permitted inclusion sizes vary from 150 μm for structural steel to 25 μm in spring steels, continuously decreasing in wire or bearing steels, down to 1 μm limits for aerospace demands. To fulfill product requirements, total oxygen contents are kept as low as possible to reduce the probability of single large inclusions. An in-house micro

cleanness evaluation ($NMI > 1\mu\text{m}$) showed particle contents of 500-1000/mm² in construction steels, about 250/mm² in spring and railways steels, and 50-100/mm² in micro-alloyed or austenitic steels. Remelted grades range in NMI contents of 1-10/mm². Required steel cleanness always depends on the application, especially considering particles' chemical composition. Realizing the unavoidability of non-metallic inclusions and considering the potential of adjustment to less harmful or even positive influences on the material properties, the term oxide metallurgy was first mentioned in the 1980s [31], describing the enhanced modification of non-metallic inclusions for special purposes. This led to modern steel production based on thermodynamic and kinetic models predicting and considering segregation, formation, and separation of non-metallic phases [32–49].

As published by Kaushik et al. [50], research, development, and problem solving are complex and more stage processes. Key factors of metallurgical research including process and product improvement are based on a synergy of theory postulation, model creation, and reliable analysis. In non-metallic inclusion analysis, different inclusion detection and characterization approaches are used in industry and research, primarily focusing on scanning electron microscopy and energy dispersive spectrometry (SEM/EDS). For example, published guidelines and particle evaluation rules of industry are generally formulated for specific products, e.g. flat products with particular deformation degree and can't be transformed directly to other samples. The general lack of objective guidelines and explicit non-metallic inclusion standards for micro and sub-micro steel cleanness evaluations are one of the decisive drivers behind this work. An unbiased categorization and interpretation guideline needs to be given by excluding the subjective influence of operator or researcher expectations. According to the ongoing digitalization of steel production, correct interpretation of this data will be directive for metallurgical improvements. Affordable and faster SEM/EDS detector technology will further increase its application in industry and research. Strict process times leave hardly any time for fundamental considerations of inclusions composition or extensive manual analyses. Therefore, there will be an increased need for data post-processing and interpretation guidelines of automated analysis in a most efficient and easily adaptable way. Current standards do not fulfill these requirements. With the increasing needs of smaller particles analyzed due to decreasing particle sizes in high-performance products, an improved understanding of electron and X-ray interaction is necessary for correct interpretations. With decreasing inclusion diameter, unavoidable matrix interaction needs to be dealt with at composition analysis, being essential for metallurgical demands.

The present work deals with various approaches to further improve non-metallic inclusion characterization with special focus on SEM/EDS analyses. The potential of enhanced

evaluation is demonstrated in different research and industry tasks. Chapters 2 and 3 describe the general acquisition of inclusion characteristics focusing on SEM/EDS analysis's measured values as a key device for modern inclusion analytic. Accuracy of EDS systems at current measurement circumstances compared to standard values is in the main focus to further improve the measurements systems understanding. Starting with a general overview on various influencing parameters on inclusion population, Chapter 4 leads to possible approaches for improved inclusion analytics. Theoretical concepts include fundamental considerations of electron interaction and non-metallic inclusions surrounded by steel. Digitally simulated automated measurements can be an innovative new methodology for the evaluation of different phenomena and parameters affecting the particles' EDS result in cross-section analysis. Cutting position, physical effects, or Fe-matrix interaction are discussed. Practical concepts dealing with the production of non-metallic inclusion standard samples can improve inclusion research in general. The application of defined particle production, electrolytic extraction, and development of a referencing methodology leads to quantification of iron contents in automated measurements. Additionally, a discussion of the general EDS output and improved data post-processing by mathematical correction of matrix interaction helps to generate improved analytical data. Developed new interpretation tools for innovative steel cleanness evaluations realize enhanced chemical and morphological particle classification. Fast and reliable inclusion evaluation is assured for present and future inclusion analytics, by easy to use data post-processing Matlab tools shown in Chapter 5. Concluding the works' main findings in Chapter 6, the gained knowledge concerning micro and sub-mirco steel cleanness evaluations will lead to new quality criteria for steels, improving the best possible output of automated inclusion analysis.

2 Methods of Inclusion Characterization

Several approaches [44,51–55] have been developed defining indirect and direct methods for inclusion characterization in the past decades. Indirect concepts, including total oxygen analysis and magnetism or eddy current related methods, are based on steel parameters correlated by thermodynamics or empirical data to the inclusion content. For example, bearing steel shall not overcome 10 ppm total oxygen content to significantly improve the oxide steel cleanliness and increase fatigue life. In general, indirect methods often leave room for interpretations, but they are still a good indicator of steel cleanliness changes during the production process. Direct methods have been developed to determine the size, number, shape, position or composition of non-metallic inclusions in steel samples products. The variety of systems caused by various physical approaches detect inclusions' parameters by image analysis, scanning electron microscope, pulse discrimination analysis, fracture-related methods, ultrasonic testing, laser and plasma techniques or cathode luminescence [50–64]. Mathematical approaches can be seen as indirect steel cleanliness determination based on directly measured parameters, including statistics of extreme values or generalized pareto distribution often used for theoretical considerations [65–67]. To apply adequate research and development, as many parameters as possible should be gathered during a performed analysis. Due to the great variety of non-metallic inclusions present in steel samples, particle composition's determination evolved to one of the essential parameters related to different metallurgical questions. For instance, the time of particle formation or current stages of their Ca-modification can be identified [68]. According to requirements in metallurgical research and enhanced industrial evaluations, the predominant direct methods evaluating steel cleanliness parameters in detail are summarized in Figure 1.

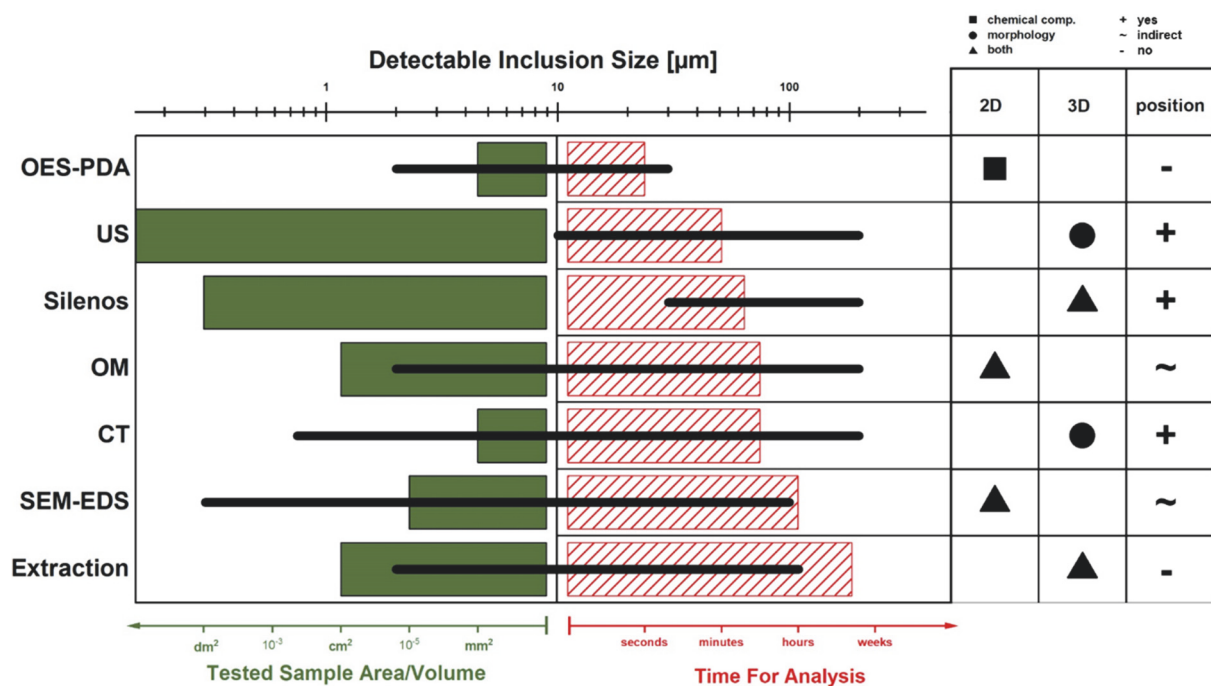


Figure 1: Most established instruments steel cleanliness evaluations.

The displayed characterization concepts have their specific application field due to different industry and research philosophies in measurement time, costs, and analysis resolution. According to literature research, detectable inclusion size, analyzed volume, and time effort depend on the used device and the set parameters. The main applied methods for inclusion characterization will be shortly explained and summarized in the following

- Optical emission spectrometry with pulse discrimination analysis (OES-PDA) determines particle composition and number during production. Lollipop samples taken, roughly machined and analyzed by spark analysis, enable detecting hundreds of non-metallic inclusions approximate composition within seconds. Detected sizes can be correlated to signal intensity of randomly measured inclusions in the micrometer size range without explicit information about morphology or position. For example, ongoing inclusion modification (Ca-treatment) can easily be monitored before tapping, based on the general particle composition changes. Due to the fast application giving an excellent general overview of particle populations in the melt, OES-PDA evolved to a standard analysis device in many steel plants [59,69–71].
- Ingot products with large dimensions often have the problem of large cavities or agglomerated non-metallic inclusions being crucial material inhomogeneities at unfavored positions. Ultra-sonic (US) evaluation enables defect localization and size estimation without necessary machining or sampling in minutes. Depending on product

size and particle position, defects in the meso and macro range are generally detected. Often a 100 % US quality check philosophy is realized at companies [72–74].

- Steel cleanness level-evaluation by a numerical optical system (Silenos) is a particle detection procedure analyzing defects $> 20 \mu\text{m}$. By removing $10 \mu\text{m}$ layers by CNC milling and additional particle analysis using a high-resolution scanner and laser spectrometer, three-dimensional steel cleanness evaluation is performed. Size, morphology, and exact position are determined and correlated to production. Influences of continuous casting machine parameters can so directly be linked to inhomogeneities in the product [75–79].
- The most widely used device of the last decades is optical microscope (OM) evaluation. In industry and research, most metallurgical discoveries and innovations are based on image analysis of micro-sections. Therefore many standards and key-values describing non-metallic inclusion characteristics have been formulated. Sample preparation is more time-consuming, but the general possibility of additional microstructure evaluation makes it an essential tool for researchers and steel producers. Due to simple image analysis, chemical compositions of inclusions are assumed by morphology and appearing greyscale. Particle positions in the product can indirectly be identified by comprehensible sampling [80–83].
- Computer tomography (CT) is a three-dimensional imaging tool. In general, non-metallic inclusions and cavities have a lower density than the surrounding steel matrix. Therefore, CT-detectors can image their position and morphology. Due to the problematic radiography of steel materials, CT scans can only be applied to thin-walled products [83–86].
- In the past 20 years, the probably most often used concept for particle analysis is scanning electron microscopy with energy dispersive spectroscopy detectors (SEM/EDS). Simple cross-section sample preparation enables the manual evaluation of microstructure and non-metallic inclusions with different detectors. Morphology and composition analysis can be performed at sub-micrometer to millimeter size regime, enabling a wide range of research and industry applications. Particle positions in the product are determined by position of the cross section sample. The application of automated inclusion analysis creates statistically comprehensible data of every single inclusion combining the benefits of impartial optical evaluation and a high number of detected features for statistically proven results at constant measurement conditions. Due to the wide range of possible information gathered, SEM/EDS is the state-of-the-art modern inclusion analysis device, although still significantly disadvantaged by its time effort [60,81,84,87–95].

- To further improve SEM/EDS analysis, electrolytic or chemical extraction can be applied to steel samples as an additional sample preparation step. Caused by different chemical or electrochemical potentials, the iron matrix is dissolved, and noble non-metallic inclusions are collected by a filtering step. After sputtering, these non-metallic inclusions free of any surrounding bulk material are analyzed by SEM/EDS. For fundamental research, extraction procedures have a high potential for the best composition and morphology evaluation of complex non-metallic inclusions [82,96–102].

2.1 SEM/EDS in General

Scanning electron microscopy has a broad field of applications, and its affordability makes it a widely used device. Regarding non-metallic inclusion analysis in steels, SEM/EDS systems' extensive benefits are evident. With feasible magnifications of 25x to 150.000x, modern scanning electron microscopes provide a broad resolution range for macroscopic ($> 100\mu\text{m}$) and sub-microscopic ($< 1\mu\text{m}$) evaluations. A variation of mountable detectors and software packages leads to an extensive information output. For qualitative and quantitative analysis, energy dispersive spectrometry (EDS) is an entrenched method to identify and quantify almost all periodic table elements. First suggestions of the high potential of EDS analysis can be found in literature in the early 1970s by Reed et al. [103]. Since then, technological developments in the microscope and detector technology have improved continuously. The performance concerning resolution, input-output counts, spectrum quality, low energy photon detection, quantitative analysis, and spectrum imaging of 3rd generation SDD detectors has been examined by Newbury et al. [53]. Analysis of non-metallic inclusions is done based on minor and trace element concentrations (Table 1), increasing the challenge of correct evaluations and interpretations for metallurgists.

Table 1: Constituent mass ratio classification [104]

Category	Mass fraction	Wt%
Major constituent	$C > 0.1$	$>10\%$
Minor constituent	$0.01 \leq C \leq 0.1$	1-10 %
Trace constituent	$C < 0.01$	$<1\%$

Today, EDS systems can quantitatively analyze soft X-rays (C, O, S, N) at the same level as wavelength dispersive spectroscopy (WDS). A disadvantage of EDS technology is the bad peak-to-background ratio resulting in higher limits for quantifying unfavorable element combinations, e.g., molybdenum and sulfur (for details see Section 3.4) [104–106].

If non-metallic inclusions are analyzed by EDS technology, two general measurement approaches need to be differentiated: standard-based and non-standard-based analysis.

The limits of quantification are determined by the magnitude of the characteristic signal level relative to the continuum. Therefore, for the best analytical results, the standard-based methodology is preferable. Each element analyzed in the unknown is compared to a reference standard, similar to wavelength dispersive spectroscopy (WDS). The application of mathematical corrections for physical analysis effects (ZAF-correction) is applied to consider how electrons and x-rays interact with the sample matrix of 2 compounds' materials [91]. According to the following Equation 1 and 2, the relative concentrations of the unknown and the standard (C_{unk}/C_{std}) is considered multiplicatively by the ratio k (X-ray intensity in the unknown (I_{unk}) and the standard (I_{std})), backscatter, and energy losses correlated to the atomic number (Z^a), primary x-ray generation and absorption during propagation through the material (A), secondary x-ray generation caused by inner-shell ionization by photoelectric absorption (F) and Bremsstrahlung or continuum radiation (c).

$$k = \frac{I_{unk}}{I_{std}} \quad (\text{Eq. 1})$$

$$\frac{C_{unk}}{C_{std}} = k * Z^a * A * F * c \quad (\text{Eq. 2})$$

A significant time and knowledge effort must be considered for composition analysis combined with the disadvantage of standards available for all elements measured in the sample material [91,107,108]. Due to manually performed analysis and complicated quantification of heterogenous-non metallic inclusions by standard-based analysis, steel cleanness evaluations are generally performed by more accessible non-standard-based analysis. Due to its faster application and better adaption changing measurement tasks, non-standard EDS is the primary methodology for modern inclusion analytics. Detectors are calibrated regularly, and element differentiation is performed by peak identification based on the detector distributor's software and databases (e.g., Oxford Instruments) comparing characteristic peak positions. Element quantification is performed by interpreting peak heights and shapes. Although an inferior quantification analyzing minor and trace elements need to be considered, comprehensible data evaluation and interpretation can still be realized by stoichiometric calculations. Figure 2 displays a relative error of +/-30 % to capture 95 % correctness (2013).

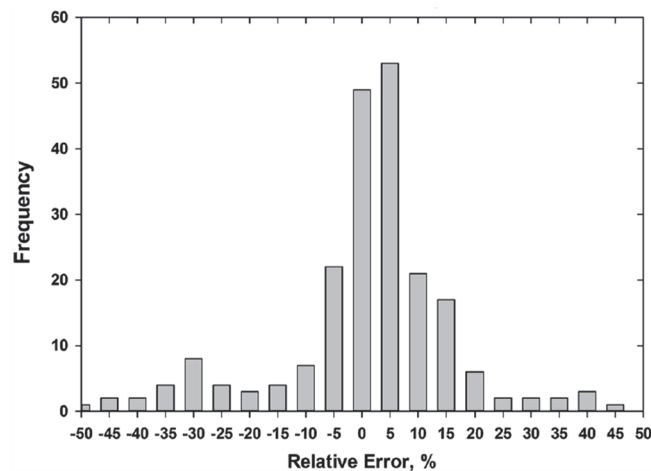


Figure 2: Relative errors at non-standard analysis [108]

According to Newbury et al. [108], the benefits of the faster method prevail: The majority of EDS results published globally are outcomes of non-standard measurements and affirm the excellent applicability. Additionally, result scattering can be compensated by measurement automation providing good statistics. Depending on the analysis's complexity, specific knowledge and experience in result interpretation are still needed. Additional and more detailed information dealing with the general functionality of SEM/EDS can be found in "Scanning Electron Microscopy and X-Ray Microanalysis" of Goldstein et al. [91].

2.2 Application of SEM/EDS for Steel Cleanness Evaluations

Representative sampling is probably the most crucial point for statistically reliable micro cleanness results. Before performing measurements, various parameters influencing particle formation need to be considered in data interpretation, e.g., time of formation, segregation, or cooling conditions (see Section 4.1). General measurement areas of 50-100 mm² support the method's validity by a large number of morphological and chemical inclusion data compensating single outliers. Depending on the sample's chemical composition and the expected inclusion population, sample preparation may need to be adapted, but usually, specimen preparation follows the listed metallographic approach by alternate washing:

- Embedding in conductive (Cu) material
- Grinding with 320-600-800-1200 mesh SiC-paper
- 9 µm diamond polishing for 7 min with hard cloths
- 3 µm diamond polishing for 7 min with hard cloths
- 1 µm diamond polishing for max. 1 min with soft cloths

About 3 bar and rotation speeds of ~130 rpm for the rotary head and 200 rpm for the rotary table are used for mechanical polishing. OPS treatment is not beneficial due to possible surface contamination with oxides and a chemical attack that may affect particles' compositions. If water-soluble inclusions are expected (e.g., CaS), grinding and washing should be performed with ethanol or glycol liquids. After a proper drying procedure, the sample can be mounted in the SEM. Remaining liquids on the surface or in cracks should strictly be avoided because evaporation during vacuum generation leads to heavy contamination of the SEM chamber. Recurrent contamination results in decreased image and measurement quality.

At the Chair of Ferrous Metallurgy, two scanning electron microscopes are in use. In addition to a tungsten cathode-powered FEI Quanta M200 primarily used for the analysis of non-conductive slag materials, a field-emitter-based JEOL 7200F is operated for high-resolution demands and steel cleanliness evaluations. In both cases, the software for detector control and data evaluation is provided by Oxford Instruments. The JEOL-Oxford system is equipped with:

- UED – upper electron detector
- LED – lower electron detector
- RBED – retractable backscattered electron detector
- EBSD – electron backscattered diffraction detector
- EDS – energy dispersive spectroscopy (X-Max80)

Figure 3 shows the JEOL7200F system at the Chair of Ferrous Metallurgy's laboratories illustrating the prevailing setup for inclusion analysis in the microscope. Oxford Instruments' Aztec software operates the different detectors and processes the generated information during measurements. Self-developed offline tools perform particle evaluations and interpretations.

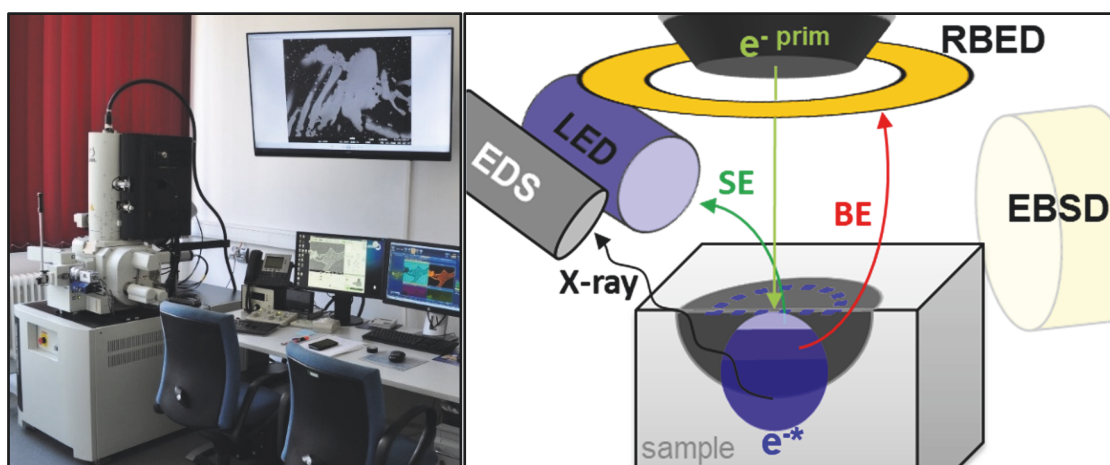


Figure 3: JEOL 7200F system and illustration of gathered information during NMI analysis

After the generation of primary electrons (e-prim) in the Shottky field emitter, the electron beam is accelerated and focused on the sample according to the defined voltage and emitter current. Elastic and inelastic impulse interaction of the electrons in the sample material (e^{*}) generates an interaction volume of spherical shape, describing the initial point of all information generated. Depending on the material properties, the e^{*}-bulb has diameters between 0.5 – 2 µm. For different information sources, the corresponding detector needs to be activated. Secondary electrons (SE) generated in the samples' first 10 nm [91] possess the lowest energy detected by the LED detector for primary imaging of surface structures. The RBED detector interprets medium energy interaction of backscattered electrons (BE) by a chemical contrast for depths' with approx. 200 nm [109], generally depending on the elements' atomic number. For steel cleanliness evaluations, this detector usually identifies non-metallic inclusions in steel at cross-section samples. Typical steel inclusions, e.g., Al₂O₃, TiN, CaO, or MnS, appear darker than the surrounding steel matrix enabling easy identification. At depths of approximately 1 µm [91,109], characteristic X-rays are generated and emitted. In the current setting, this emitted radiation is analyzed by the XMax-80 EDS detector and processed by the mentioned non-standard peak identification method using a database of various EDS spectra. After peak evaluation by the software, the X-ray intensity information is transformed to qualitative characteristic spectra and quantitative compositions of the analyzed volume. Shape and interaction of the information volume may differ depending on material properties, heterogeneity, and microscope settings [91,109,110].

In general, measurements can be performed manually or automatically. At manual analysis, the point of interest is defined by the operator's subjective identification criteria. Point or area analysis are performed at manually defined positions. Microscope and detector settings can be adjusted at any time. Manual analysis is generally used to get an overview or general impression of unknown samples. Especially for identifying material failures, fracture surfaces, or detailed particle analysis after automated measurements, including concentration mappings, manual EDS evaluations can lead to outstanding results.

At automated inclusion analysis, all microscope and detector parameters are defined once, and inclusion identification and measuring are performed software controlled by the system. The main parameters of the current setup are listed in Table 2. An extended list can be found in Appendix A.2, Table 20.

Table 2: Analysis parameters for micro cleanliness evaluations at the Chair of Ferrous Met.

beam energy	15kV
probe current	12 PC
working distance	10 mm
resolution	1'024×960 px
magnification	400x
min. particle size	9px
ECD range	1µm – max
measurement time	3 s
process parameter	4 PP

Feature identification is performed by defined greyscale threshold settings with respect to the surrounding matrix shown in Figure 4. There, the contrast and brightness of a reference image are quantified (green line in the image). The microscope settings should be adjusted until a mean matrix value of >24000 and a non-metallic inclusion value of <2000 is measured. By threshold definition of 20000 (red area), the identifiable greyscale values are defined. In the current setting, features with grey scales <20000 and sizes bigger than 1 µm are identified and subsequently measured for 3 seconds by the EDS detector.

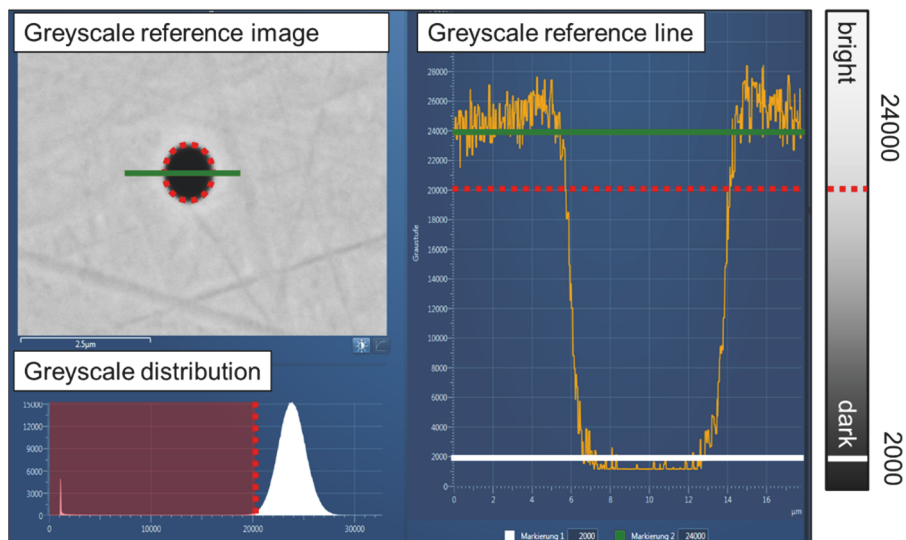


Figure 4: Greyscale quantification and threshold setting.

The resulting EDS spectra, quantified chemical composition, and morphological data are stored in the software. Thousands of non-metallic inclusions are detected in several hours without an operator needed [92,111–116]. Depending on the task, all measurement parameters can be optimized for more efficient analysis [117].

A disadvantage of the automated system is the misinterpretation of dark appearing features. These are polishing residues, scratches, and porosities, leading to inaccurate measurements. Post-processing steps dealing with the resulting data lead to statistically representative values. It is challenging to correlate correct non-metallic and metallic partners of the measured inclusions at data interpretation only by composition data. From a thermodynamic point of view, many different element combinations are possible. For instance, data including O, Mg, Al, S, Ca, and Mn as distinctive elements can be combined, resulting in different homogenous or heterogeneous possible non-metallic inclusions. Today only extensive manual analysis by generating detailed chemical composition mappings (Figure 5) can determine particle homogeneity, element combinations, or identification of solute matrix elements in inclusions. Theoretically, large size area mappings can also be used for particle identification during automated inclusion analysis. However, this needs further research and development regarding worse resolution and an extensive time effort [118].

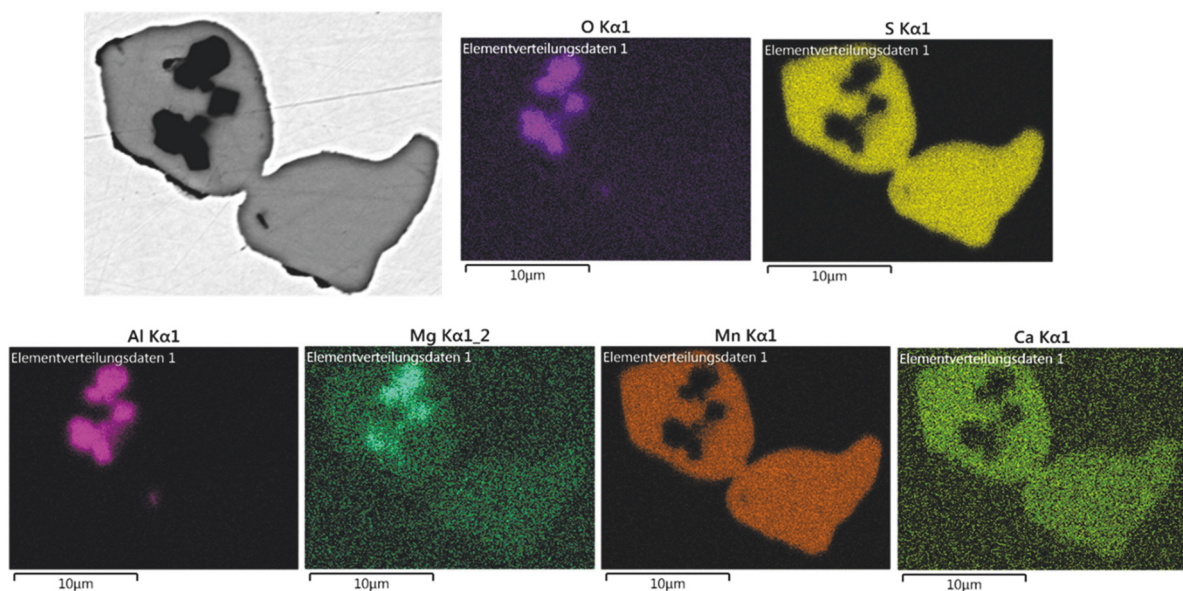


Figure 5: Concentration mapping of a heterogeneous (Al, Mg)oxide – (Ca, Mn, Mg)sulfide inclusion.

Reliable steel cleanliness evaluations are always based on a combination of automated inclusion analysis and supporting manual composition evaluations. Concentration mappings can help to gain more metallurgical knowledge and increase the quality of correct classification and typification decisions.

2.3 Extraction extending the performance of SEM/EDS analysis

For micro and especially sub-micro inclusion evaluations, matrix dissolution experiments can be applied to steel samples to practically avoid the appearing challenge of steel matrix interaction during EDS analysis. Using differential chemical and electrochemical potentials of non-metallic inclusions and the surrounding bulk material, NMIs can be separated from the steel matrix. As illustrated in Figure 6 quality and quantity of SEM/EDS results can be improved by better interaction bulb and particle volume ratio, especially at small inclusions.

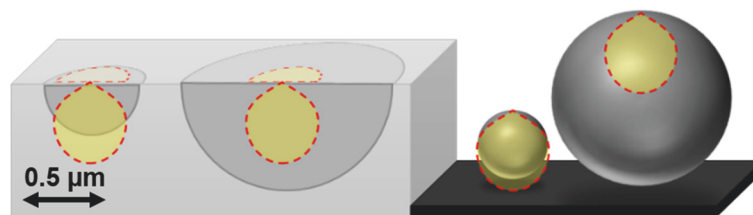


Figure 6: Comparison of electron interaction for cross-section and for extraction samples.

At dissolution experiments, two main parameters need to be considered: stability of the steel matrix and the general dissolution resistance of the exposed environment's targeted particles. As seen in Figure 7, strong acids cause an accelerated matrix dissolution compared to electrolytic extraction, tending to be a softer process. Depending on the research task, different amounts of a dissolved matrix are reasonable. Janis et al. [119] reported a compromise for the existing conflict depending on particle size, time consumption, matrix stability, and particle stability need to be found.

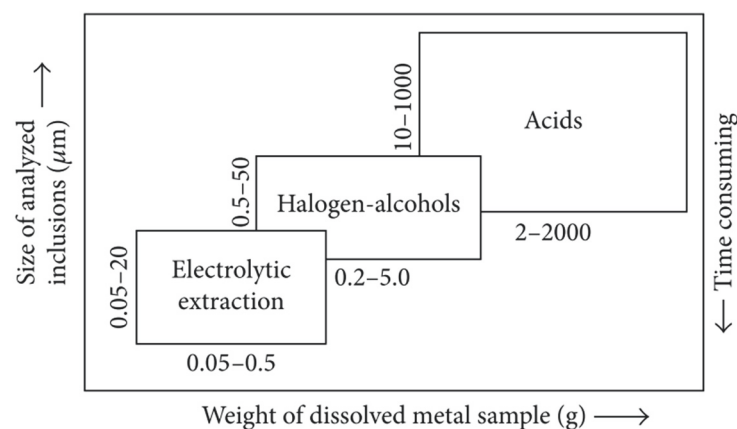


Figure 7: Different extraction methods for steels non-metallic inclusions [119].

To properly analyze inclusion in macro or meso size regime, a high amount of bulk material needs to be dissolved within a manageable time. Consequently, strong acids are often used for non-metallic phases with high stability [119,120]. Different dissolution rates for extraction applications have been evaluated in literature [119,121–124] based on the bulk material. Generally, steels' increased corrosion resistance results in more difficult extraction and more artifacts complicating subsequent analysis. With the application of higher concentrated acids at chemical extraction, possible changes in inclusions chemistry and morphology at the extraction process need to be considered and evaluated. Heterogeneous particles and easily dissolvable components as MgO, MnS, or CaS [125] can result in a transformed appearance of inclusion morphology and composition after extraction. Building upon a low anodic potential of ferrite matrix and higher potentials of non-metallic inclusions [124,126,127], electrolytic extraction is more selective and less aggressive. Increased extraction speed usually results in forced material dissolution (higher current density), creating more artifacts (e.g., iron and chromium chlorides). Subsequently, the remaining electrolyte, including non-metallic inclusions and noble intermetallic phases, is treated with consecutive filtration steps. After an optional sputtering procedure, particles can be analyzed in three-dimensional appearance in the scanning electron microscope. Reference measurements on cross-section samples are recommended to exclude possible influences caused by extraction [93]. In Table 3, electrolytes and solutions are listed, well-functioning for the isolation of various non-metallic particles.

Table 3: Electrolytes and non-metallic inclusions extracted for research demands.

Steel	Method	Medium	Extracted Non-Metallic Phase	Literature
low alloyed	elec.	46,25% urea; 53,75% chlorin chloride; dimethylformamide (1:10)	FeOMnO	[93]
		10% ammoniumacetate; 1% tetramethyl- ammoniumchloride; methanol;	MnS	[128]
		5% triethanolamin; 5% glycerin; 1% tetramethylammoniumchloride; methanol	MnS-TiN, MnS, Al ₂ O ₃	[128–130]
	chem.	nital 5% sequentially	MnS	[128]
med alloyed	elec.	2% triethanolamine; 1% tetramethyl- ammoniumchloride; bethanol; 0,05-0,2% Ba	MgO; MgAl ₂ O ₅	[125]
med-high alloyed	elec.	10% acetylacetone; 1% tetramethyl- ammoniumchloride; methanol	MnS, ZrO ₂ , Al ₂ O ₃ , AlN, AlON, MnAl ₂ O ₄ , Al ₂ O ₃ , AlN, AlON, MnAl ₂ O ₄ , Mn(S,Se)	[131–133]
high alloyed	elec.	10%HCl; 1% wine acid; methanol;	(Ti,Nb)CN	[43]
		2% triethanolamine; 1% tetramethyl- ammoniumchloride; methanol; 0.16-0.42% Ba	CeS, MgO, CaO, SiO ₂ , Al ₂ O ₃ , MgO, Ce ₂ O ₃ , CeO ₂ , ZrO ₂ , Ti ₂ O ₃	[133]
		4% salicyl acid ester; 1% tetramethyl- ammoniumchloride; methanol	ZrO ₂ , Ti ₂ O ₃ , Ce ₂ O ₃ , CeO ₂ ;	[134]
		40% maleinacidanhydride; 3% tetramethyl- ammonium; metahnl	Ti ₂ O ₃	[134]
	chem.	14% iod methanol	ZrO ₂ ; Ce ₂ O ₃ ; CeO ₂ ;	[134]
CWS	elec.	46,25% urea; 53,75% chlorin chloride; dimethylformamide (1:10)	(Cr,Mo,V,Nb)carbides	[135]
	chem.	90% HCl; 10% ethanol;	(Cr,Mo,V,Nb)carbides	[135]
HSS	elec.	46,25% urea; 53,75% chlorin chloride; dimethylformamide (1:10)	(Cr,Mo,V,Nb)carbides	[135]
	chem.	90% HCl; 10% ethanol;	(Cr,Mo,V,Nb)carbides	[135]

Various electrolytes and procedures were tested for the present work, leading to three methodologies redefined and improved for variable research tasks described in detail in Section 4.5. The main subject was to determine how accurately Fe content evaluations can be applied on extracted non-metallic inclusions and how the preparation method itself affects the EDS result's quality.

3 Phenomena and Potentials of SEM/EDS Analysis

During SEM/EDS analysis, many physical effects affect detected composition and morphology. In the present work, direct and indirect impacts of topography, surrounding matrix, imaging, scanning method, and data treatment are discussed.

3.1 Topography Causing Adsorption of X-rays

As indicated in the previous section, careful sample preparation is necessary for best measurement results [136,137]. Newbury and Ritchie [107] described the samples' general topography influencing propagation and generation of characteristic X-rays. In Figure 8, different adsorption paths in the analyzed sample are illustrated, affecting the elements' detection. Unevenness in the micrometer size range already causes adsorption variation of the emerging x-rays. According to Pistorius and Patadia [138], especially low-energy photons (below 5keV), which are essential for non-metallic inclusion identification (O, N, S), are sensitive to adsorption effects of unfavorable positions relative to the detector [107].

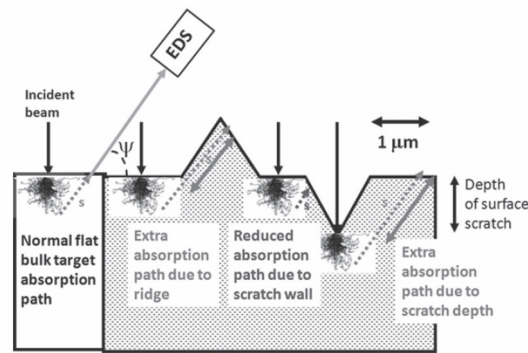


Figure 8: Local topography affecting EDS results [107].

In cross-section analysis, non-metallic inclusions are generally surrounded by a dens steel matrix. At automated or manual EDS analysis, NMIs typically emit low energy and high energy X-rays. According to Pistorius and Patadia [138] and the NIST database of adsorption coefficients [139], X-rays of lighter elements (O or Al) are increasingly absorbed by the steel matrix. In contrast, high-energy X-rays (Ca, Mn, or Fe) pass easier through the material. The remaining intensity after a specific path in the material, depending on its radiation type, can be calculated according to Equation 3 considering transmitted intensity (I), incident intensity (I_0), attenuation length (L), and radiation type (λ).

$$\frac{I}{I_0} = e^{-\frac{1}{\lambda}L} \quad (\text{Eq. 3})$$

Figure 9 illustrates the resulting intensity for different $K\alpha$ X-rays proceeding through pure iron. As already reported, high-energy X-rays stay relatively unaffected, whereby low-energy X-rays are almost totally absorbed after 0.5 -1 μm .

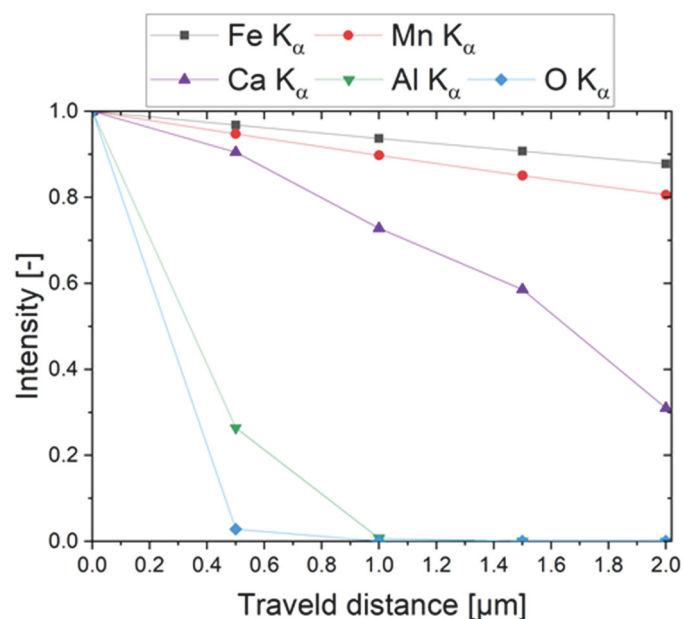


Figure 9: Intensity depending on attenuation length in Fe matrix according to [138].

Analysis of non-metallic inclusions being three-dimensional structures partly covered by steel matrix, detected composition results could be affected by particle cutting position and preparation quality. Newbury and Ritchie [108] reported different signal paths through the material as relevant for EDS results scattering in the range of 0.5 wt.%. Therefore, the best analytical results for 1keV photon considerations can be obtained by a mean sample roughness of about 20nm [91,107].

3.2 Influence of Inclusions' Cutting Position on the EDS data

Appearing shapes and characteristics created by sectioning during sample preparation are a well known issue in metallography [140]. Micro cleanliness evaluations of non-metallic inclusions in steels are based on chemistry, apparent morphologies, and sizes evaluated on two-dimensional cross-section BE-images [92]. A dimensional discrepancy created by combining two-dimensional optical information and three-dimensional composition information gathered by an interaction volume needs to be considered (Figure 3). For inclusion analysis in micrometer regions, an undefined interaction with the surrounding steel matrix depending on inclusion's size causes variations in the resulting EDS data. An increase of measured iron contents ($\%Fe^{EDS}$) is observed with decreasing inclusion size caused by matrix interaction [110,131], as illustrated in Figure 10.

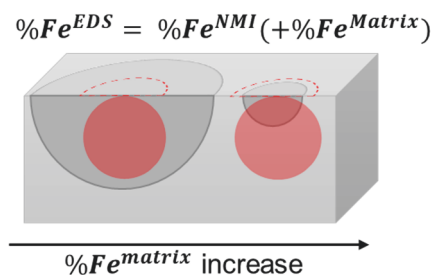


Figure 10: Increasing steel matrix interaction with decreasing particle size.

Not only differing sizes but also varying particles' depths (Z) affect the detected data output. In Figure 11, inclusions show the same appearing size with different cutting positions leading to higher detected iron contents at shallow particles.

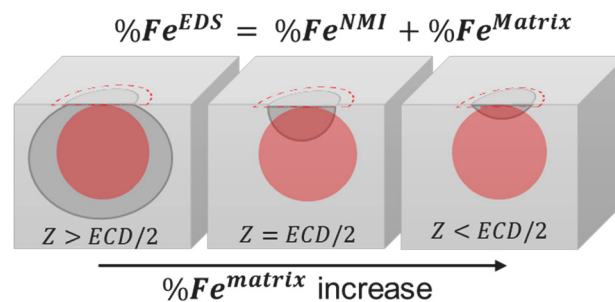


Figure 11: Different cutting position influencing EDS output.

In practice, the described effects of appearing size and remaining particle depth combine. Spheres with a large remaining depth (Z) should correctly measure Fe compositions, even for the smallest NMIs. But, according to Pistorius et al. [138], this cutting position can lead to underestimation of low energy photons by adsorption. Particle Ca-modification, being an essential tool in modern metallurgy, is hard to identify at this cutting state. With decreasing Z/ECD -ratio, steel matrix interaction increases, impeding iron content evaluations and minimizing the quantifiable EDS output after neglecting Fe. These disruptive effects at EDS measurements result in increased scattering of the data.

Nevertheless, Pistorius et al. [110,141,142] published an approach for particle depth assumptions based on the detected Fe peak. The iron content in inclusions is neglected, and the Z/ECD ratio is calculated based on the relative Fe peak of the generated spectra, leading to matrix effect corrections for under or overestimated elements. This procedure is legitimate for many metallurgical studies, and outstanding research was done for matrix corrections by the mentioned authors. In fundamental metallurgical research, a general neglecting of elements should be avoided in case of unexpected experimental results. Especially for new approaches in oxide metallurgy, analysis of segregation effects, or the verification of kinetic models, iron should always be considered a possible inclusion's constituent.

3.3 Image Recording Influencing Detected Data

As described in Section 2.1, feature identification at automated inclusion analysis is based on the backscattered electron image's chemical greyscale difference (for measurement parameters see Appendix A.3, Table 20). As displayed in Figure 12, various greyscale events (features) are identified during image recording of automated inclusion analysis:

- Inclusions with different appearing greyscale, size, and morphology (NMI 1 & 2)
- Cavities caused at sample solidification (pore)

- Uneven topography or scratches (scratch)
- Grinding residues with eventually adsorbed oxygen (SiC & SiC+O)
- Residues of the last polishing step (pol. res)
- Particles of the laboratory room (dust)
- Lubricant particles of the pressurized air can (CaO)

The first step towards improved steel cleanliness analysis is to avoid sample contamination by proper preparation in general. High contrast settings should be applied to compensate brightness differences of varied chemical compositions or shallow spheres [113]. Different acceleration voltages can also lead to changes in brightness and undetectable inclusions [141]. Nevertheless, all features within the defined threshold are identified and measured by the detector system's EDS software. High numbers of pollution particles or scratches result in an extended time effort for measuring inclusions.

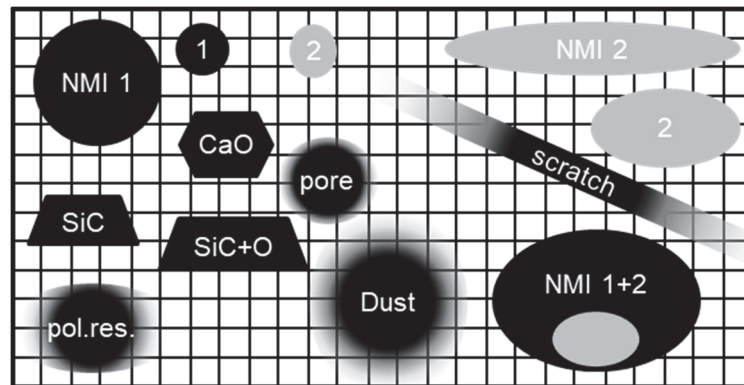


Figure 12: Greyscale features and artifacts at automated SEM/EDS analysis.

To ensure correct interpretations of inclusion populations, improved data post-processing is required. NMIs need to be separated from artifacts by manual evaluation or mathematical corrections. Otherwise, SiC+O, grinding residues with adsorbed oxygen, or CaO particles, originating from pressurized air cans' sealant, can be misinterpreted as particles of the steel and massively falsify the steel cleanliness description at high-quality steels.

During image recording, digitalization of the inclusions' appearance takes place. On the one hand, this pixel effect [115] shown in Figure 13 a) leads to undetected particles near the identification limit. On the other hand, coarsening of the non-metallic inclusions' detected morphology shown in Figure 13 b) can appear.

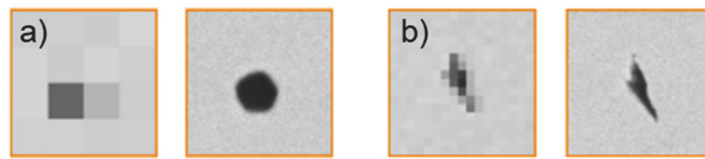


Figure 13: a) Suboptimal pixel limit b) Coarsening of inclusions appearance [115].

Morphological interpretations of sphericities can not be made correctly at smaller sizes of the detected particle. Additionally, a size grouping effect can be observed based on low pixel resolution. If image generation artifacts are not corrected before steel cleanliness evaluations, this leads to misinterpretation. For future evaluations, morphological categorization considering the mentioned image recording effects shall be formulated.

3.4 Automated Peak Identification Limiting the Interpretation of the Data

Composition evaluation of manual and automated inclusion analysis is generally performed according to the described non-standard EDS analysis methodology (Section 2.1). After generating the characteristic X-ray spectrum for each analyzed volume, the program compares the appearing peak positions and heights with the software provider database. This automated peak identification calculates chemical compositions based on distinctive spectrum parameters. Only the application of automated peak identification enables composition evaluations of thousands of particles in a manageable time effort [91]. Standard-based EDS analysis would not be feasible in this case.

Low energy range elements (200eV to 5keV), which are often essential constituents of non-metallic inclusions in steel (e.g., N, O, S, Al, Mg), can cause errors by missing K- and L-shell X-ray peaks caused by several physical effects [106,143]. This can consequently result in misinterpretation of inclusions' composition in the dataset can result. Missing elements or a shared quantity by cross interaction (e.g., Al&Br or Ti&V) can occur. According to Newbury [104], such ambiguous peak detection can only be determined by peak fitting versus measured references in extra manual post-processing steps. To consider cross-interaction defects of certain elements, Table 4 lists energy ranges and elements with overlapping peaks.

Table 4: Overlapping peaks problematic at automatic peak identification [106,143].

Below 5keV:	Elements with overlapping peaks
0.390-0.395 keV	N – Sc
0.510- 0.525 keV	O – V
0.670- 0.710 keV	F – Mn – Fe
0.845- 0.855 keV	Ne – Ni
0.900- 0.950 keV	Cu – Pr
1.00- 1.05 keV	Na – Zn – Pm
1.20- 1.30 keV	Mg – As – Tb
1.45- 1.55 keV	Al – Br – Yb
1.69- 1.80 keV	Si – Rb – Sr – Ta – W
2.00- 2.05 keV	P – Zr – Pt
2.10- 2.20 keV	Nb – Au – Hg
2.28- 2.35 keV	S – Mo – Pb
2.40- 2.45 keV	Tc – Bi
2.60- 2.70 keV	Cl – Rh
2.95- 3.00 keV	Ar – Ag – Th
3.10- 3.20 keV	Cd – U
3.25- 3.35 keV	K – In – U
3.60- 3.76 keV	Ca – Sb – Te
4.05- 4.15 keV	Sc – Xe
4.45- 4.55 keV	Ti – Ba
4.84- 4.95 keV	Ti – V – Ce

If single elements can definitely be excluded from the evaluation, the software allows the operator to eliminate them. A general list of excludable elements for inclusion evaluations in steel can be found at Newbury et al. [107]. For steel cleanliness evaluations of unknown samples, all elements should be considered in the first step, and adjustments should be made after validation of the result in a second quantification step.

3.5 Scanning Parameters Influencing the Detected Iron Content

Different scan settings need to be distinguished at manual and automated SEM/EDS analysis [144]. For the present system, single point (PScan) and area (AScan) settings are used for particle evaluations. PScan analysis is applied to homogenous phases or inclusions, keeping the interaction volume as small as possible. The sample's point of interest is defined manually by a simple click or automated by the software using greyscale thresholds. The measurement point's position accuracy depends on pixel size concerning the current

magnification of the digital image. The sight of interest is analyzed till a predefined limit is reached (time or counts). After interpretation of the resulting spectrum based on Oxford Instruments algorithms, the composition is optionally reported in weight or atomic percent. Single point analysis is recommended for evaluations of already familiar homogenous inclusion populations only. To achieve better results at unspecified inclusions, automated inclusion analysis with area scan settings is preferential to avoid missing heterogeneous particle phases. Figure 14 illustrates data acquisition of different scan settings. Like single-point analyses, AScan measurement's output is the mean composition of all single-point analysis of every inclusion pixel measured. At AScan settings, the outmost positioned measurements create a consistent ring of electron interaction around the analyzed inclusion depending on the particle morphology (Figure 14). For particle analysis in unalloyed steels, the appearing interaction ring shows an approximate width of 400 nm, according to Casino simulation (see Section 4.2.).

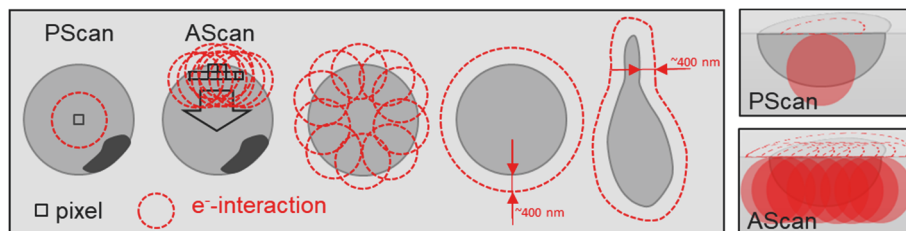


Figure 14: PScan and AScan settings creating different interaction volumes.

Figure 15 quantifies the increased matrix interaction caused by AScan setting. Constantly more extensive iron contents are detected at area scans for the same particle population at 15kV.

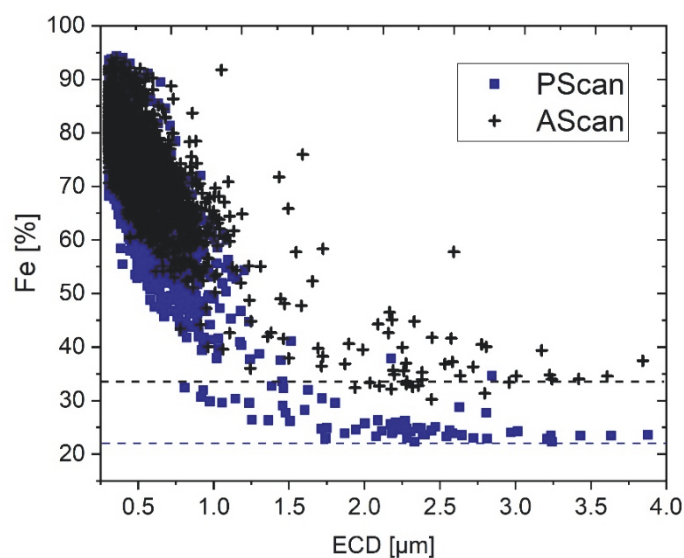


Figure 15: Detected particles' iron content for different scan parameters.

For the smallest inclusions, up to 95 % iron is detected. For particles in this sub-micro (<1 μm) size range, the scanning method's influence seems to decrease due to approximation of the overall interaction volume. This general falsification inhibits the evaluation of matrix element concentrations in non-metallic inclusions at automated measurements. Therefore, research dealing with wettability, separation, nucleation, or other effects of inclusions influenced by Fe-contents is exceptionally challenging to evaluate through small particles' EDS compositions.

3.6 Inclusion Morphology, Clusters, and Strings Identified by Automated SEM/EDS Analysis

A beneficial output of the automated analysis is the stored position, and morphological data of each non-metallic inclusion detected. According to magnification and image resolution, single NMI-pictures are generated and quantified by area, length, width, orientation, and perimeter. Standard categorization [81] of inclusions' morphology and long-range orders deal with optical identification of particle sizes > 2 μm , especially specified for meso defect sizes caused by research history. There absolute distances of 40 μm and 20 μm are used for grouping identification. These thresholds cannot be applied to as-cast products or inclusion populations in the micro and sub-micro size regime. Therefore, in most steel cleanliness evaluations, morphology, spatial distribution, and long-range particle orders often remain disregarded. A possible approach dealing with particle distances for cluster evaluations based on automated analysis data is published by Wartainen et al. [145], depicting particles based on feature data set and quantifying the euclidian distance of detected inclusions. Additionally, Seleznev et al. [146] published an image-based particle evaluation methodology by recreating inclusions and applying image algorithms for identification. Although providing a high potential of helpful information to specify inclusion origins and behavior, any specific standard for sub-micro and micro cleanliness evaluations dealing with distance relations is published at the moment. The demand for improved interpretation of particle arrangements increases in the future. Especially not-rolled materials and new goods entering the market with as-casted, hiped, or printed metal microstructure categorization standards are needed. Potentially, distances and nearest-neighbor correlations of finely dispersed inclusions can be used as a characteristic value for homogeneity quantification of steels.

3.7 Improvement Potentials in Non-Metallic Inclusion Analysis

In the past years, scanning electron microscopy combined with EDS analysis has been essential for non-metallic inclusion analytics. The output of morphological and chemical information enables inclusion evaluations for fundamental research as well as industry demands. In the early days of microscope and detector systems, the research output level was often low due to technical limitations of the used systems. Acquisition times, image resolutions, or detector accuracy minimize metallurgist requests to examine thermodynamic and kinetic phenomena. As illustrated in Figure 16, metallurgical evaluation and interpretation of SEM/EDS data were often performed with sufficient distance to technical limits of analyzing systems avoiding discussions about representativeness of measurements. The technical limit constantly increased to better performances enabling analysis of lightest elements and smallest particles with the ongoing development of microscope systems, detector technologies, and evaluation algorithms. Additionally, publications dealing with the correct interpretation of measurements' results improved analytics and data evaluation knowledge. Today non-metallic inclusion analysis is often performed close to the analytical limit of available systems.

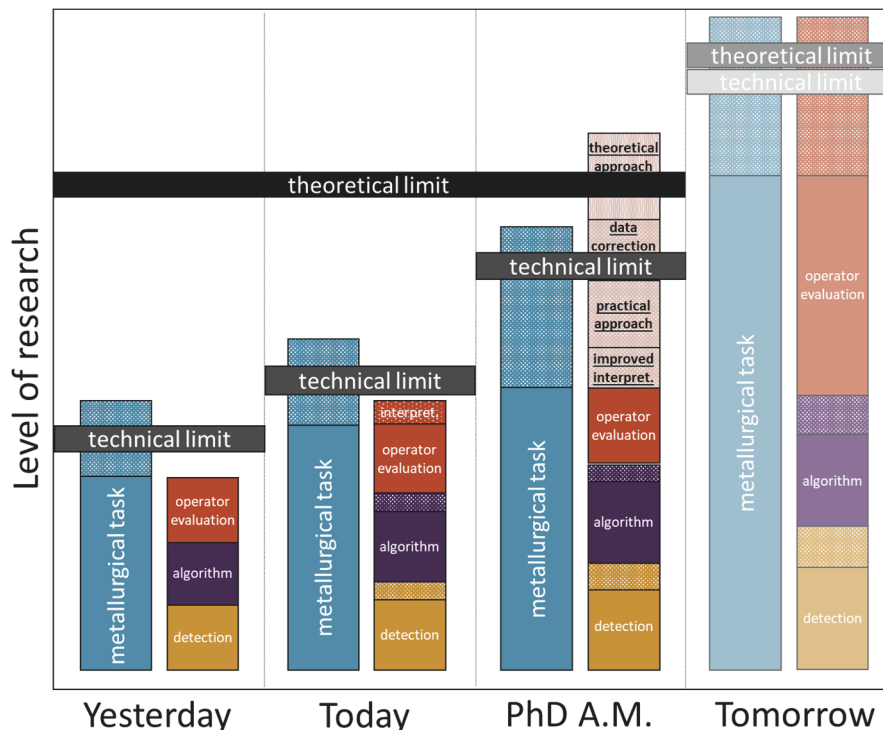


Figure 16: Influence of the present work on metallurgical inclusion analysis by means of SEM/EDS.

SEM systems, EDS detectors, and algorithms are constantly improving, and future developments improve in terms of the systems' representativeness and measurement correctness, according to Newbury [95]. Given this background, the current thesis outlines new innovative approaches for steel cleanliness evaluation focusing on the arising challenges related to high performance steel products. Practically, this concerns the following aspects which will be explained in detail in the subsequent sections of this thesis:

- Improved data classification and typification enable better fundamental interpretations resulting in more efficient metallurgical research.
- Practical approaches, including matrix dissolution experiments and the development of inclusion reference sample production, advance the technical limit of analysis.
- Enhanced data treatment and mathematical correction of matrix interferences outline the potential of enabling innovative particle characterization methodologies beyond standards.
- Theoretical approaches discuss general influences on particle formation for research demands, and an improved understanding of cutting positions and electron interaction at SEM/EDS analysis is realized by simulation of automated inclusion analysis on a new level. Steel cleanliness evaluations can therefore be realized exceeding the physical limit of SEM/EDS systems.

4 Solution Approaches for Improved Inclusion Analysis

This work's primary focus on EDS interaction at metallographic cross-section samples is accompanied by a proper experimental procedure for standard sample production, improved sample preparation, and simulations of manual and automated measurements, enabling evaluations beyond EDS systems' physical limits. All gathered knowledge and approaches are summarized in characterization guidelines for steel cleanliness evaluations in micro and sub-micro size regimes.

4.1 Holistic Consideration of NMI Formation During Experiments

For substantial research, good preliminary work is necessary to identify all possible influences affecting the experiments' outcome. Direct and indirect parameters influencing inclusions' formation and analysis are illustrated in Figure 17 as part of a sound experimental design to deal with in NMI-research.

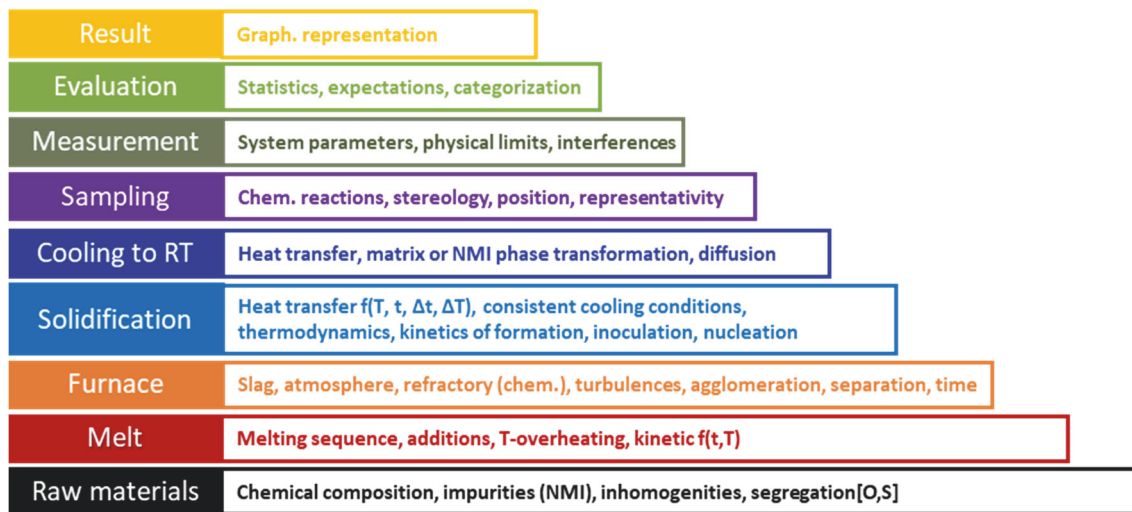


Figure 17: Parameters affecting the output of non-metallic inclusion analysis.

Thermodynamic and kinetic calculations can reduce the probability of failing and supporting experimental parameters' definition before performing the first metallurgical experiments. A considerate selection of raw materials should be the basis of all practical approaches. Therefore, quantifying exact chemical compositions and verifying preexisting non-metallic inclusions in any experiment's input material is necessary. During the sample production, accurate documentation of preheating cycles, holding times, casting temperatures, cooling conditions is essential to ensure reproducibility and research transparency. Additionally, all possible parameters affecting non-metallic inclusions morphology or chemistry should be considered to perform comprehensible particle analysis and data interpretation. Misleading correlations caused by the experiment system itself must be avoided. If practicable, interim sampling can clarify the inclusions population's changes by particle modification or separation effects in the furnace system. Then, a particular focus on appropriate sampling and cross-section preparation is essential for trustable and representative results. For enhanced inclusion classification, typification, and data interpretation, the sample's temperature history at all stages influencing particle characteristics needs to be considered at threshold definition. Different post-processing approaches can be beneficial according to the specific research task. In the end, an appropriate result representation is fundamental for objective discussion. If, for instance, liquid state conditions during steel production shall be discussed, it can be beneficial to evaluate melts' oxidic steel cleanness. Events at sample solidification can be evaluated by interpreting spatial distribution and sizes of small nitrides and sulfides. Before performing experiments or applying analysis to inclusion populations, the mentioned parameters of Figure 17 are advised to be considered in discussion and interpretation of any measurement data.

4.2 Simulation of Electron Interaction and X-ray Generation

As explained in Chapter 3, different effects and phenomena influence the result of applied energy dispersive X-ray analysis. Electron and X-ray interactions are simulated based on probability theory and physical models to assess and discuss even invisible effects during inclusion measurements. Using Casino V2.5.1. [147,148] a free to use software, electron interaction simulation in solid materials can be applied. The general input parameters for the simulation are material composition, density, and electron beam parameters (Appendix A.4, Table 21). On the one hand, backscattered electron images can be simulated for matrix/inclusion contrast predictions [113,149]. On the other hand, resulting interaction bulbs of deflected primary electrons ($e\text{-prim}^*$) for different materials are created and evaluated, as illustrated in Figure 18. Quantification of results is performed based on data extraction in table form. In most publications, electron interaction bulbs are discussed dealing with non-metallic inclusion analysis. Contrasting the electron interaction bulb (left) and the simulated X-ray interaction (right) in Figure 18, a significant size difference of the appearing bulbs can be noted.

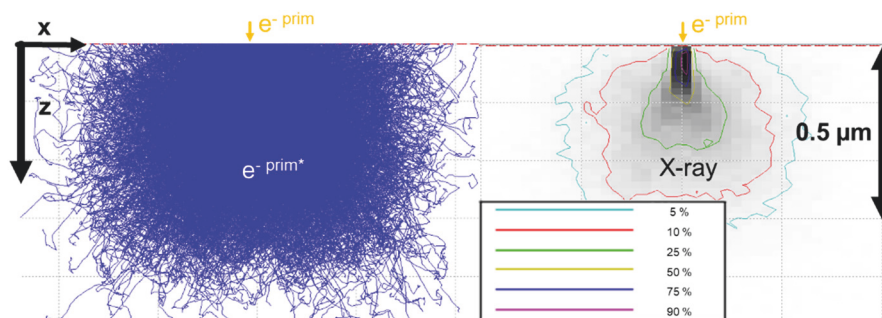


Figure 18: Simulated electron and X-ray interaction for 15KV in pure iron.

Considering 5 % remaining intensity for X-ray generation, a significantly smaller interaction volume than assumed by electron interaction ($e\text{-prim}^*$) can be noted. To quantify this often unconsidered phenomenon in steel cleanliness evaluations, dimensions of X-ray propagation are exported. Based on the intensity output of each characteristic X-ray shell (e.g., $K\alpha$, $L\alpha$) depending on its z position, the theoretically detected information is calculated.

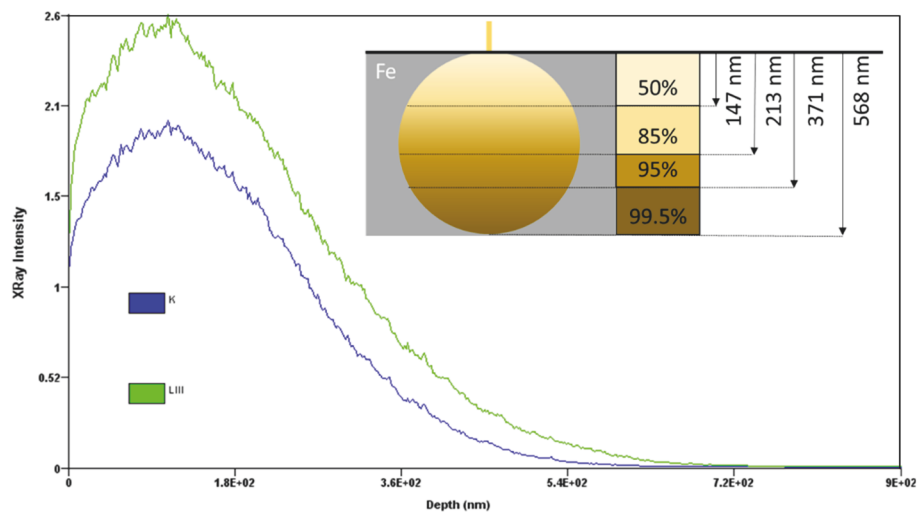


Figure 19: Characteristic X-ray intensity according to interaction depth z.

In Figure 19, X-ray intensity declines with advancing depth after reaching a maximum at about 100 nm calculated for 15 kV and pure iron. The cumulative intensity (I^{cum}) for every z-position is calculated according to Equation 4 for all elements ($i = N, O, Al, Si, Fe...$) present during analysis.

$$I^{cum} = \sum_i^j K_{\alpha}^i + L_{\alpha}^i + M_{\alpha}^i \quad (\text{Eq. 4})$$

Concluding, 85 % of X-ray intensity is already generated in the first 213 nm. If maximum x-ray interaction is defined by 99.5 % cumulated intensity, almost all X-ray is generated after 568nm resulting in an actual smaller interaction bulb as estimated by the e-bulb illustration in Figure 18. This fact needs to be taken into account discussing interaction volumes at sectioned steel sample inclusion populations.

4.2.1 X-ray Interaction Volume in Varied NMI Types

To further evaluate the interaction processes during EDS analysis, X-ray bulbs for different non-metallic inclusion compositions are calculated and examined. Depending on the chemical composition and density of the analyzed material, primary electrons have different interaction depths. In the following diagram, the resulting intensity curves are displayed for CaS, AlN, Al₂O₃, MnS, and TiN. According to the simulation, CaS interaction results in more material interaction than analyzing MnS inclusions shown in Figure 20.

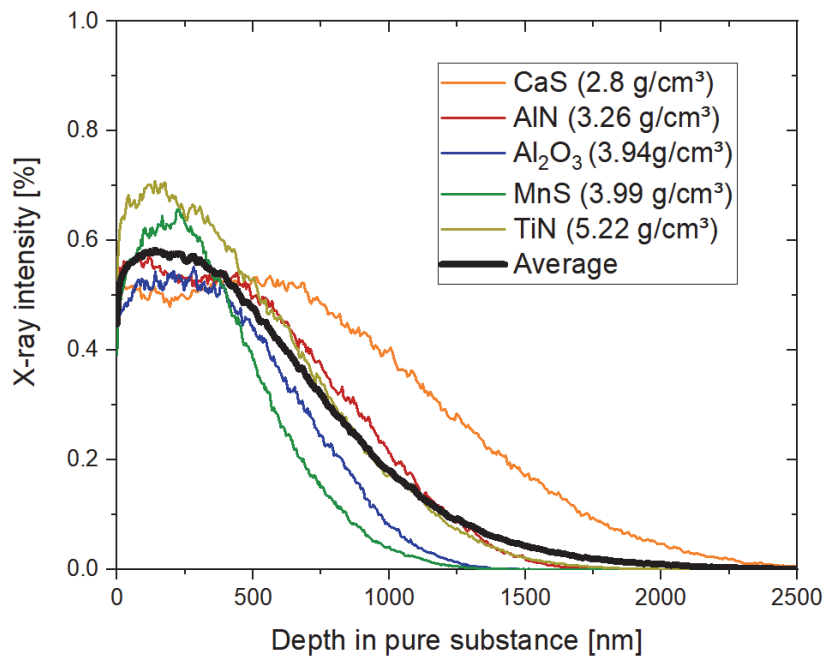


Figure 20: X-ray interaction for typical non-metallic inclusions in steels.

Due to a minor penetration resistance depending on the inclusions' characteristics, larger NMIs can still include matrix X-ray information (%Fe). Calculating an average intensity curve for typical steel inclusions, an X-ray interaction depth of 2 μm needs to be considered for advanced SEM/EDS analysis of non-metallic phases and data interpretation.

4.2.2 Simulation of X-ray Interaction of Different Inclusion Depths in an Iron Matrix

As discussed in Section 3.2, the inclusions' three-dimensionality, including size and remaining particle depth, strongly influences the EDS result. A two-dimensional layer assumption is defined to correlate depth-related interaction and non-metallic inclusion characteristics during particle analysis in steels. As illustrated in Figure 21, a non-metallic layer phase on top of the Fe-matrix is defined with a specific thickness representing the remaining depth of an Al_2O_3 inclusion cut at a particular position. Based on estimated particle depths by $\text{ECD}/2$, the shown interactions are similar to Al_2O_3 particles with a size of 1 μm and a depth of 500 nm. The dimension drafts of spherical and cubic particle shapes are in good accordance with the applied layer assumption for first interaction simulations.

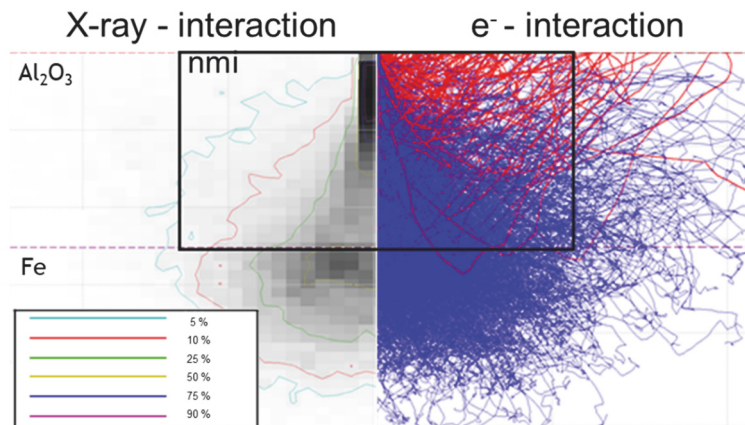


Figure 21: Illustration of two-dimensional NMI layer assumption and interaction.

The before mentioned $K\alpha$ and $L\alpha$ intensities for Al, O, and Fe are evaluated. At 500 nm, the Al_2O_3 to Fe transition can be seen in Figure 22. The Al and O intensity drop and an interaction depth of approximately 650 nm are deviated by reaching 99.5 % of I^{cum} .

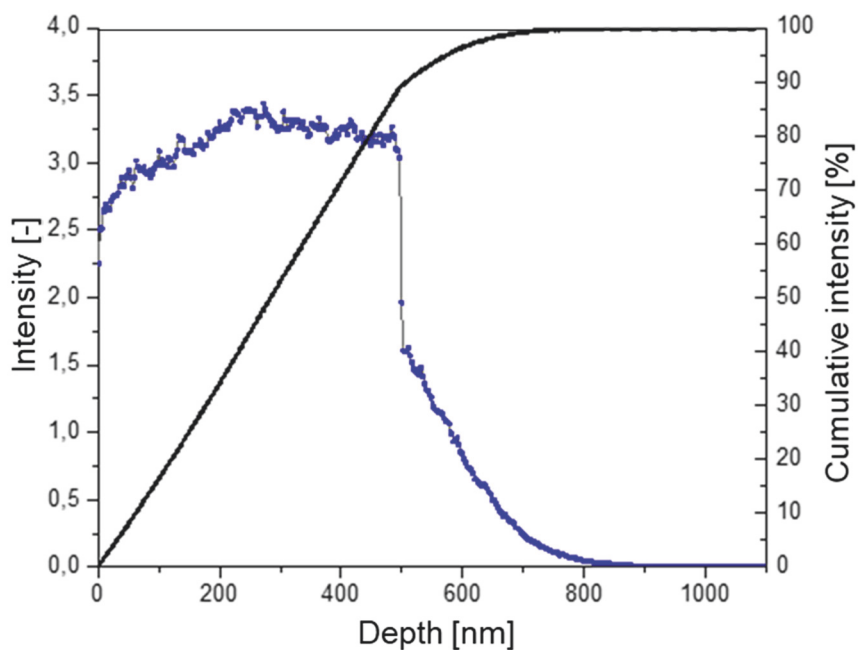


Figure 22: X-ray interaction for a 500 nm thick NMI layer.

The same procedure is applied for different particle sizes and resulting inclusion depths. Different layer thicknesses of Al_2O_3 significantly influence the resulting X-ray interaction and information gathered at the EDS detector. Calculating the resulting ratio of NMI and matrix information (I_s) according to Equation 5 for different particle depths, the theoretical materials intensity-share can be quantified.

$$I_S = \frac{I_{NMI}^{cum}}{I_{NMI+matrix}^{cum}} = \frac{\sum_i^i K_{\alpha}^{Al} + K_{\alpha}^O}{\sum_j^i K_{\alpha}^{Al} + K_{\alpha}^O + K_{\alpha}^{Fe} + L_{\alpha}^{Fe}} \quad (\text{Eq. 5})$$

A defined simulation strategy was performed to evaluate different simulated X-ray interactions at varied particle compositions. Calculations were realized at particle depths (layer thickness) of 150 nm, 250 nm, 500 nm, 750 nm, 1000 nm, 3000 nm, and pure substrate for nine different typical non-metallic inclusions: CaS, MgO, Al₂O₃, MnS, MnO, TiN, AlN, Mn₂O₃ and Ti₂O₃ (Particle densities can be found in Appendix A.4, Table 22). With increasing particle depth, the %Fe^{matrix} share decreases. The thinnest layer of 150 nm represents particles with a 0.3 μm appearing size, defining the reasonable size limit for quantifying non-metallic inclusions in steel for the described detector system. Depending on phase composition and material properties, different interaction depths and NMI/Matrix ratios of the interaction volume can be expected for varying inclusions similar to Figure 22. In Figure 23, the intensity split is contrasted to the actual layer thickness calculated by Equation 6 including Boltzmann constants (A1 and A2).

$$y = A2 + \frac{(A1 - A2)}{1 + e^{\frac{x-x_0}{dx}}} \quad (\text{Eq. 6})$$

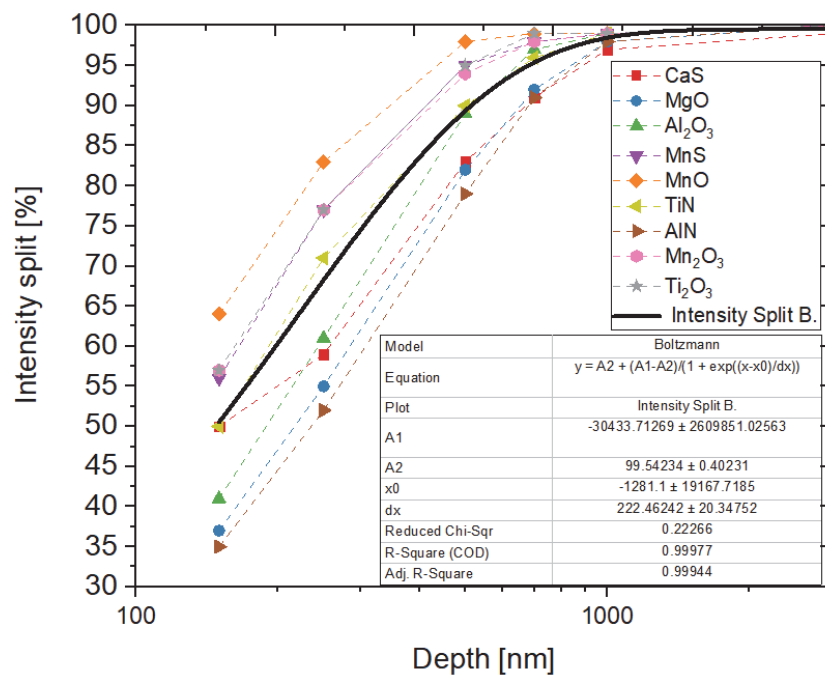


Figure 23: Intensity splits depending on particle composition and depth.

It can be seen that MnO inclusions result in a better information ratio than for instance AlN inclusions showing larger interaction volumes. An average intensity split is formulated by Boltzmann approximation of the mean interaction split to consider intensity ratios depending on particle size in future guidelines.

4.3 Digital Simulation of Automated Inclusion SEM/EDS Analysis

The most significant challenge in improved EDS analytics is to explain analysis phenomena by interpreting its resulting data. This discrepancy often leads to estimations and assumptions for more accessible explanations of exact particles' compositions. Evaluation of Casino V2.42 simulations described in Section 4.2 resulted in enhanced knowledge of EDS interaction during manual and automated measurements. Based on that knowledge, an approach is formulated to create a digital replica of automated non-metallic inclusion measurements. Especially for inclusions in the sub-micro size regime, this theoretical approach improves the understanding of phenomena due to the enhanced difficulty of analysis. Consequently, it is possible to define exact chemical compositions for inclusions without kinetic effects and to determine the cutting position of analyzed particles in the steel matrix. Various phenomena are correlated to the resulting EDS output by evaluating invisible or undetectable parameters (e.g., exact particles cutting position).

4.3.1 Description of Simulated Automated Steel Cleanness Measurements

Fortran programming is used to digitally create non-metallic inclusions and simulate their analysis due to simple and efficient coding. Schwartz-Saltykov [150] approaches have been considered, but due to avoiding size class grouping discrepancies and to create digital NMI's most simply, the following procedure is pursued:

- Harmonic mean, volumetric mean, volume share, and particle number per volume are calculated according to Takahashi and Suito's [66] distribution-free evaluation based on performed automated measurements. Additionally, truncated particles below 0.3 μm detection limit are considered, so the mean value and standard deviation of particles' total can be calculated. Subsequently, lognormal distributed spherical volumes are generated on random positions [92], fulfilling the mean and standard deviation of previous distribution-free evaluations. A randomly positioned cutting step illustrated in Figure 24 is performed, creating a digital cross-section plane with corresponding appearing sizes of inclusions. To every appearing particle diameter (d), the actual particle size (D) and the corresponding cutting position (h) is stored in the database.

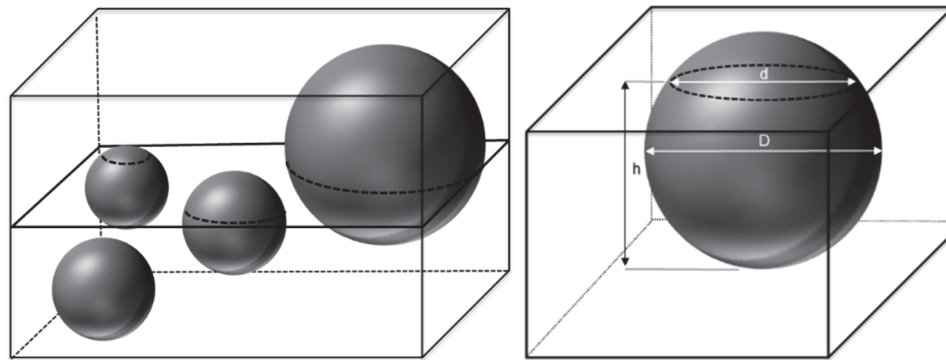


Figure 24: Volumetric spheres and cutting procedure determining characteristic geometry parameters.

- A $0.1 \mu\text{m}$ grid overlay (1pxl) is done on the cutting plane, as displayed in Figure 25, simulating the SEM system's image recording step. The following greyscale depending feature identification step is reproduced by the fraction of the inclusion's area within a single pixel. If more than 65 % is NMI area, the total pixel is active. Additionally, the smallest considered diameter is determined by a 9-pixel threshold resulting in a minimum particle size of $0.3 \mu\text{m}$, identical to real measurements. Then, cubes (voxels) are generated in z directions based on the $0.1 \mu\text{m}$ grid. Related to the area-fraction threshold, a volume ratio of $> 65 \%$ particle is defined as 100 %NMI. The remaining voxels are 100 % matrix. Depending on the voxel type, the corresponding composition for NMI (e.g., 20 %O – 30 %Mn – 50 %Fe) or matrix (e, g., 0 %O – 0 %Mn – 100 %Fe) is defined.

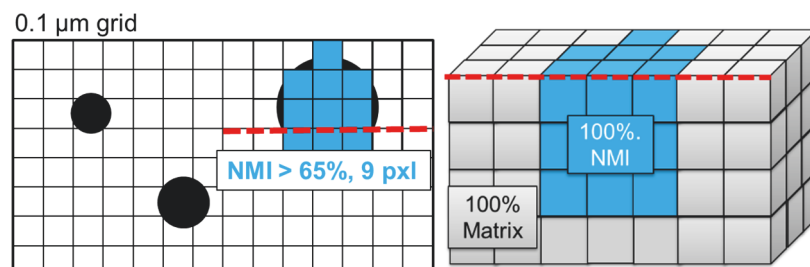


Figure 25: Imaging step and threshold definition and voxel generation.

- To recreate EDS measurements performed on an inclusion population's digital twin, X-ray interaction bulbs are developed by simulated EDS analysis on every active surface voxel, inspired by area-scan settings of actual automated particle analysis. Starting with an intensity of 1 at the surface voxel, the energy decrease in all directions (Z, N, E, S, and W) is calculated by a step-wise reduction of the initial value decreasing with every new voxel until the intensity is zero ($I \leq 0$), illustrated in Figure 26. The intensity

decrease at every pixel pass is calculated corresponding to X-ray interaction simulation with Casino V2.42 for the given matrix and NMI composition.

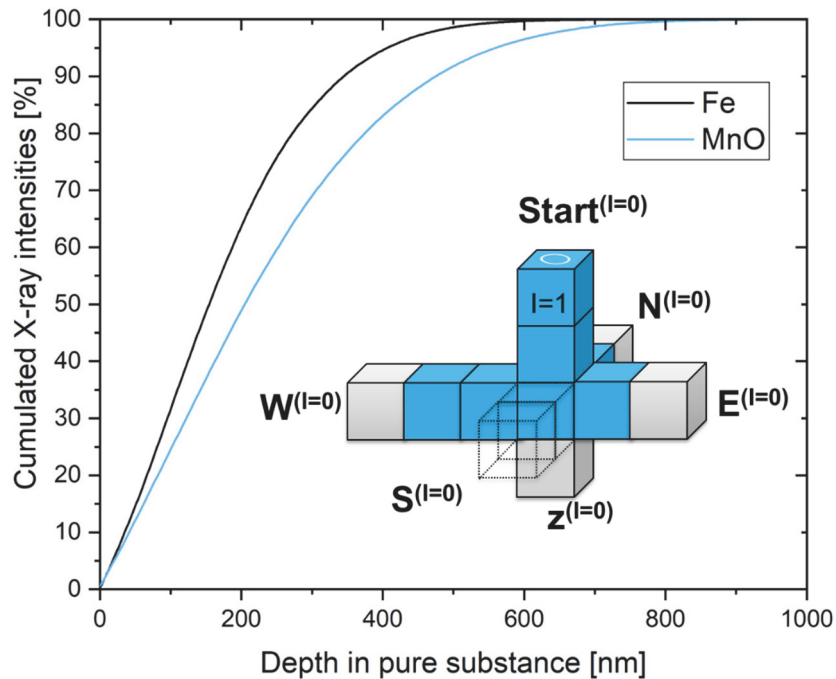


Figure 26: Implementation of X-ray interaction and intensity decrease.

- Finally, a quantification step for all created NMI and matrix voxels inside the calculated interaction volume is performed by the combination of different mean values, as illustrated in Figure 27. Every horizontal path is quantified by the arithmetic mean value of all compositions in N, E, S, and W reduced in the vertical voxel corridor (A). Then a weighted mean value based on intensity is calculated for all Z voxels (B) and summarized in the top unit. As a last step, the arithmetic mean value of all remaining surface particles is calculated (C).

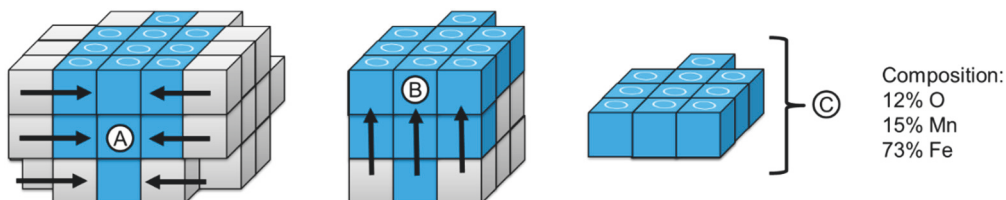


Figure 27: Voxels' mean value generation.

The end value (e.g., 8 %O – 9 %Mn – 73 %Fe) represents the EDS measurement of a non-metallic inclusion, including iron matrix falsification. Additionally, morphological parameters as

appearing diameter, original diameter, exact NMI composition, and the cutting height can be correlated to the resulting measurement composition.

4.3.2 Simulated SEM/EDS Analysis in Comparison to Performed Measurements

Evaluating the simulation, the digitally created EDS composition is contrasted to performed measurements. In Figure 28, the detected $\%Fe^{EDS}$ composition is displayed depending on the appearing equivalent circle diameter (ECD). The composition of NMI-voxels was set according to the result of EDS analysis after electrolytic extraction serving as input parameter for the calculation (20 %O, 68 %Fe, and 12 %Mn). A detailed description of extraction and composition analysis will be given in Sections 4.5 and 4.6. A color scheme considers the relative cutting position of the digitally created inclusions. Inclusions sectioned at the top with a large remaining height are colored in blue, whereas shallow NMIs are marked red.

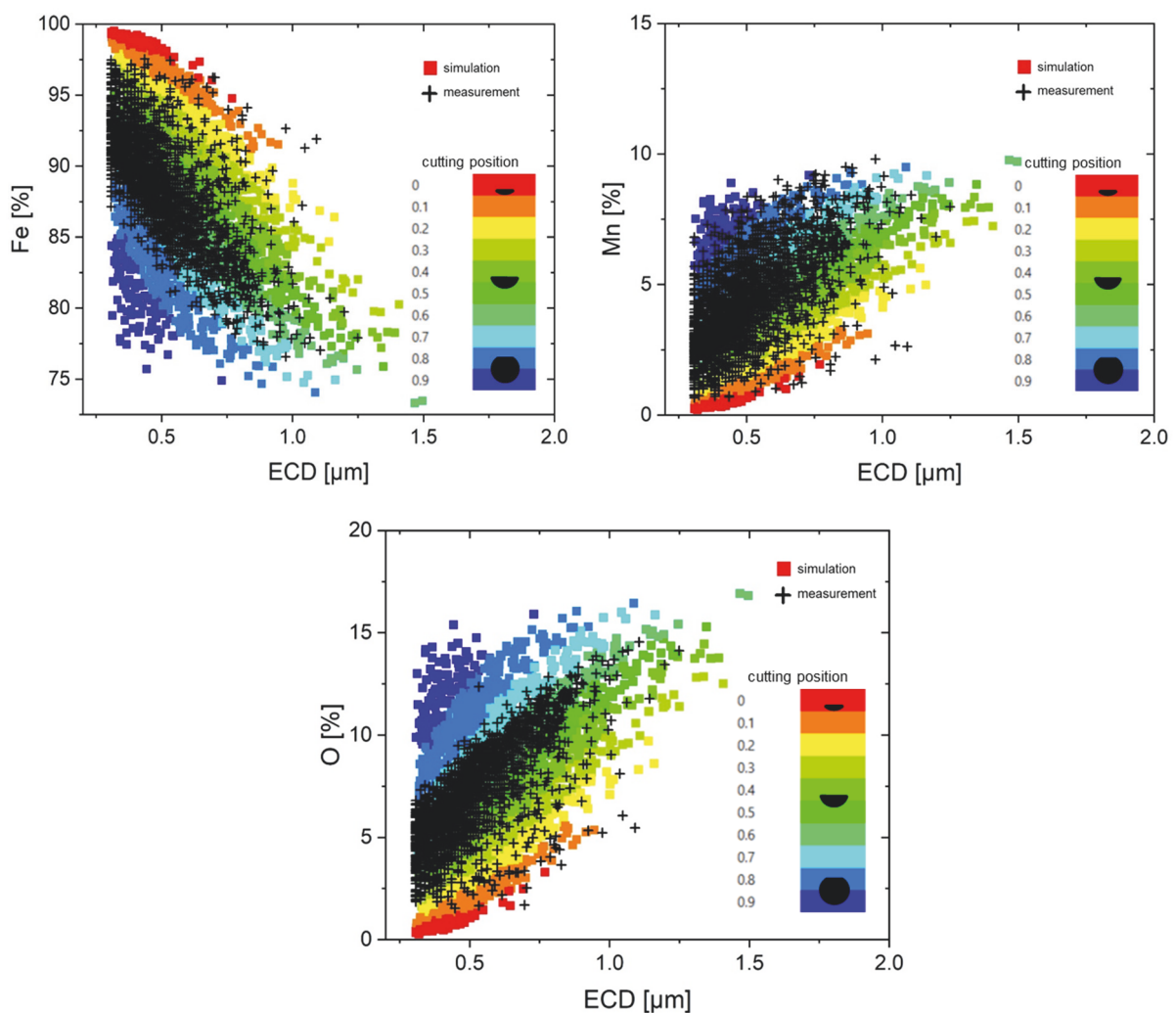


Figure 28: Comparison of simulated and measured EDS results.

In simulated and real measurements, the same amount of increased matrix interaction resulting in higher detected %Fe^{EDS} contents with decreasing sizes can be observed. The gradient of the iron increase for both particle populations is similar, affirming the practicability of the Fortran simulation's digital EDS approach. Differences can be seen in very high and low iron contents of sub-micrometer inclusions. Digitally created measurements show an increased number of extreme values. According to the color scheme, most of these data points show very large or small remaining inclusions' depth. The inverse tendency can be seen in the detected oxygen and manganese contents. With a smaller diameter, the contents decrease caused by more %Fe^{matrix} detected. Varying contents at small diameters are again detectable for simulated particles. The difference to actual measurements may be caused by mechanical removing of shallow inclusions, in reality, varying greyscale differences and x-ray absorption:

- During sample preparation, the surface is cut, ground, and polished. Extremely shallow inclusions may be removed due to poor bonding to the metal matrix and deformation of the bulk material.
- Additionally, shallower particles appear brighter because of the increased electron backscattering of the matrix below the particle. Consequently, these particles may be excluded by the greyscale threshold, as already reported in the literature [113].
- Comparing actual and simulated results of sunken spheres (blue data points), the simulation shows overestimated detection of O K α X-rays. At Fortran simulation, quantification is realized by arithmetic and weighted mean values. A relative detector position and adsorption effects by surrounding steel matrix described in Sections 3.1 and 3.2 are not considered.

Further, for a more detailed discussion of cutting positions, Figure 29 contrasts the remaining particle height and the original size before the sectioning step. It is evident that the smallest inclusions have the most variety of cutting positions concentrating on top or bottom sectioning. With increasing diameter, the sectioning step tends to result in more centered positions. This fact confirms the theory of cutting positions influencing the result.

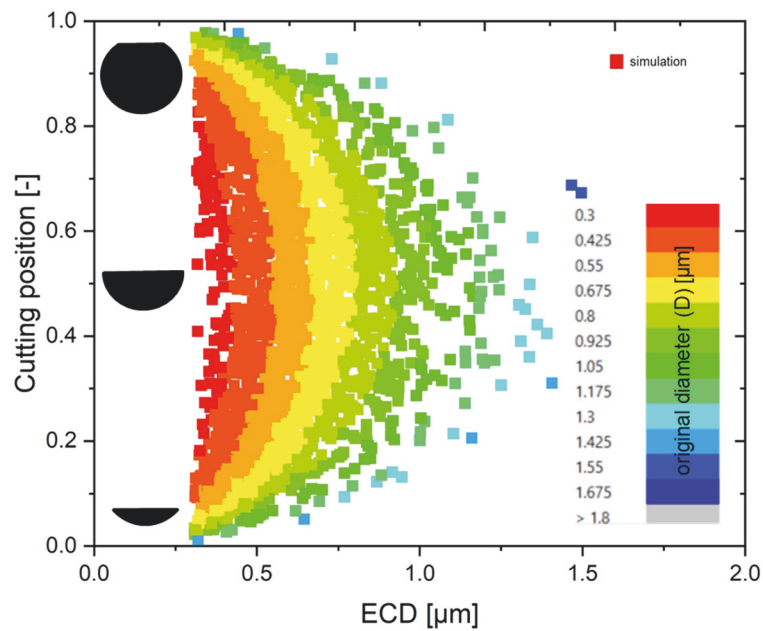


Figure 29: Favoured cutting position depending on inclusion size.

The theoretical approach of creating a digital inclusion population reveals new insight into an unknown territory of non-metallic inclusion analysis. The creation of a digital inclusion population referring to real sample is realizable. After composition definition at isolated particles and generation of necessary X-ray intensity interactions, automated inclusion analysis can be simulated. Future consideration of metallographic sample preparation effects or eventually changed greyscale appearance can improve the simulation result. Nevertheless, evaluation and interpretation of these theoretical approaches increased the understanding of cutting probability and the apparent influence of X-ray adsorption effects caused by the surrounded matrix.

4.4 Consideration of X-ray interaction for single-point analysis

For many tasks, simple single-point EDS measurements enable sound metallurgical interpretations. A guideline for SEM/EDS operators performing manual evaluations of non-metallic phases is formulated considering electron interaction volumes based on described theoretical knowledge. Depending on the material composition and density, different interaction depths performing electron bulb simulations are calculated for typical non-metallic phases listed in Table 5. According to calculations performed in Section 4.2 interaction depths are in the range of 600 to 2000 nm.

Table 5: Calculated interaction depth depending on particle composition and density at 15kV.

NMI	Density	X-ray Interaction Depth	NMI	Density	X-ray Interaction Depth
[-]	[g/cm³]	[nm]	[-]	[g/cm³]	[nm]
BN	2.11	1840	CrS	4.85	1120
SiO	2.13	2155	Mn₃O₄	4.86	881
SiO₂	2.19	2101	CrO₂	4.89	908
MgS	2.68	1589	TiO	4.95	893
CrO₃	2.70	1650	MnO₂	5.03	861
CaS	2.80	2246	TiN	5.22	834
AlN	3.26	1478	Cr₂O₃	5.22	837
CaO	3.37	1265	MnO	5.45	785
BN	3.45	1122	VC	5.77	747
MgO	3.58	1287	VN	6.04	724
Al₂O₃	3.94	1196	Ce₃ONS	6.25	719
MnS	3.99	1123	Cr₂₃C₆	6.54	667
TiO₂	4.24	1060	Cr₃C₂	6.68	641
Ti₂O₃	4.49	990	NbC	7.60	648
Mn₂O₃	4.50	949	NbN	8.40	587

In Figure 30, the calculated depths and inclusion densities are compared. If SEM operators analyze non-metallic phases without knowing the exact composition or density, a feasible assumption of the generated bulb can be achieved using the following diagram. Applying the correlation for single point inclusion analysis, interaction volumes can be assumed as spherical interaction bulbs with a diameter equivalent to the calculated depth. To quantify matrix element concentrations in inclusions, dimensions of the emerging interaction volume must be within the non-metallic phase. For non-metallic inclusions, remaining particle depths are approximated by half of the appearing inclusion size. For example, if homogenous Al₂O₃ or MnS inclusions with an approximate density of 4 g/cm³ are analyzed, a minimum particle size of 2.3 μm should be guaranteed for matrix-free EDS particle evaluation.

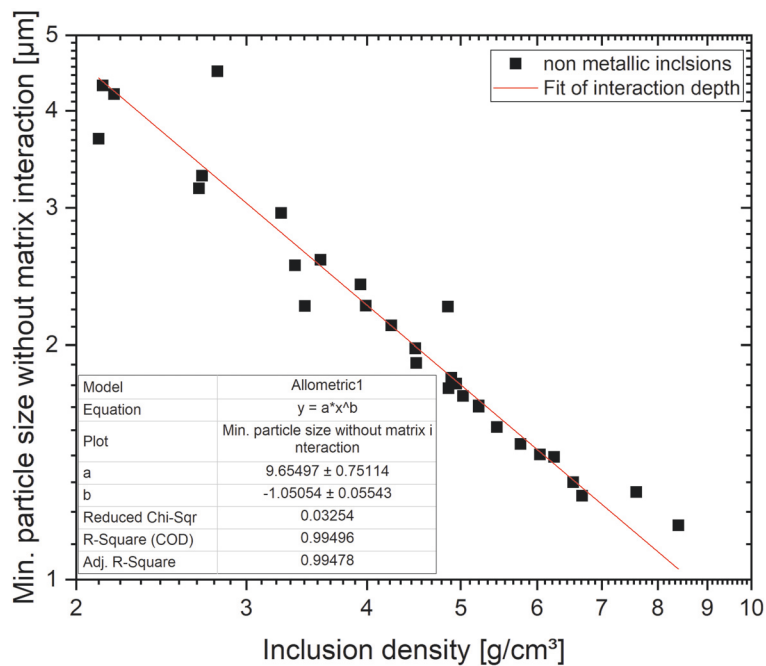


Figure 30: Minimum particle size avoiding matrix interaction for single-point analysis.

Considering these size limits, matrix element quantification of inclusions can be realized for NMIs of a specific size. Thinly sectioned inclusions or unfavorable cutting positions cannot directly be considered. An increased number of measurements enable outliers' compensation, as shown in Figure 31, displaying detected Al_2O_3 compositions in contrast to an appearing diameter of 0.3 – 3.5 µm. A detectable matrix interaction can be observed starting at 2.5 µm particle size. With decreasing size, an increased matrix interaction can be detected. Taking polygonal particle shapes and the unknown cutting position of Al_2O_3 inclusions into account, the calculated theoretical limit of 2.3 µm of Figure 30 correlates well with the displayed results in Figure 31.

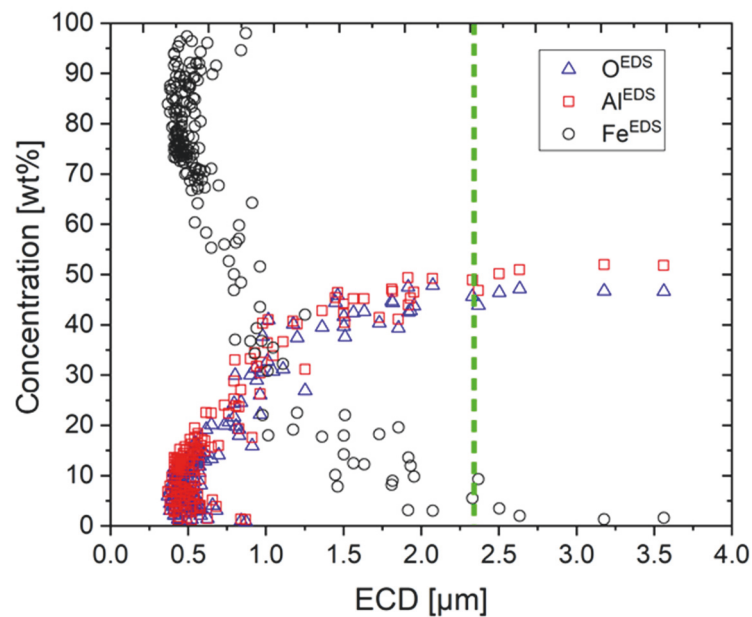


Figure 31: Detected composition at single point analysis at Al_2O_3 particles.

The illustrated guideline considering material density and inclusion size in Figure 30 can be applied to composition evaluations of most homogenous inclusions in steels for different research tasks. Considering the minimum size limit for inclusion evaluation, better qualitative and quantitative results can be obtained. Even evaluation of matrix element concentrations in inclusions (e.g., iron content) can be verified. The guideline can be applied to non-metallic phases in any bulk material of non-ferrous alloys or any other material because of the interaction volume merely depending on the non-metallic phase itself.

4.5 Inclusion Extraction Enabling Matrix-Free EDS Analysis

The application of inclusion extraction methodologies is discussed to improve SEM/EDS analysis by enhanced preparation procedures. Three approaches of dissolution experiments are described to practically eliminate electron interaction with iron bulk material during SEM/EDS analysis. Depending on the non-metallic inclusion population, steel grade, and research task, various approaches are beneficial.

4.5.1 Electrolytic Extraction Applied to (Fe,Mn)oxides

Matrix dissolution by electrolytic extraction reveals precise handling of experiment parameters. During the experiment, dissolution speed is controlled by the electrical current applied to the system. Changes of the driving force can easily be monitored and adjusted if necessary. In the setup displayed in Figure 32, steel samples are machined to a rod like geometry and mounted in the center of a precious metal cage (Pt-grid). In a Teflon beaker, the chosen electrolyte of choline chloride and urea (1:1) with 1 % dimethyl-formamide additive is heated up to 60°C, ensuring low viscosity and good conductivity. By constant stirring and temperature control of the liquid by a thermocouple mounted on a carrying arm, stable electrolyte conditions are ensured. A multimeter, including current and voltage control, supplies the necessary energy for enhanced Fe dissolution (0.1 A and 15 V). After extensive literature research and several pretest studies on the practicability of inclusion isolation by electrolytic extraction, an improved housing was developed with additional inlets for electrolyte control and a bigger volume for larger beakers. The plastic hood prohibits no contamination and enhances safety for the operator. Depending on the electrolyte, hazardous substances can be produced, which often requires a vacuum hood for subsequent waste gas treatment. Using electrolytes with choline chloride and urea, an acrid smell may be noticed.

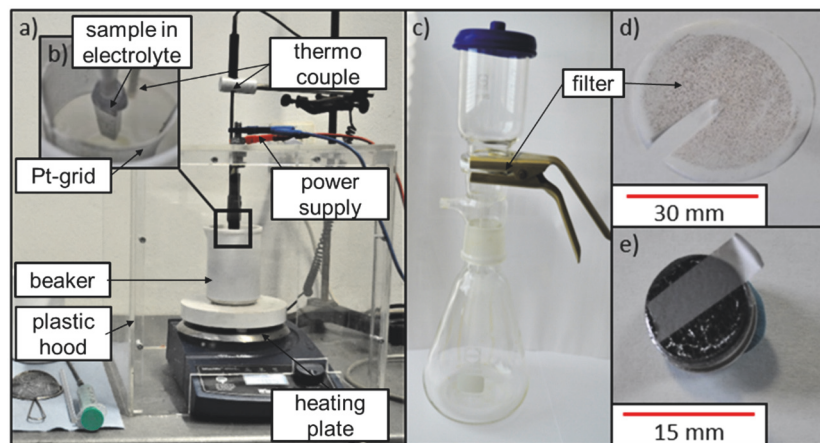


Figure 32: Installation for electrolytic extraction and filtrate processing.

Ongoing matrix material's dissolution can be monitored by decreasing sample weight and color changes of the electrolyte from clear to dark brown (Fe) or green (Cr). After 1 – 8 h, depending on the targeted dissolution volume, the electrolyte diluted with ethanol is filtered by a vacuum filtering device as seen in Figure 32 c). 12 μm , 1 μm , and 0.4 μm polycarbonate filters were used to separate different size classes. During electrolytic extraction, products as FeCl can be created at high current densities at the sample, so an intensive washing sequence during every

filtering step is necessary. In the end, the polycarbonate filters are treated by a drying procedure for 8 h at 60°C to decrease remaining humidity to a minimum. If large filter areas are analyzed and highest image quality is required, carbon sputtering is recommended. For qualitative analysis, the non-metallic inclusions can also be peeled off the filter with conductive tape. Due to the selective and adjustable extraction parameters, electrolytic extraction combines the best potential for Fe-content evaluations. Oxidic non-metallic inclusions in Figure 33 show excellent results of the performed electrolytic extraction. There, any indication of dissolution effects can be seen by the remaining morphology of particles after extraction.

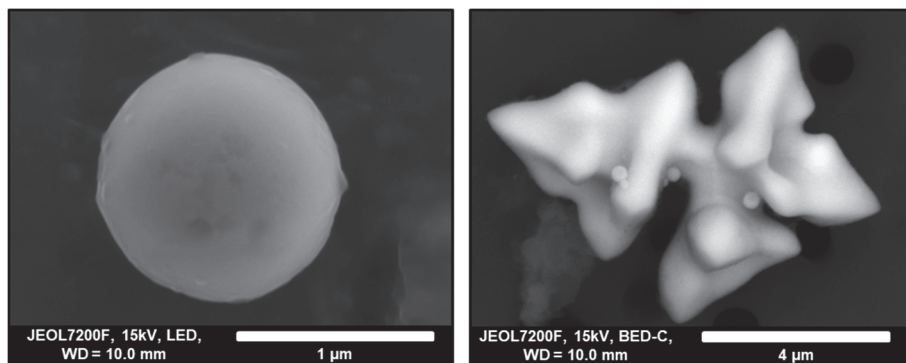


Figure 33: Electrolytic extracted non-metallic inclusions enabling exceptional particle analysis.

Advantages and disadvantages of electrolytic extraction can be summarized as follows:

- Selective extraction parameters can be adjusted.
- High dissolution speed is realized by non-aqueous electrolytes.
- Generally good stability of inclusions except for sulfides can be noted.
- A high amount of non-metallic inclusions is gathered on various filter steps.
- Automated inclusion analysis can be performed on filters.
- No chem. or morph. influence on (Fe,Mn)O inclusions (10-90 %FeO) is detected [93].
- Magnetic stirrer during extraction procedure causes morphological demolition.
- The low viscosity of cooled electrolyte causes a long-lasting filter procedure.
- Sample cleaning can be difficult due to often low viscous electrolytes.

4.5.2 Chemical Extraction Applied to Heterogeneous Oxy-Sulfide Inclusions

A rather simple but effective way to isolate non-metallic inclusions is by chemical extraction. In general, samples of approx. 1cm³ in size get deposited in acid solutions for hours or days. An interim weighting of the sample can monitor the dissolution progress. Parameters as temperatures, acidity, or pH-values are essential for differential dissolution of the matrix without

affecting non-metallic inclusions. Most methodologies described in the literature are based on HCl or HNO₃ solutions extracting rather stable particles (oxides or carbides). Due to their high tendency of instability in acids, sulfidic particles were dissolved in most experiments performing chemical extraction (see Figure 34) [119,126,151,152].

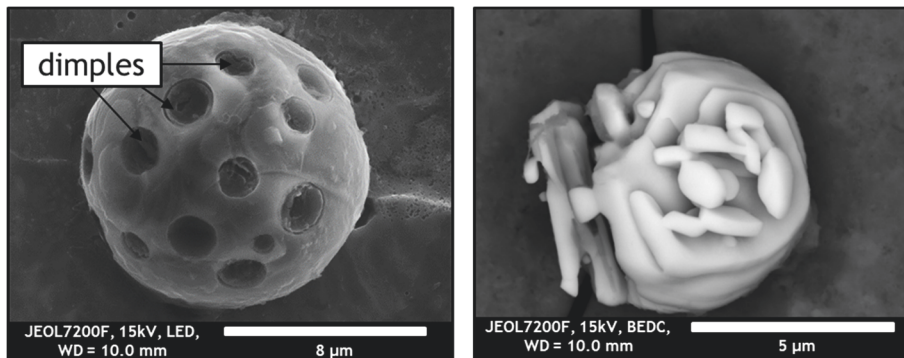


Figure 34: Oxidic inclusions with dissolved sulfide regions resulting in dimples and missing phases.

For improved steel cleanliness evaluations after extraction, this influence can cause allocation of clusters or agglomerates, resulting in changed interpretations. After a literature study on sulfides' chemical extraction [153–155], an improved methodology is formulated in this thesis. Dissolution with 5 % nitric acid showed the best results [128] amongst other acids. Nitric acid provides easy handling and availability due to the relatively low acidity and everyday use in metallography for etching. A sequential extraction procedure was created to optimize the exposure of inclusions to the solution. The steel sample is positioned in a beaker without stirring. Every 15 minutes, the area around the sample with visible extraction residues is sucked into a pipette and then injected into a 250 ml volume of ethanol for reaction inhibition. This sequence is performed until enough bulk material is dissolved for representative results. In the end, the already described subsequent filtering and washing steps are applied. Alternatively, the pipette volume can be injected directly into the filtering system followed by ethanol washing for inhibition, as illustrated in Figure 35.

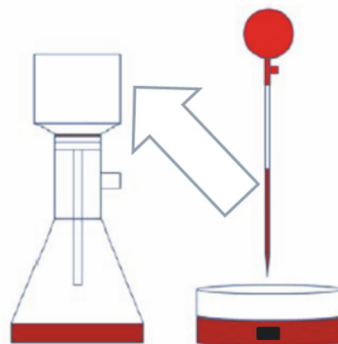


Figure 35: Methodology of sequential chemical extraction.

A permanent dissolution of the steel matrix with minimum exposure time for the non-metallic inclusions is realized, applying the developed sequential extraction. Analysis of clustered and complex structured non-metallic inclusions containing a significant amount of sulfidic phase shown in Figure 36 significantly improves the metallurgical knowledge of proceeding inclusion reactions. The high manual effort with easy application privileges the sequential chemical extraction for spot testing and sulfide containing cluster analysis [128].

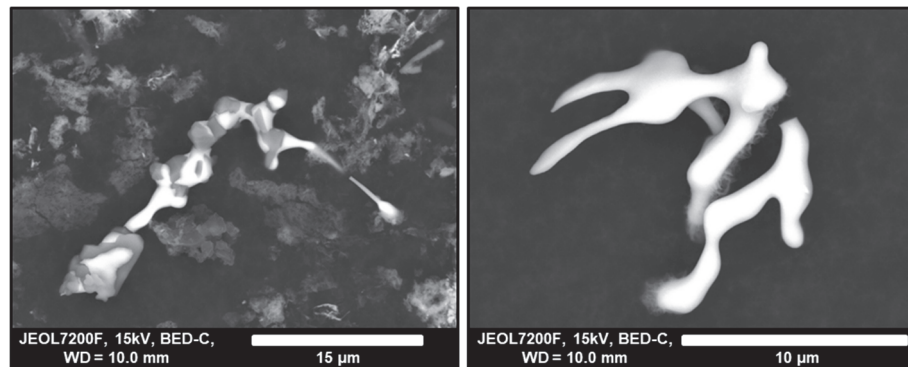


Figure 36: Clustered and complex sulfide inclusions after sequential chemical extraction.

The described morphology has also been applied for the extraction of oxidic inclusions and their MnS nucleation sights caused by solidification. Element concentration mappings in Figure 37 indicate MnS nucleation sights at cross-section analyses. After electrolytic extraction, originally only dimples are found on extracted inclusions (Figure 34). Only by chemical extraction applied in 15 min sequences, these nucleation sights can be analyzed without the surrounding steel matrix.

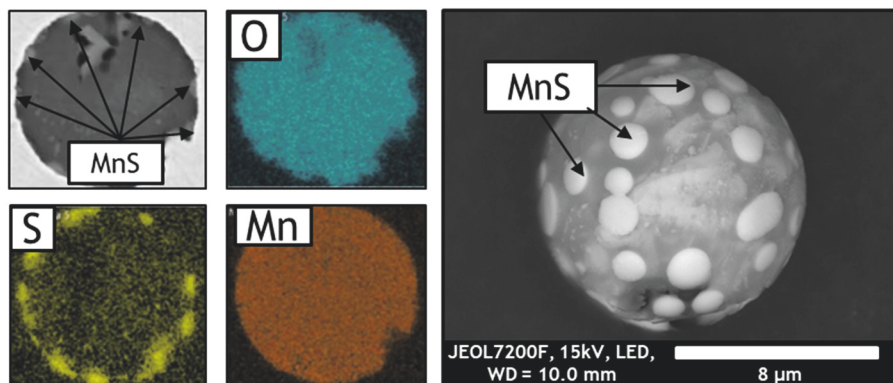


Figure 37: (Mn)OS inclusion in cross-section and after sequential chemical extraction.

To further improve the analysis of steel nucleation at non-metallic inclusions, the dissolution sample itself can be analyzed after cleaning off the electrolyte. Examples for evaluations are shown in Figure 38. MnS and bonding to the steel matrix can there be evaluated.

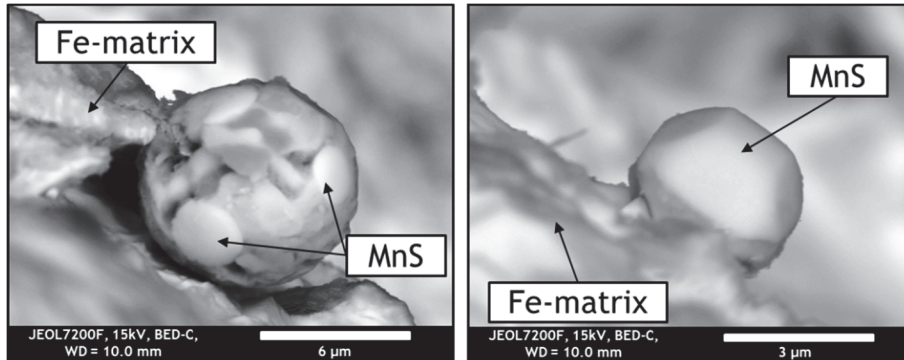


Figure 38: NMI still attached to extraction sample.

Evaluating heterogeneous non-metallic inclusions, poor bonding between sulfide and oxide phase must be considered peeling inclusions off the filter by conductive tape. Figure 39 illustrates an oxidic inclusion with lost sulfide regions.

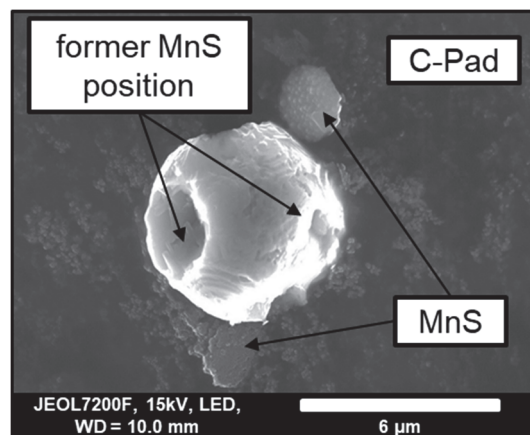


Figure 39: Particles with dissolved or lost MnS.

Additionally, noble elements solute in steel (e.g., Cu) can cause deposition effects on sulfidic inclusions during extraction by general chemical affinity. Similar effects were also observed by Luo et al. [156].

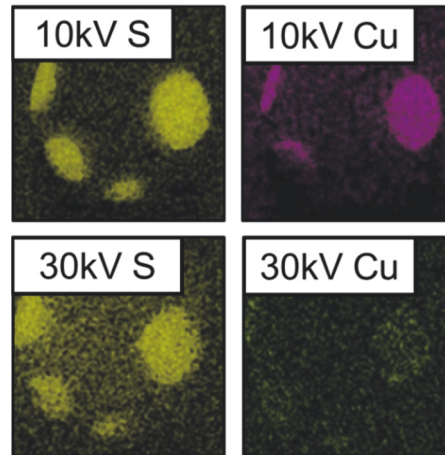


Figure 40: EDS concentration mapping at 10 kV and 30 kV.

Figure 40 illustrates the Cu-layer phenomenon's appearance by concentration mappings applied with different acceleration voltages. For quantification, Cu can be neglected and does not hinder any evaluations. The following advantages and disadvantages can be summarized:

- Extraction can be performed over night.
- Easy handling enables a promising application for spot-checking.
- Stability of sulfide particles is proven by heterogenous oxide-sulfide inclusions.
- An easily removable acid solution enables evaluation of NMI attached to the matrix.
- Evaluation of large agglomerates or inclusions bonded by sulfidic phases is possible.
- Poor bonding between sulfidic and oxidic non-metallic phases is detected.
- Cu-layer deposition is detected.

4.5.3 Twinjet-Polishing Performed as an Additional Dissolutive Preparation

An additional device for matrix dissolution was improved and verified by evaluating different preparation methods. Twin-jet polishing was used as a preparation sequence for high-quality thin foils. Generally, this methodology is applied to samples for transmission electron spectroscopy. First, plates with 80 – 120 μm thickness are produced by cutting and grinding. After a stamping procedure, 3 mm discs are installed in a twin-jet electro-polishing device for electrochemical dissolution. The sample is polished in a Struers TenuPol-5 by a 90 vol% perchloric acid and 10 vol% methanol electrolyte till perforation point (Figure 41). Near the perforation, the electron transparent area caused by continuous sample thinning emerges.

During SEM analysis, this area can be identified by decreasing brightness. Around the perforation, non-metallic inclusions are found barely holding on to the sample without any bulk material above or below. Due to the massive time effort for sample preparation, this method may only be used for particular research tasks, including high number particle populations [93].

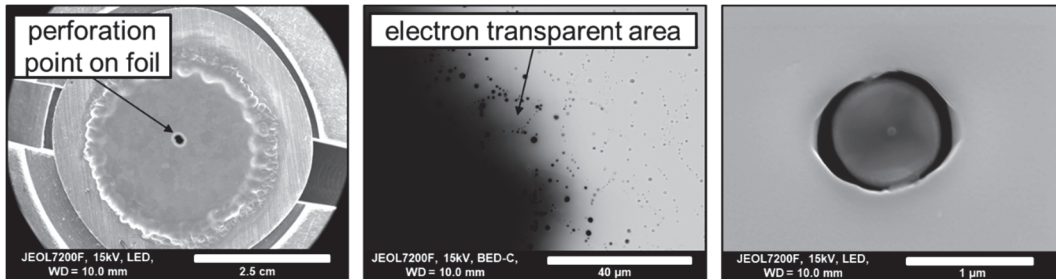


Figure 41: Twin jet polished sample in different magnifications.

The key acts of electro twinjet polishing are summarized as:

- Particle populations with high amounts and small sizes can be analyzed qualitatively and quantitatively without steel matrix interaction.
- TEM analysis for the highest magnification can be applied directly to these samples.
- The possibility of particle analysis with and without matrix interaction on one sample enables reference measurements in a single pass.
- General etching effects allow additional interpretations and correlations.
- Unpredictable perforation position might occur.
- Aluminum sample holders can create Al-background noise, minimizing the possible output and hindering AI quantification for inclusions.

4.6 Production of Inclusion Standard and Reference Samples Enabling Quantification of Matrix Interaction

One of the Ph.D.'s particular tasks is to deal with the fundamental question of how accurately iron content quantifications can be applied to non-metallic inclusions. Inspired by calibration procedures of measuring devices and dealing with bulk material interaction influencing EDS outputs at a specific inclusion size, a new referencing approach is developed, including comprehensive sample selection accompanied by thermodynamic and kinetic calculations. A reproducible and verifiable procedure for non-metallic inclusion standard and reference sample production is developed. An innovative referencing approach of detected composition

fluctuations caused by matrix interaction during EDS analysis is implemented on cross-section samples for (Fe,Mn)oxide inclusions with different Fe contents.

4.6.1 Sample Selection, Including Thermodynamics and Kinetics

Based on a preceding literature study and metallurgical knowledge, properties for non-metallic inclusion population possibly functioning as a reference and standard sample are defined. According to the following characteristics of the Fe-Mn-O system, Mn deoxidation is identified as most suitable to create non-metallic inclusion populations for standard sample production:

- Fe-Mn-O phase diagram database for thermodynamic calculations is verified [157].
- The Iron content in inclusions is controlled by the deoxidation level of the melt.
- Non-metallic particles form homogeneously.
- Particle formation and behavior can be described in kinetic calculations [32].
- Equilibrium conditions at high temperatures are achievable in experiments.
- Distinctive morphology of NMI enables easy identification after extraction [158].
- Generally high chemical stability of NMI in various electrolytes can be assumed.

At first, fundamental considerations are done based on the Fe-Mn-O phase diagram. Using Factsage 7.3 Equilib, including FSstel and FToxide database (2019), the ternary system's relevant section is illustrated according to thermodynamic data (Figure 42). An overview of possibly stable phases at different temperatures is given. Depending on the marked equilibrium compositions of samples 1 to 7, an increasing Mn/O ratio results in different particle origins during solidification. The inclusion population differentiates by the amount of liquid (slag) and solid (mono) inclusions during solidification. According to Steinmetz et al. [158–160], different oxygen activities during particle formation result in differing dendritic or faceted shaped oxide inclusions.

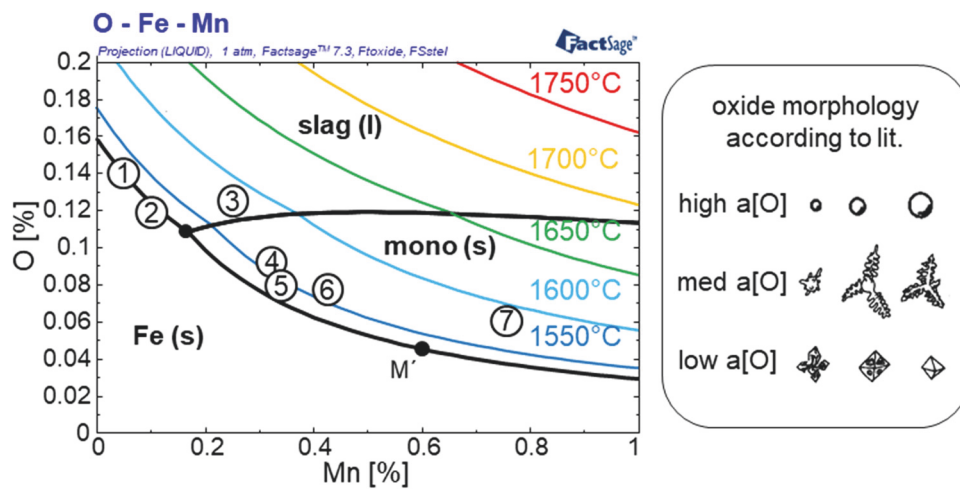


Figure 42: Phase diagram and Mn oxide morphology depending on oxygen activity [157,158].

Confirming the reduced stability of non-metallic phases with increased temperature, equilibrium conditions can be guaranteed for all sample compositions above 1600°C. Steinmetz et al. [157] reported slow cooling conditions could result in changed FeO contents. Increasing %FeO during solidification can be expected below the inflection point M', increased %MnO content can be expected above 0.6 %Mn. A study to evaluate possible changes of inclusions' compositions during solidification was achieved by the application of a model proposed by You et al. [32,34,161] coupling thermodynamic equilibrium conditions and solute enrichments in the residual liquid using an improved version of Ohnaka's model [162]. Liquidus temperature composition ($f_s=0$) was calculated based on mentioned Factsage equilibrium calculation. At each solidification step, the local partition and diffusion coefficients were considered resulting in a stepwise calculation of particles' compositions as illustrated in Figure 43. Theoretically dealing with segregation and enrichments in the remaining liquid for 0.105 %Mn and 0.119 %O, an increase of FeO is predicted.

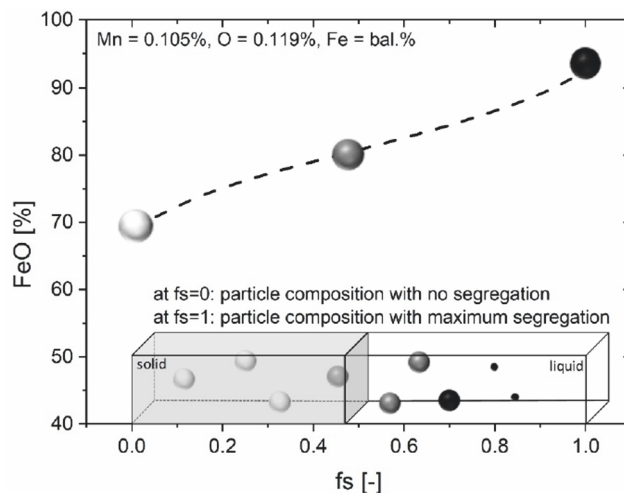


Figure 43: Calculated Fe segregation effects during solidification.

Possible changes of each thermodynamically stable NMI phase for all samples are calculated and listed in Table 6 for cooling speeds of 10 K/s corresponding to the equipment used for sample production.

Table 6: Predicted wt%FeO composition ranges (10 K/s)

Nr.	Mn/O	Slag fs=0	Slag fs=1	Mono fs=0	Mono fs=1
1	0.357	83	97	-	-
2	0.882	70	92	-	-
3	1.978	60	85	41	54
4	3.496	45	75	30	45
5	4.252	40	70	30	45
6	5.351	35	65	24	45
7	12.422	21	22	14	17

Liquid Slag phase inclusions with a general higher FeO content possibly occur in all samples. Mono inclusions with a generally higher MnO content can increasingly be detected with higher deoxidation potential of Mn before solidification [93].

4.6.2 Production of Non-Metallic Inclusion Standards for Fe Quantification

The representative production of metallurgical NMI standard samples is performed based on the holistic overview of influencing parameters for particle formation described in Section 4.1. To eliminate most system-related effects on (Fe,Mn)oxide formation, a Lifumat Met.3 high-frequency-remelter (HFR; Linn High Term GmbH) is used for 60g sample production. In combination with non-aqueous electrolytic extraction, according to Section 4.5.1, all requirements for verifiable and reproducible standard sample production are fulfilled. Figure 44 illustrates the formulated procedure:

- SEM/EDS cleanness evaluation performed on high purity electrolytic Fe (99.99 %Fe, Allied Metals) and Mn (99.98 %, Alfa Aesar) affirms purest input materials without preexisting non-metallic inclusions, inhomogeneities or segregations.
- Al₂O₃ refractory and inert Ar-atmosphere avoids the formation of exogenous inclusions.
- The enclosed furnace system without additional material input, intense high-frequency stirring, and superheating to 1650°C ensure high-temperature equilibrium conditions before solidification.

- Spin casting into a copper mold ensures constant heat transfer (10 K/s) and consistent cooling conditions for non-metallic inclusion formation.
- 4 minute solid-liquid-solid time enables controllable and reproducible sample production with only marginal influence of solidification effects.
- Chemical analysis of the final samples performed by emission spectroscopy and LECO combustion tests for total oxygen contents enabled composition evaluation with the highest accuracy.
- Subsequent sectioning and metallographic sample preparation with SiC grinding and diamond polishing cloths provided standard surface conditions for cross-section composition measurements (CS-reference) according to the guideline in Section 2.1.
- Electrolytic extraction followed by SEM/EDS analyses on the filtered particles according to Section 4.5.1 enables composition measurements without steel matrix interaction during analysis (STD).

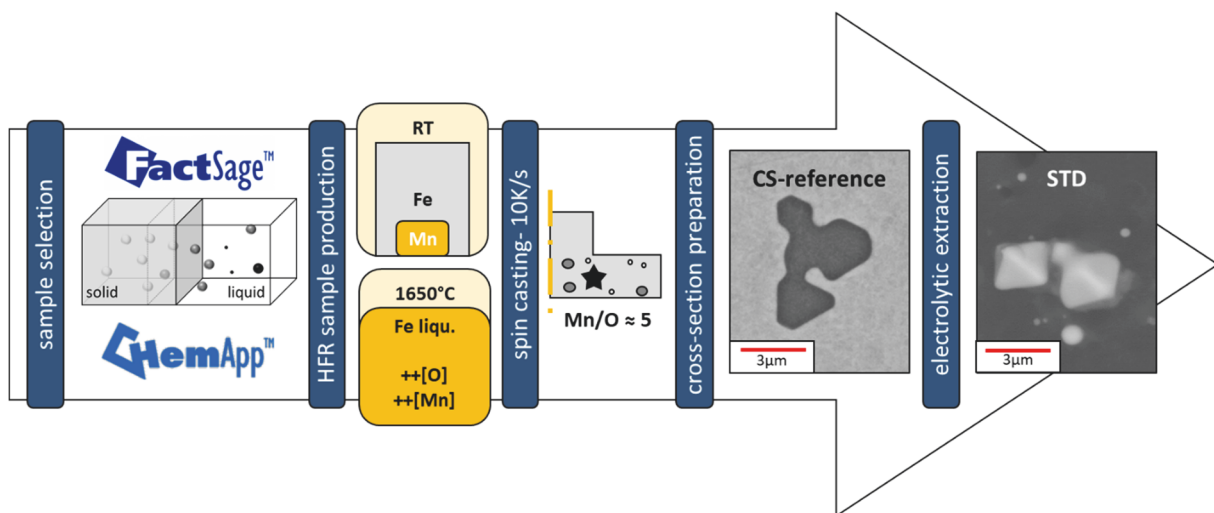


Figure 44: Methodology of NMI reference and standard sample production.

4.6.3 Evaluation of NMI Standard Samples

Well-considered sample selection combined with proficient melting metallurgy and metallographic effort enables the development of non-metallic inclusions reference and standard sample pairs with different FeO ratios. Figure 45 compares calculated composition ranges for different Mn/O ratios and inclusions' measured composition at cross-section (CS) and extracted (STD) form. On the one hand, steel matrix interaction is avoided by evaluation of (Fe,Mn)O particles > 2 µm to ensure matrix-free EDS analysis. On the other hand, particles in the range of 0.3 - 0.5 µm are analyzed to quantify the influence of matrix interaction at particles close to the detection limit of automated inclusion analysis. Table 7 lists the defined

non-metallic inclusion classes produced by Mn deoxidation. In general, spherical shapes can be easily differentiated from faceted or dendritic inclusions. Furthermore, the first quantifications of matrix interference during EDS analysis at sizes of 0.3 - 0.5 μm can be evaluated.

Table 7: NMI populations in Mn deoxidized melts

NMI Characteristics	Inclusion Classification
Dendritic or Faceted > 2μm	A (CS = cross-section reference; STD = extracted standard)
Spherical > 2μm	B (CS = cross-section reference; STD = extracted standard)
All Shapes 0.3 - 0.5 μm	C (CS = cross-section reference; STD = extracted standard)

According to the applied segregation model results in Figure 45, the calculated %FeO values are illustrated by composition ranges for liquidus ($f_s=0$) and solidus ($f_s=1$) temperature. The difference is caused by calculated oxygen segregation in the remaining liquid during cooling resulting in a general FeO increase. Particle compositions of A-CS and B-CS inclusions, unaffected by the surrounding matrix, conform to the calculated theoretical %FeO values. The kinetic model approach, the defined size range for matrix-free measurements, and the used databases are verified and affirmed. At Mn/O = 12.4, a lower FeO content is noticed, which may be caused by enhanced Mn segregation not being entirely considered in the model. As expected, an increased matrix interaction is detected at C-CS inclusions influencing the detected chemical composition resulting in massive FeO overestimation. Compared to cross-section analysis, chemical compositions gathered on extracted A-STD, and B-STD particles show no indication of chemical or morphological changes caused by electrolytic extraction. EDS fluctuations at particles' three-dimensionality can cause minor deviations. Electrolytic extraction enabling measurements without bulk material massively improves C-STD compositions compared to C-CS %FeO values. Therefore, sub-micro inclusion evaluation is performed quantitatively and quantitatively.

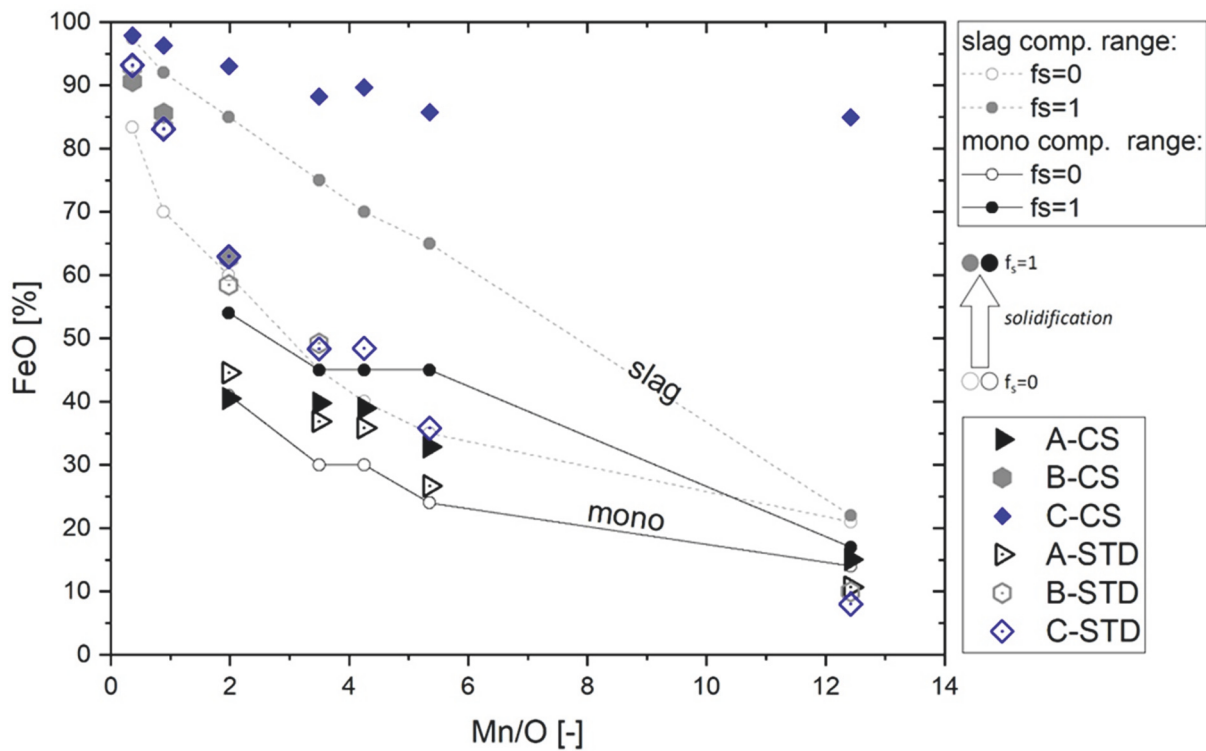


Figure 45: Calculated and measured FeO contents.

To evaluate changes in morphology and chemical composition caused by varied deoxidation potential and segregation effects during cooling. In Figure 46, the resulting inclusion populations in cross-section and extracted state are displayed. The changes in inclusions morphology with increasing Mn/O ratio are similar to publications of Steinmetz et al. [158]. Actually, an additional faceted inclusion state at medium Mn/O ratios is observed. The present morphology chronology (spherical – faceted – dendritic) correlates better to a developing interface instability caused by supersaturation than Steinmetz's published theory: spherical – dendritic – faceted. At lowest oxygen activities reported faceted inclusions by literature might be correlated to Fe and Cr's combination for deoxidation. In the present case, low oxygen activities are realized by Fe-O master alloys with different total oxygen contents and single Mn deoxidation, creating pure (Mn,Fe)oxide inclusions. The observed additional morphology type should be considered in future research dealing with manganese deoxidation or interface instabilities.

To verify calculated segregation in emerging non-metallic phases, compositions of largest and smallest inclusions are correlated considering the particles' origin within a single melt (Mn/O ratio). In general, inclusions $> 2 \mu\text{m}$ can be assumed to be particles formed at liquidus temperature ($f_s=0$). These are easy to identify by their size and shape (Figure 46). Inclusions with $0.5 - 0.3 \mu\text{m}$ can be assigned to formation near solidus temperature ($f_s=1$). The chemical

difference calculated according to Equation 7 quantifies the detectable kinetic effects. So, the performance of the applied kinetic model can be evaluated.

$$\Delta FeO^{fs(1,0)} = FeO^{(fs=1)} - FeO^{(fs=0)} \quad (\text{Eq. 7})$$

As illustrated in Figure 46, FeO increase can be detected at melts with Mn/O ratios of 3.4 – 5.3 considering an EDS scattering of 3.7 % [93,163] caused by three-dimensional effects at extracted NMI particles. At a Mn/O ratio of 12.4, a MnO increase was detected. The assumed particle composition changes of literature are in good general accordance with the quantified composition changes.

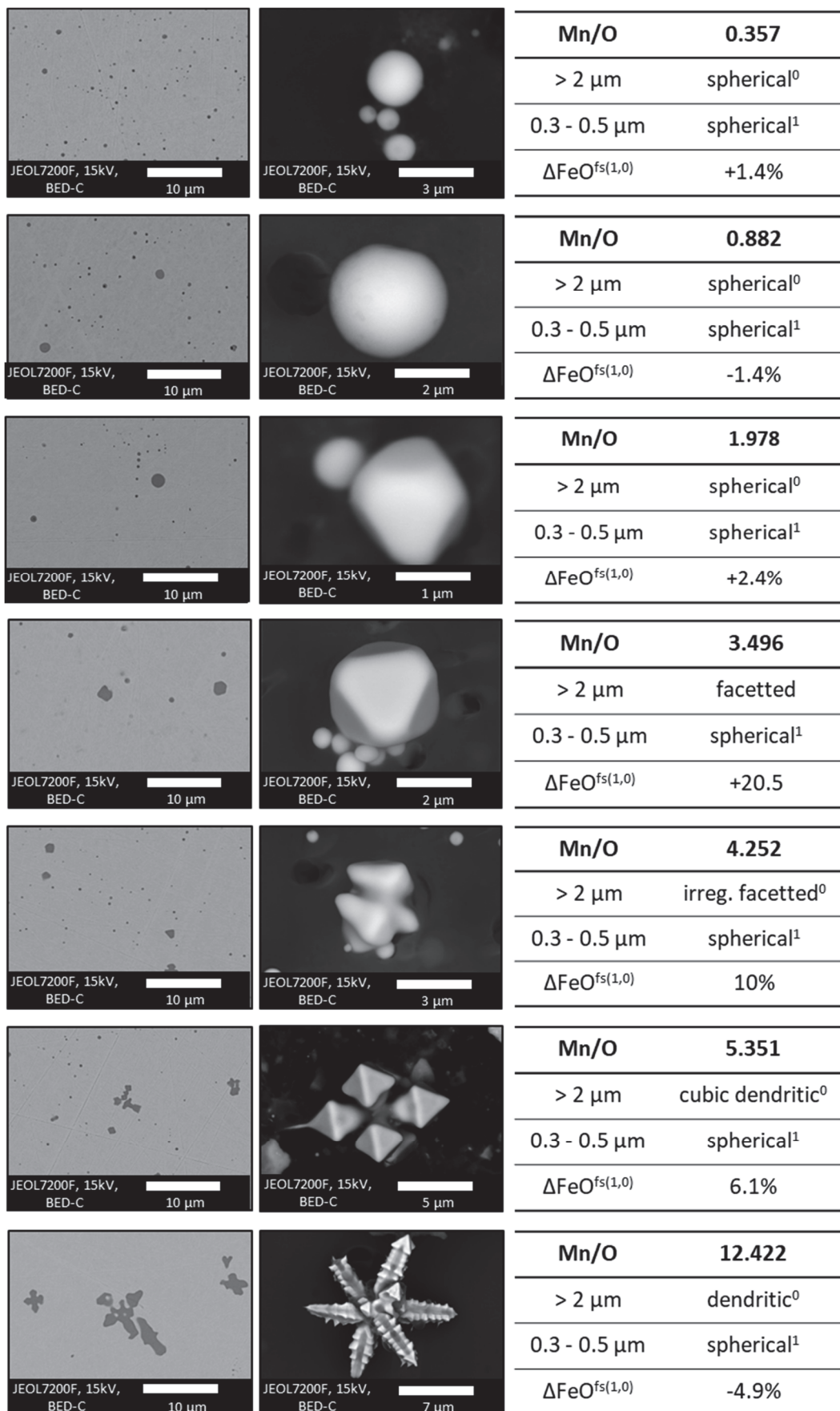


Figure 46: Morphologies of CS and STD samples depending on Mn/O ratio.

Applying a different evaluation approach, CS- and STD- measurement results are displayed in Figure 47. The gathered FeO values of A, B, and C particles after electrolytic extraction are contrasted to their corresponding reference measurement on cross-section samples. The visualization of the quantified error caused by matrix interaction at single point EDS analysis is demonstrated by Figure 47, showing the resulting correlative positions.

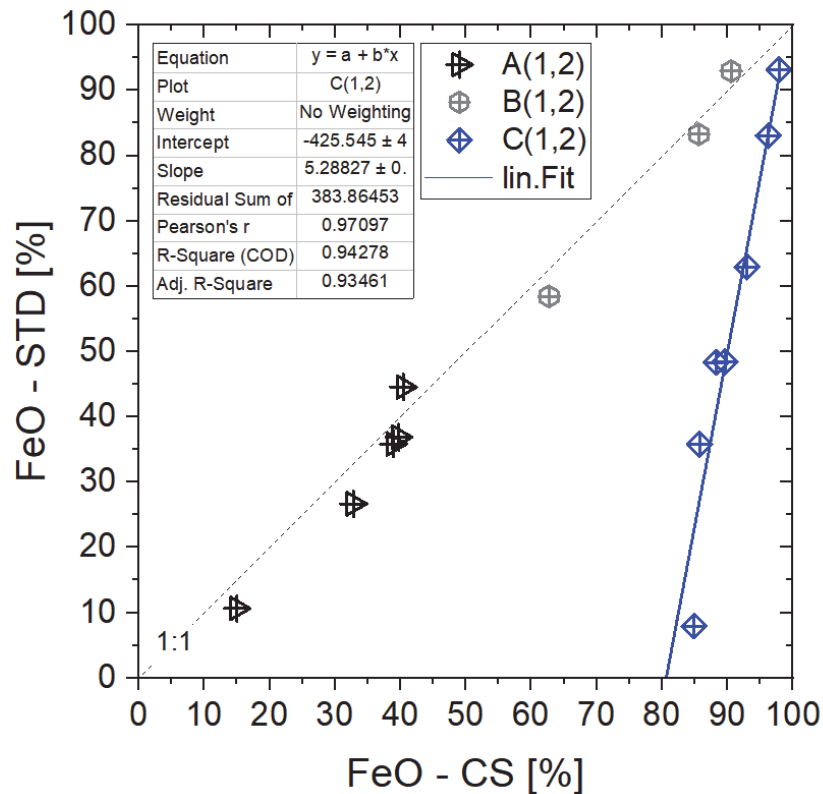


Figure 47: Referencing cross-section and extracted compositions detected [163].

Inclusion sizes without matrix interaction are located along the 1:1 meridian. On the one hand, minimum differences to the meridian eliminate any doubts of electrolytic extraction affecting the (Fe,Mn)oxide composition. On the other hand, the formulated methodology as reproducible and applicable even for high Fe contents in oxidic inclusions is confirmed. The general matrix interaction error of automated single-point analysis at non-metallic inclusions in a sub-micro size range of 0.3 - 0.5 μm can be extrapolated to 80 %.

4.7 Matrix Correction for Automated Inclusion Analysis

Area scan settings are the most suitable way to gather chemical compositions of a high number of different heterogeneous inclusions (e.g., Al_2O_3 with MnS nucleation) to answer challenging metallurgical processes and research tasks by inclusion analytics. In the current setup and suitable for most steel cleanliness evaluations, 15kV acceleration voltage is used. An unavoidable negative side effect of area scan settings is an increased matrix interaction limiting the qualitative and quantitative output of every single analysis. A detailed description of forming interaction volumes in non-metallic inclusions and the surrounding bulk material can be found in Section 3.5. In general, the detected iron content (Fe^{EDS}) of a performed measurement is a combination of the actual content in the particle itself (Fe^{NMI}) and the amount caused by matrix interaction ($\text{Fe}^{\text{Matrix}}$) according to Equation 8:

$$\%Fe^{\text{EDS}} = \%Fe^{\text{NMI}} + \%Fe^{\text{Matrix}} \quad (\text{Eq. 8})$$

With decreasing particle size, the falsification caused by matrix influences increases (Section 3.2). Therefore, a central task of this thesis is to develop a mathematical correction for matrix interaction based on the gathered knowledge described in Sections 3.2, 3.5, 4.2, and 4.3. Input parameters for the equation are morphological parameters and the chemical composition obtained by automated inclusion analysis. As displayed in Figure 48, the matrix interaction can be divided into two main volumes. On the one hand, a matrix interaction ring appears caused by the scanning method. Dimensions of this ring are defined by the electron acceleration voltage, particle size, shape, and matrix composition. On the other hand, the amount of iron information caused by the matrix beneath the non-metallic inclusion is influenced by the cutting position, morphology, size, and matrix composition.

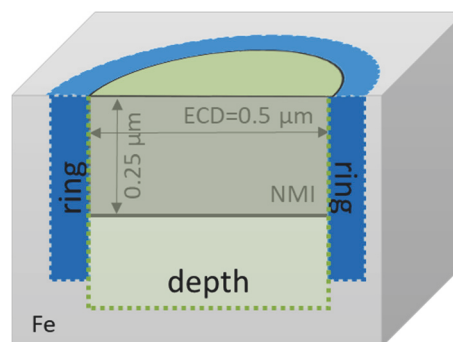


Figure 48: Considered matrix interaction at area scan measurements.

The measured iron content caused by matrix interaction ($\%Fe^{\text{matrix}}$) can be quantified by Equation 9.

$$\%Fe^{matrix} = \%Fe^{ring} + \%Fe^{depth} \quad (\text{Eq. 9})$$

The remaining particle depth after sectioning cannot be explicitly defined by any parameter gathered by automated inclusion analysis. In the present work, the particle's depth was approximated by half of the inclusion equivalent circle diameter (ECD/2).

A stepwise correction is described in the following sections, applying a methodology of an ordered *ring correction* followed by *depth correction*. With the correct sequence of applied calculations, the evaluation of the improved composition value can be monitored. A massive over or underestimation of certain elements can be easily identified, and the equations can be adapted if needed.

4.7.1 Interaction-Ring Correction

The first correction step includes a geometric consideration of the EDS interaction, so the actual X-ray interaction volume for every inclusion is defined. Simplifications are needed to consider the rather undefinable gradient inside the interaction bulb. Based on the intensity curves in Section 4.2.1, a 100 % interaction density is assumed as equal to a third of the volume, including a gradient. Hence, after an interaction path of $z/3$, all X-ray information is generated and detected. Figure 49 a) illustrates the simplifications applied to the bulb. The appearing interaction ring surrounding particles is mainly defined by the electron bulb's size in the matrix material using AScan settings for measurements (Figure 49 b and c).

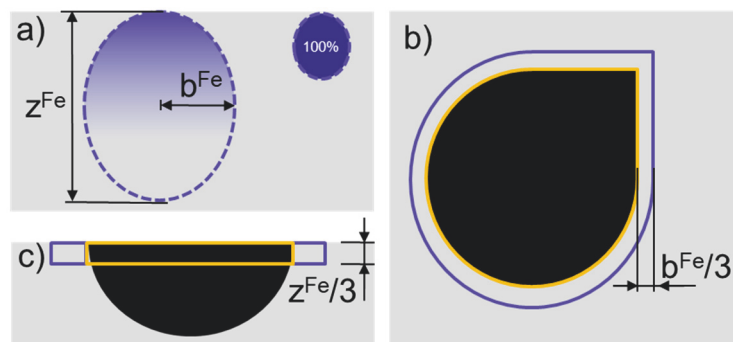


Figure 49: reduced interaction dimensions.

According to Equation 10, the interaction ring is defined by the inclusion's perimeter, $z^{Fe}/3$ (interaction depth), and $b^{Fe}/3$ (interaction width), including geometrical simplifications.

$$V^{ring} = \frac{b^{Fe}}{3} * perimeter * \frac{z^{Fe}}{3} \quad (\text{Eq. 10})$$

The corresponding volume inside the inclusion (V^{nmi}) is calculated by Equation 11 considering the actual detected particle area and the matrix's reduced interaction depth.

$$V^{nmi} = area * \frac{z^{Fe}}{3} \quad (\text{Eq. 11})$$

By simplifying the generated volumes to almost two-dimensional relations, the generated ring volume and the appearing particle area can easily be correlated. Using actual detected dimensions and perimeter values enables consideration of elongation or irregularity influences. Calculating the volume ratio (V_r) according to Equation 12, the matrix and particle interaction share can be quantified.

$$V_r = \frac{V^{ring}}{V^{ring} + V^{nmi}} \quad (\text{Eq. 12})$$

In the following Table 8, all steps and results of an exemplarily applied ring correction are listed. In the beginning, the parameters of the matrix surrounding the non-metallic inclusions are defined. In the present case, the steel composition is characterized with 99.9 %Fe and 0.1 %Mn. Other elements below 0.1 % like O, S, and N remain neglected due to their lack of detectability by lowest concentrations. The dimensions for the interaction bulb in the bulk material are calculated for 15 kV acceleration voltage. According to described Equation 12, the ratio V_r is determined and used for the first step of iron correction. The iron content after the first correction step ($\%Fe^{ring*}$) is calculated by Equation 13, correcting the initially measured content ($\%Fe^{EDS}$) by the calculated share and matrix interaction ($\%Fe^{matrix}$).

$$\%Fe^{ring*} = \%Fe^{EDS} - (\%Fe^{Matrix} * V_r) \quad (\text{Eq. 13})$$

The same procedure is done for all other elements in the bulk material, which may falsify the EDS result, in this case, Mn.

$$\%Mn^{ring*} = \%Mn^{EDS} - (\%Mn^{Matrix} * V_r) \quad (\text{Eq. 14})$$

After applying the mathematical correction for Fe and Mn, the composition values are normalized to 100 % and defined as $\%Fe^{ring}$ and $\%Mn^{ring}$. In the end, the calculated and normalized concentrations of the corrected composition can be seen in Table 8. After the mathematical correction, the element concentrations have already improved towards the composition of thermodynamic prediction and the reference values gained after electrolytic extraction (20 %O, 12 %Mn, and 68 %Fe).

Table 8: Application and results of ring correction

Defined Values	%Fe ^{matrix}	%Mn ^{matrix}	z ^{Fe}	b ^{Fe}		
	99.99	0.1	0.6	0.4		
Measured Values	Area [μm ²]	ECD [μm]	Perimeter [μm]	Fe ^{EDS} [%]	Mn ^{EDS} [%]	O ^{EDS} [%]
	0.074	0.308	1.005	89.36	2.79	5.32
Calculated Values	V ^{ring} [μm ³]	V ^{nmi} [μm ³]	V _r [-]			
	0.0268	0.0149	0.6428			
Normed Conc. After Ring Correction	Fe ^{ring} [%]	Mn ^{ring} [%]	O ^{ring} [%]	FeO ^{ring} [%]	MnO ^{ring} [%]	
	75.69	8.24	16.05	90.17	9.82	

Figure 50 displays the particle composition gained by EDS before and after the first correction for a micro and sub-micro inclusion population of (Fe,Mn)oxide inclusions. The original measured composition values colored in black show a massive matrix interaction with decreasing diameter. An increased iron content results in decreased Mn and O values.

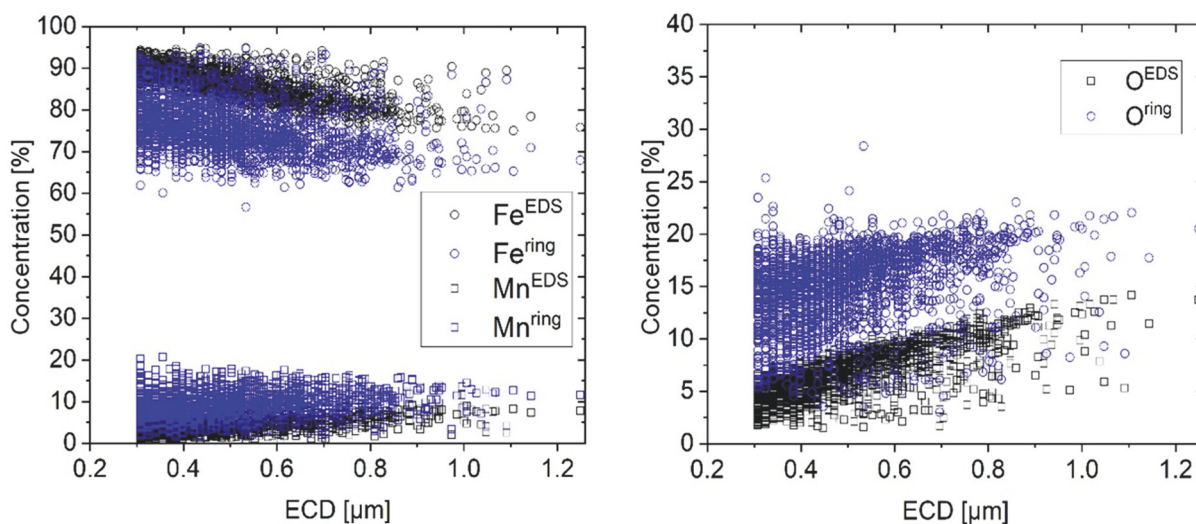


Figure 50: Detected and corrected particle composition.

After applying mathematical ring correction, the Fe concentrations are reduced, and Mn and O are lifted. The general particle compositions are improved. Particularly, the oxygen value can be seen as an indicator of the equation's suitability. The final result should be close to 20 % to fulfill thermodynamics and kinetics predictions.

4.7.2 Interaction-Depth Correction

After the applied ring correction step considering mainly geometric parameters, the composition data can further be improved using the gained knowledge of electrons and X-rays interacting with metallurgical samples. Based on the fundamental research done by casino simulation on physical effects, a method is formulated considering falsification caused by matrix interaction below non-metallic inclusions. During analysis, several physical effects need to be weighed for quantification. Cross-interaction of higher energetic radiation (Fe) and non-metallic phases and other phenomena described in Chapter 3 are investigated, simulating interaction bulbs of non-metallic inclusion layers on matrix material. The defined X-ray intensity ratio described in Section 4.2.2 by a Boltzmann approximation (equation 15) calculates the information gathered inside and outside the non-metallic phase (intensity split = I_s). The assumed particle depth of $ECD/2$ proved to be a reasonable assumption for the present inclusion population.

$$I_s = A_2 + \frac{(A_1 - A_2)}{1 + e^{\frac{\frac{ECD}{2} - x_0}{d_x}}} \quad (\text{Eq. 15})$$

According to Equation (16) and Equation (17), the second matrix correction is applied by multiplying the intensity split and the element concentration after the ring correction step.

$$\%Fe^{r+d*} = \%Fe^{ring} * I_s \quad (\text{Eq. 16})$$

$$\%Mn^{r+d*} = \%Mn^{ring} * I_s \quad (\text{Eq. 17})$$

After a normalizing step, improved particle composition ($\%E^{r+d}$) can be used for evaluations and interpretations. The following table summarizes input and output data of the second mathematical correction method.

Table 9: Interaction depth correction.

Defined Values	%Fe^{matrix}	%Mn^{matrix}	z^{Fe}	b^{Fe}		
	99.99	0.1	0.6	0.4		
Measured Values	Area [μm²]	ECD [μm]	Perimeter [μm]	Fe^{EDS} [%]	Mn^{EDS} [%]	O^{EDS} [%]
	0.074	0.308	1.005	89.36	2.79	5.32
Calculated Values	V^{ring} [μm³]	V^{nmi} [μm³]	Vr [-]			
	0.0268	0.0149	0.6428			
Normed Conc. After Ring Correction	Fe^{ring} [%]	Mn^{ring} [%]	O^{ring} [%]	FeO^{ring} [%]	MnO^{ring} [%]	
	75.69	8.24	16.05	90.17	9.82	
Intensity Split MnO	A1	A2	X0	dx	ls	
	-0.68559	0.99845	0.00312	0.11232	0.6499	
Normed Conc. After Ring & Depth Corr.	Fe^{ring+depth} [%]	Mn^{ring+deph} [%]	O^{ring+depth} [%]	FeO^{r+d} [%]	MnO^{r+d} [%]	
	69.67	7.59	22.73	90.17	9.82	

Figure 51 displays the resulting changes of the appearing particle composition after each correction step. The original EDS data shows intense matrix interaction depending on the particle size. After applying both correction steps, the mean %O value scatters around 20 % correlating perfectly to the calculated oxygen content for this inclusion composition. Increased scattering with a smaller diameter is probably caused by different cutting positions of the analyzed inclusions. According to Section 4.3.2, with decreasing size, it is more unlikely that spheres are sectioned in the exact center, resulting in thin and sunken particles unsuitable for approximating the depth by ECD/2. Additionally, evaluating the displayed particle sizes, a grouping of particles at 0.3 - 0.5 μm diameters stands out. Caused by picture digitalization, a narrowing effect of possibly detectable sizes is created.

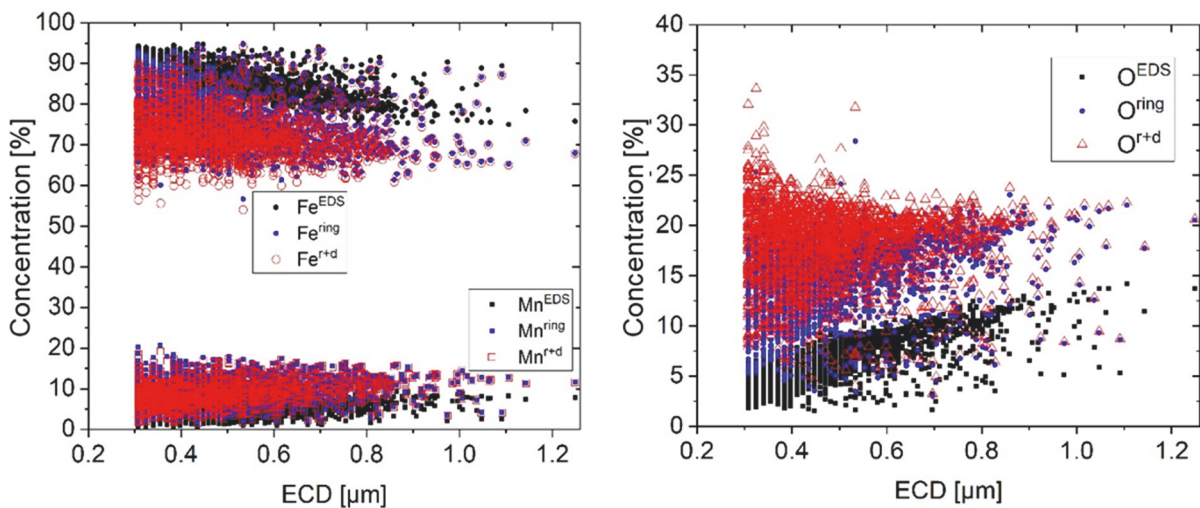


Figure 51. Concentration ranges at the correction of matrix interaction.

The general quantitative output correlates well with the thermodynamic and kinetic calculation and the composition values gathered by EDS after electrolytic extraction (20 %O, 12 %Mn, and 68 %Fe). It can be seen that by applying the ring and depth correction, the falsified inclusion composition is corrected to a significant extent.

4.7.3 Iron Correction Applied to Research Samples with varied Fe Content

To evaluate the formulated mathematical correction's performance, the procedure was applied to manufactured (Fe,Mn)oxide samples. The combination of high and low Fe containing inclusions with the great variety of particles' morphologies (spherical, faceted, and dendritic) enables verification of different effects on the corrections' output. Additionally, based on performed dissolution experiments, valid composition values are obtained by electrolytic extraction and EDS analysis.

To perform measurements for research and industry demands, automated inclusion analysis for inclusions $>1\mu\text{m}$ und area scan settings are executed and contrasted to corrected iron contents and compositions detected after electrolytic extraction in Figure 52. Box-whisker plots are used to show the shape of the composition distribution with marked mean and median values. Whiskers (10 - 90 %) and boxes (25 - 75 %) illustrate the most frequently measured %Fe contents of each inclusion population. In Figure 52, the initially detected Fe contents (%Fe^{EDS}) are displayed by blank box-whisker plots.

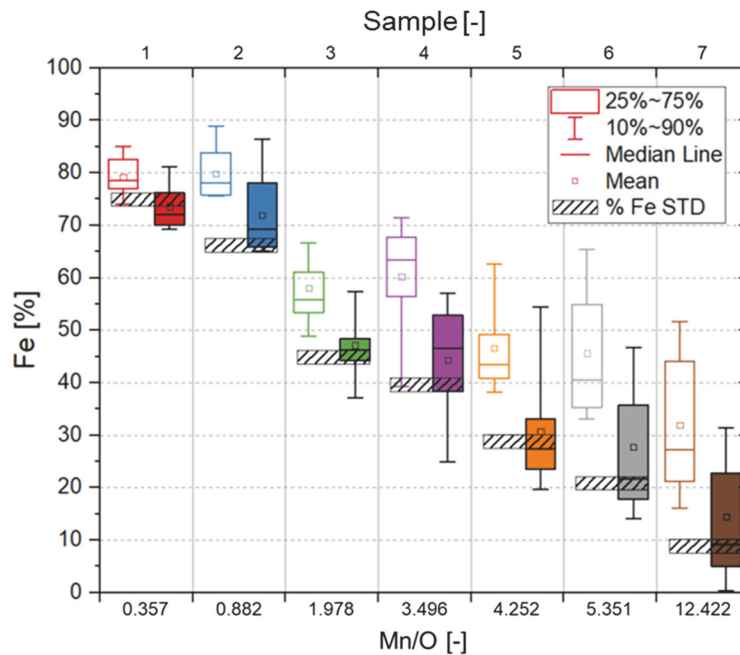


Figure 52: Detected Fe contents compared to electrolytic extraction and mathematical correction.

The iron content measured after electrolytic extraction (%Fe STD) is marked by a striped area including a 2.5 % range, considering increased scattering at three-dimensional structures [93,163]. An apparent difference between falsified cross-section feature compositions and extracted particles can be noted in the following diagram. After mathematical matrix correction illustrated by filled box-whisker plots, a noticeable improvement of the compositions is created. At almost all samples, the corrected data is closer to the “*valid*” composition. According to the displayed data, the formulated mathematical approach is unaffected by high and low Fe contents affirmed by the median value generally being near to %Fe STD value of each sample. Also, changing morphologies do not affect the correction of matrix interaction. The main improvement is the eliminated size effect minimizing the output of EDS data in general.

Applying matrix corrections to sub-micro particle populations do also show good results. Over/underestimation of Mn or Fe contents caused by increased oxygen scattering minimizes the quantifiable output. For evaluating compositions of sub-micro inclusions, electrolytic extraction is still more beneficial due to the relatively simple practical elimination of steel matrix interference.

For industry and research demands, mathematical matrix correction reveals excellent potential for future inclusion analytics. In a first step, the mean interaction formula given an Equation 15 can be used to evaluate and verify the formulated approach's implementation. To further improve the mathematical correction for different inclusions, including rare earth elements, additional intensity split simulations can be developed. Future improvements of processes,

research, and analysis, are apparent. Different approaches have been formulated to deal with matrix interaction including Pistorius et al. [110,141,142]. The present work breaks new grounds especially for automated inclusion analysis. The corrected data improves the possibility of interpreting and evaluating metallurgical tasks, including changes of solute or bonded matrix elements. Improved measurements of sub-micro inclusions enable descriptions of non-metallic inclusions compositions on a new level. This method combines simple calculations creating extraordinary helpful outputs for metallurgists and material scientists.

4.8 Morphology Categorization using M-Factors

In modern oxide metallurgy, besides particles' chemical composition, especially sizes and morphologies are known to be decisive to influence agglomeration, separation, and nucleation behavior of inclusions. Especially short-range orders of NMIs can be detrimental for the finished product in terms of material failure. At the moment, steel cleanliness standards only deal with sizes larger than 3 μm and morphologies based on optical microscope analysis for rolled products with a defined deformation ratio. The main objective is the identification of inclusion strings or clusters. Inclusion characteristics as greyscale, size, and particle neighbor distances depending on the rolling direction are distinctive to obtain a classification for micro and meso size regimes. Although modern SEM systems are firmly established in research and industry analytics providing comprehensive morphological data, any guidelines or standards are published, including specific morphological classification and typification based on automated measurement data. One present thesis's task is to formulate a detailed description of different inclusion morphologies in steel samples. For categorizing, innovative "*morphology factors*" (MF) depending on particles appearing concentricity, length, and perimeter are defined, and a guideline for spherical, elongated, and irregular particles is formulated. Using a dimensionless factor (MF1) as the basis for classification rules, this categorization can be applied to any size regime or inclusion type analyzed by any digital imaging system. A particular focus is put on good transferability to other microscope systems by defining limits in minimum pixels. Sub-micro, micro, meso, and macro inclusions can be categorized depending on the elongation and irregularity to quantify even slight changes in morphological appearance or early states of clustering and agglomeration.

First, image recording is performed based on the backscattered electron detector image of the sample (Figure 53). Depending on magnification and resolution settings, a minimum size range

is defined, often limits of 4 or 32 pixels equal to 1 μm are set. A minimum limit of 9 pixels is recommended for the best digital depiction of sphericities. In the present case, the detection limit results in smallest detected inclusions of 0.3 μm. Smaller particles can be detected, but subsequent EDS analysis would be massively affected in quality and quantity caused by described physical limits (Section 3.2). After image-recording, a greyscale threshold is defined to enable the automated system a differentiation between inclusion and surrounding steel matrix. This rather qualitative value should be chosen in a manner of good reproducibility. By the applied picture digitalization and threshold definition, the original form of inclusions is influenced by increased edge coarsening at decreasing particle size. The binary pixel picture is then used for morphological parameter definition, including length, breadth, area, and perimeter. For every single particle, the morphological and chemical data is detected and stored for evaluation.

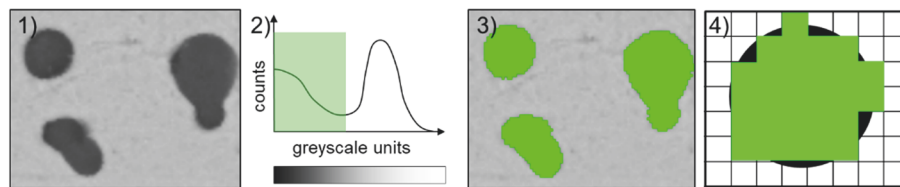


Figure 53: 1) Imaging, 2) Greyscale threshold application, 3) Binary imaging, 4) Illustration of edge coarsening caused by binarization.

Software packages (Aztec, Oxford Instruments) provide calculated morphological data, including “ECD” (equivalent circle diameter) or “shape” (sphericity) values. These are often too inconclusive for improved inclusion interpretation. The described categorization guideline is based on measured morphological parameters to improve inclusion analytics data interpretation. To avoid misinterpretation of the data, the coarsening effect is considered by a minimum limit of 21 pixels for morphology interpretation. Shape interpretation below the limit can result in falsely identified angularity. In general, the developed morphology classification differentiates spherical and elongated inclusions. If the ratio of length to width is larger than 1.55, the inclusion is defined as elongated. Different MF factors are calculated to achieve a better separation of morphological properties. The MF 1 factor calculated according to Equation 18 creates a dimensionless value related to a perfectly spherical appearing inclusion (ECD). This MF 1 value is the basis for subsequent morphology factor calculation considering angularity, irregularity, and increased harmfulness.

$$MF1 = \frac{perimeter}{area} - \left(\frac{2}{\frac{ECD}{2}} \right) \quad (Eq. 18)$$

By adapting the MF 1 factor by Equation 19 with the measured length, MF 2 is created, enabling categorization of elongated inclusions. Heavy elongation can be interpreted by higher appearing harmfulness.







$$MF2 = (MF1) * length \quad (\text{Eq. 19})$$

A significant advantage of the described morphology factors is the possibility of identifying differences between angular and irregular appearing inclusions. Adapting MF 1 to MF 3 with Equation 20, including the measured perimeter, quantifies the particles' morphology changes from spherical to angular or irregular.

$$MF3 = (MF1) * perimeter \quad (\text{Eq. 20})$$






With increasing MF 3 value, a more irregular particle interface can be identified. In Table 10, the vital thresholds for improved inclusion characterization for elongated non-metallic inclusions are summarized. As displayed by the following sketches, MF 2 and MF 3 values' combination enables categorizing characteristics in elongation and irregularity.

Table 10: MF values for elongated inclusions.

Elongated sketch	slightly elongated	slightly e. + irregular	elongated	elongated + irregular	extremely elongated and/or irregular
					
MF 2	< 5	< 5	5 – 29	5 – 30	30 ≤
MF 3	-	5 <	-	70 <	-

In Table 11, the defined threshold values for improved morphological categorization for spherical non-metallic inclusions are summarized. The inclusion sketches shall exemplarily display different possible forms of spherical inclusions. The formation of angular morphology or irregularities caused by particle agglomeration in the melt can now easily be quantified and evaluated based on MF3 values.

Table 11: Morphology factors (MF) for spherical inclusions

Spherical (s.)	s. < 21pxl	s. circular	s. angular	s. irregular	s. highly irregular
sketch					
MF 3	-	< 0,6	< 4	< 40	40 ≤

Examples of NMIs used for categorization development are listed in Appendix A.2 in **Table 19**. Cross-section analyses combined with changing particles' morphology (spherical – faceted – dendritic, Section 4.6) generate various NMI structures differing in irregularity and appearing aspect ratio. Quantification of MF values for research samples is listed in Table 12 for created (Fe,Mn)oxide standard samples. With a higher Mn/O ratio, increasing MF values can be noted. The application of perimeters and particle lengths as additional parameters enables a more accessible threshold definition for distinctive morphologies. The continuously increasing MF 2 and MF 3 values are in good accordance with visual impressions of inclusions (Section 4.6.3 and Figure 46) and literature assumed morphologies [158].

Table 12: MF values calculated for different (Fe,Mn)oxide populations.

Mn/O	MF 1	MF 2	MF 3
0.357	0.13	0.19	0.56
0.882	0.13	0.17	0.48
1.978	0.23	0.63	1.95
3.496	0.35	0.65	1.91
4.252	0.29	0.75	2.15
5.351	0.42	1.13	3.43
12.422	0.50	2.73	6.66

The morphological classification and typification developed in this work quantify even slight changes in inclusions' appearance. According to Figure 54, low Mn/O ratios, for instance, result in mainly s.circular inclusions. With a higher deoxidation potential of the melt, more angular inclusions are formed. At Mn/O-ratio of 12.4, dendritic inclusions result in an increase of irregular, slightly elongated, and elongated detected features, affirming the defined thresholds of Table 10 and Table 11.

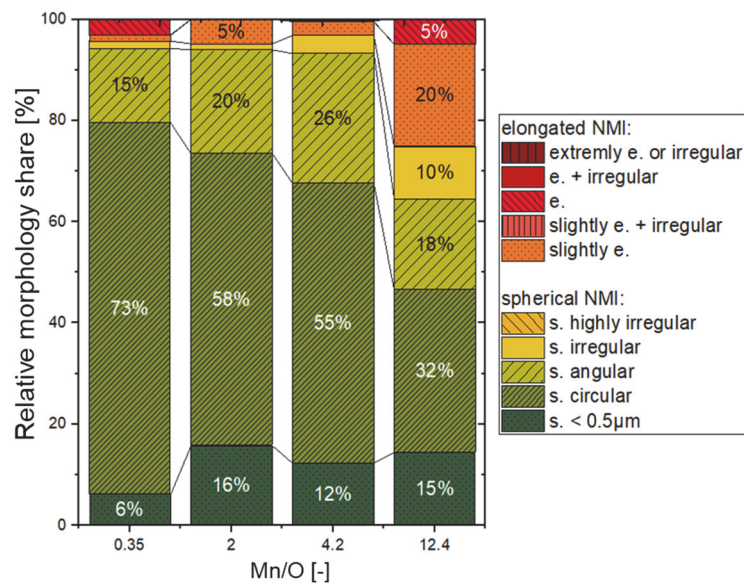


Figure 54: MF categorization with increasing Mn/O ratio.

This morphology categorization approach based on MF values enables unprecedented categorization of different existing non-metallic inclusion shapes in cross-section samples. By considering irregularity, angularity, and elongation, effects like clustering or product deformation can be verified, evaluated, and quantified. Combining chemical analysis of automated SEM/EDS analysis with precise morphological classification enables precise knowledge about inclusion evolution over different process steps.

4.9 Evaluation of Inclusions' Spatial Distribution

Non-metallic inclusion strings and clusters in the meso size range ($> 15 \mu\text{m}$) are easy to identify and differentiate according to image analysis and EN10247 standard. Categorization of nearest-neighbor characteristics is related to absolute distances and shapes of particles. Absolute $40 \mu\text{m}$ and $20 \mu\text{m}$ thresholds cannot be applied to long-range order differentiation for micro and sub-micro inclusions, and a general optical evaluation is not suitable. Datasets of automated inclusion analysis can provide a basis for evaluations by detected position and morphological data for every single inclusion in the defined size range and area. Therefore, this work's additional achievement is a formulated data treatment approach categorizing non-metallic inclusion by their nearest-neighbor relations and considering the inclusions' effective size. Dealing with data output of automated measurements, some effects need to be considered: On the one hand, using particles center-point-distances (CPD) possibly causes

misidentification of inclusions nearest-neighbors. As illustrated in Figure 55, different nearest-neighbor relations can result by quantifying CPD and edge-to-edge distances (EED). The apparent nearest-neighbor for inclusion A is inclusion C, considering inclusions size and morphology. As soon as non-metallic inclusions increase in elongation, edge-to-edge distance reveals the more correct correlation. On the other hand, if inclusion evaluations are performed based on simple image-related analysis, the chemical information is left out. Artifacts with a dark appearance are also identified as neighboring inclusions.

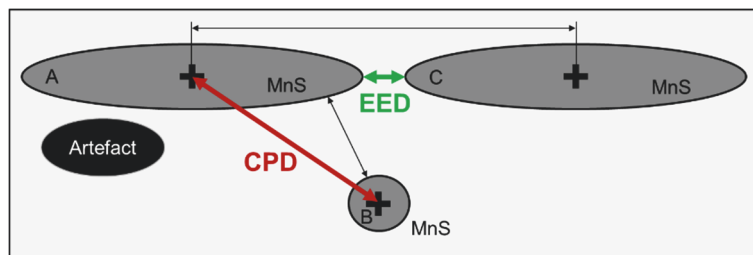


Figure 55: Center point distance and edge-to-edge distance.

According to Figure 55, an excellent nearest-neighbor correlation should consider particle sizes, morphology, orientation, edge-to-edge distances, and compositions. Further on, cluster and string identification should be performed based on size relative values to enable universal categorization for sub-micro, micro, and meso inclusions in different products.

In the first step, a calculation procedure for improved distance determination is defined. According to possible misinterpretations using center-point-distance relations, a methodology is formulated to approximate edge-to-edge distances between inclusions based on automated analysis data. To extend a particle evaluation tool described in Section 4.10, an additional Matlab routine was programmed [164]. To calculate the euclidian distances between every single particle and the remaining bulk, x/y-positions of every non-metallic inclusion are used. The closest 9 neighbors of every particle are identified and correlated. Based on the inclusions detected position, orientation, length, and width, an 8-point ellipsoid approximates the inclusion's shape. Figure 56 schematically displays the morphology approximation of inclusion A and B. 8-points-ellipsoids are a good approximation of spherical and elongated inclusions considering important outmost positions. Like the center point distance calculation for every A1-8 position, all euclidian distances to B1-8 positions are calculated. The smallest distance, A8/B3 in the present case, defines the edge-to-edge distance of inclusion A and B. Differences to the actual EED distance are negligible.

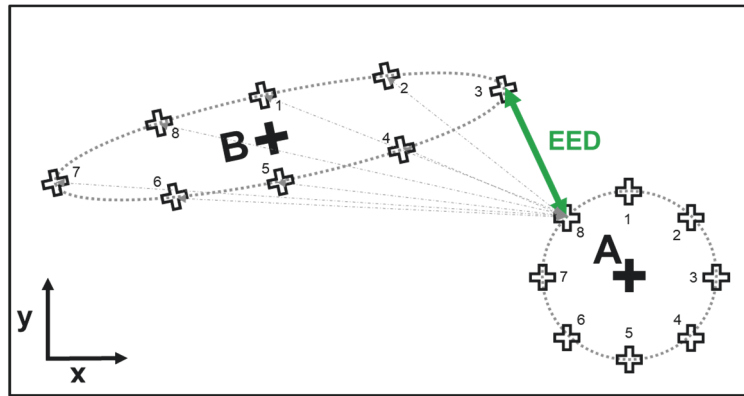


Figure 56: Illustration of edge-to-edge approximation.

Performing cluster and string identification, nearest-neighbor correlations are determined. Then, the ratio of the actual edge-to-edge distance and the appearing equivalent circle diameter (ECD) is calculated according to Equation 21. To create a relative distance parameter (d^Λ) for every particle. For every particle, a relative distance parameter is determined.

$$d^\Lambda = \frac{d^{ee}}{ECD} \quad (21)$$

Parameter d^Λ is further used for the evaluation of particle relations. A maximum distance of 150 % of the particle's diameter (ECD) is chosen as the inclusion correlation limit. Figure 57 illustrates the three possible states of the nearest-neighbor relation. In the first case, both inclusions are nearest-neighbors but not within the 150 % ECD range. In case two, both are within the range, and in the third case, only for the larger inclusion the limit of the correlation criterion is fulfilled.

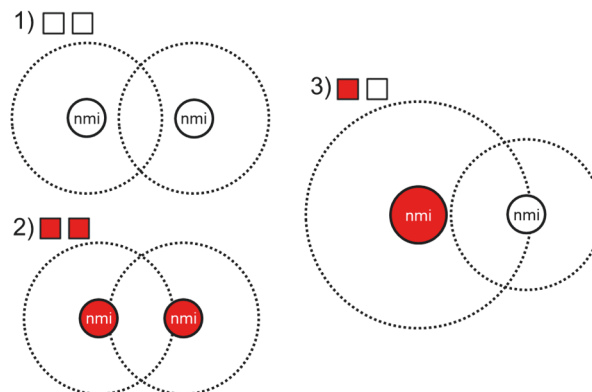


Figure 57: Possible nearest-neighbor relations.

For every particle, the correlation to its nearest-neighbor can therefore easily be illustrated and evaluated. In Figure 58, for an exemplarily measured S235JR, the result of a d^Λ -calculation is displayed, and all nearest-neighbor relations closer than 150 % ECD are marked by red

positions. The presence of large elongated sulfide inclusions in this steel grade enables a good demonstration of the formulated correlation. Inclusion strings and clusters can easily be identified after automated analysis by the applied 150 % categorization. In Figure 58, cross-section images of areas with a high number of correlated non-metallic inclusions are displayed. The results providing an impartial validation of the nearest-neighbor relations are in good accordance with the binary NMI diagram, obviously showing inclusion strings in the marked areas.

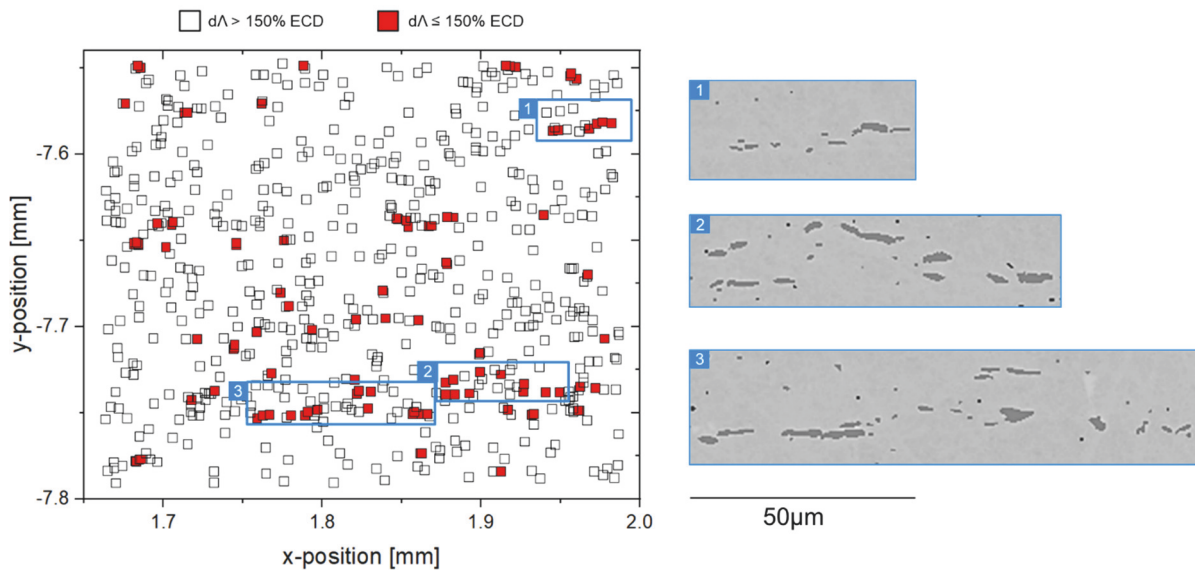


Figure 58: Relative distance relation based on particle size.

The nearest-neighbor evaluation can be applied to any samples for cleanliness evaluations. All size regimes from macro to sub-micro particles can be evaluated by a size-related distance correlation. With the described method, especially research in oxide metallurgy, particle formation and segregation can be massively improved. Now it is possible to evaluate rolled and as-cast samples with the same methodology, enhancing comparability and reproducibility of inclusion analytics and modern metallurgy.

4.10 Implementation of gained knowledge by FET development and improvements

Due to the great variety of metallurgical tasks and projects at the Chair of Ferrous Metallurgy, different inclusion analytics' challenges are daily business for SEM operators. Most assignments require a modified interpretation based on manual and automated particle analysis by means of SEM/EDS. Data post-processing and interpretation of automated measurements revealed themselves as a significant step in metallurgical research dealing with

inclusions. The current work's task is to define objective processing procedures providing a good foundation for subsequent interpretations, dealing with steel samples' measurement phenomena eliminating misinterpretations. Especially for future research demands at micro and sub-micro inclusions, a significant step towards improved analysis and interpretation has been done. The formulated data treatment approach was implemented into a stand-alone "Feature Evaluation Tool" (F.E.T.) coded in Matlab dealing with

- artifact correction,
- classification depending on the non-metallic phase,
- typification based on metallic binding partners without rating and
- interpretation and representation strategies.

The operator monitors all processing steps, and not a single piece of information is deleted. Consistency and objective inclusion evaluation is ensured by most neutral categorization dealing with sub-micro and micro steel cleanliness evaluations of steels. The following section outlines an ULC steel evaluation by the F.E.T. dealing with a broad inclusion population (0.05 %C, 0.07 %Si, 0.06 %Mn, 30 ppmS, 53 ppmN). The steel sample was measured according to the parameters mentioned in Section 2.1.

4.10.1 Correction of Artefacts

Referring to the current microscope and detector system, automated analysis data is exported into an excel sheet. A "raw data" file is created in a first step, and micro cleanliness evaluation is defined by excluding all inclusions larger than 15 µm ECD (equivalent circle diameter). Further, measurement artifact correction is applied by composition criteria listed in Table 13, dealing with falsely detected porosities and scratches (matrix) and grinding (SiC) and polishing residues. Finally, insufficient measurements (O=N=S=0) are excluded, followed by a normalization step. The correction procedure can be applied to non-metallic inclusion populations in low, medium, and high alloyed steels.

Table 13: Data post-processing: correction criteria low, med, and high alloyed steels.

Artifact type	Criterion
Matrix	$Fe + Mn + C + Cr + Ni + Mo + Nb + Ti + V > 99.99.$
Grinding residues	$Fe + Mn + C + Cr + Ni + Mo + Nb + Ti + V + Si > 99.99.$
Polishing residues	$Fe + Mn + C + Cr + Ni + Mo + Nb + Ti + V + Si + Alkali > 99.99,$ Alkali = Ar, Cl, F, Na, K, Cs, P.
Insufficient measurement	$O + N + S = 0.$

To identify non-metallic inclusions in carbide steels with low Si contents, a possible approach is formulated and listed in Appendix A.1 (Table 18) to differentiate between matrix, carbide, artifact, and NMI data. Due to the high chemical and morphological complexity of non-metallic carbide phases, an adaption of correction procedure and additional manual evaluation is recommended for other carbide containing steels. All identified artifacts and neglected features are stored in a “rejected.xls” file for additional evaluations of sample porosity or quality of specimen preparation. All remaining non-metallic inclusions (NMI) are transferred to the “CorrData.xls” file for subsequent cleanliness evaluations dealing with chemical composition, size, morphology, and spatial distribution. Single neglected data groups (e.g., inclusions > 15 µm) can again be reinserted to the NMI list if the research task demands.

4.10.2 Classification Depending on Non-Metallic Partner

General inclusion classification is performed based on a 0.1 wt-% limit, considering the current EDS systems’ reasonable identification limit for trace elements at non-standard EDS analysis. According to the following categorization guideline, seven main inclusion classes are differentiated. Inclusions’ non-metallic bonding partners define Single-phase (O, S, N) and multi-phase inclusion classes (OS, ON, NS, ONS). Identification of homogeneity or heterogeneity only based on EDS data is not recommended, and defining inclusions generally as “Oxysulphides” for OS particles would indicate a homogenous compound. Caused by different production steps, most multi-element inclusions in steel generally appear heterogeneous. Therefore the nomenclature listed in Table 14 is recommended.

Table 14: General inclusion classification criteria.

Classification	Oxygen[%]	Sulfur [%]	Nitrogen [%]
Oxide (O)	> 0.1	≤ 0.1	≤ 0.1
Sulfide (S)	≤ 0.1	> 0.1	≤ 0.1
Nitride (N)	≤ 0.1	≤ 0.1	> 0.1
Oxide-Sulfide (OS)	> 0.1	> 0.1	≤ 0.1
Oxide-Nitride (ON)	> 0.1	≤ 0.1	> 0.1
Nitride-Sulfide (NS)	≤ 0.1	> 0.1	> 0.1
Oxide-Sulfide-Nitride (ONS)	> 0.1	> 0.1	> 0.1

Correct and objective data representation is done to perform extensive inclusion evaluation as listed in Table 15. For a first overview, the mean equivalent circle diameter (ECD) and normalized inclusion number and area are discussed. Significant differences in particle sizes and dominant particle classes are easily identified and interpreted onto their influence on material properties.

Table 15: Result of automated inclusion analysis.

Summary of typified NMs	ECD	Number		Area	
	[μm]	[nr./mm ²]	[%]	[$\mu\text{m}^2/\text{mm}^2$]	[%]
Oxides	1.7	10	11	32	9
Sulfides	1.7	14	14	37	11
Oxide + Sulfide	1.9	19	21	77	23
Nitrides	2.2	25	26	108	31
Oxide + Nitride	1.7	7	7	19	5
Nitride + Sulfide	2.1	10	11	44	13
Oxide + Nitride + Sulfide	1.7	10	11	26	8
TOTAL	1.9	95		343	

The F.E.T. enables a straightforward depiction of general steel cleanliness parameters displayed in Figure 59. The low inclusion number and area confirm a high steel cleanliness and appropriate process control.

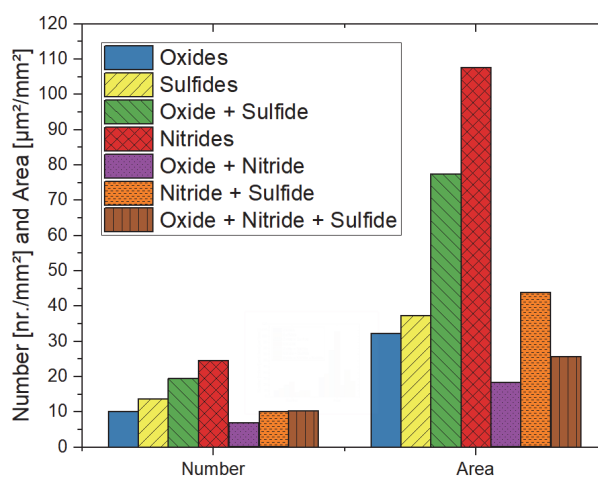


Figure 59: General classification of LC sample.

In the present case, the dominant inclusion classes are nitrides followed by oxide-sulfide inclusions. To evaluate the origin of detected particles, the next logical step is particle typification.

4.10.3 Typification for Metallurgical Steel Cleanness Evaluations

To identify specific non-metallic inclusions more precisely, typification is performed by considering the metallic bonding partners of a non-metallic phase. According to various steel treatments and alloying concepts, an exceptionally high number of different inclusions can occur. Performing particle typification using the Feature Evaluation Tool, 577 different inclusion types are considered based on the following element combinations:

- Mg, Al, Si, Ca, Ti, Mn, Cr – O
- Mn, Mg, Ca, Ti, Al* – S
- Ti, B, Al, V, Nb, Si – N
- Mg, Al, Si, Ca, Ti, Mn, Cr – OS
- Mg, Al, Si Ca, Ti, Cr – ON
- Mg, Al, Ca, Ti, Mn – OS
- Mg, Al, Si, Ca, Ti, Mn, Cr – ONS

All inclusions are objectively typified by their chemical binding partners, e.g. “(Al,Mg,Ti)OS”, avoiding any assumptions of spinel formations or other non-metallic states. To identify Al-oxide nucleation sights in sulfidic particles, Al* is considered a metallic binding partner in sulfide typification. Attention must be paid to pure Si-oxide inclusions, which can also be grinding residues with falsely detected oxygen. High alloyed steels may need higher identification thresholds for Cr or Mn typification due to observed fluctuation in EDS concentrations. Pure CaO inclusions can also be caused by sample cleaning (dust remover). If particles with uncertain origin (SiC, CaO, or CrO) have a large share of the overall inclusion population, manual verification should be considered.

For the present ULC steel, matrix composition is also evaluated using SEM/EDS. All matrix element concentrations in the range of 0.05 - 0.07 %, typification limits are set to 0.1 %. Therefore, an element is identified as a component of the inclusion, if the element concentration exceeds matrix composition. According to Table 16, different types are present in single and multi-phase inclusion classes.

Table 16: Typification of non-metallic inclusions.

Categorization	Most frequent typification
Oxides	(Si)O, (Al,Ti)O, (Al,Si,Ca)O
Sulfides	(Mn,Ti)S, (TiS), (Mn,Ti,Al*)S
Oxide + Sulfide	(Ti)OS, (Al,Ti)OS, (Al,Ti,Mn)OS
Nitrides	(Ti)N, (Ti,Al)N
Oxide + Nitride	(Ti+)ON, (Al,Ti+)ON, (Si,Ti+)ON
Nitride + Sulfide	(Ti+)NS, (Al,Ti+)NS, (Al,Ti+,Mn)NS
Oxide + Nitride + Sulfide	(Al,Ti+)ONS, (Ti+,Mn)ONS, (Al,Ti+,Mn)ONS
TOTAL	(Ti)N, (Ti,Al)N, (Ti+)NS, (Al,Ti,Mn)OS

The three most frequent particles are listed, verifying aluminum and titanium as the most dominant bonding partners. The present inclusion population can be correlated to aluminum deoxidation and titanium stabilization.

4.10.4 Data Representation and Interpretation

If melt conditions during production shall be evaluated, especially the oxidic steel cleanness is relevant. According to Figure 60, all inclusions with an oxidic basis are particularly correlated to an existence in the liquid state. The summed inclusion number per area on an oxide basis can be correlated to the liquid state's steel cleanness. 47 particles/mm² signify good process control and reduced atmospheric contact during production.

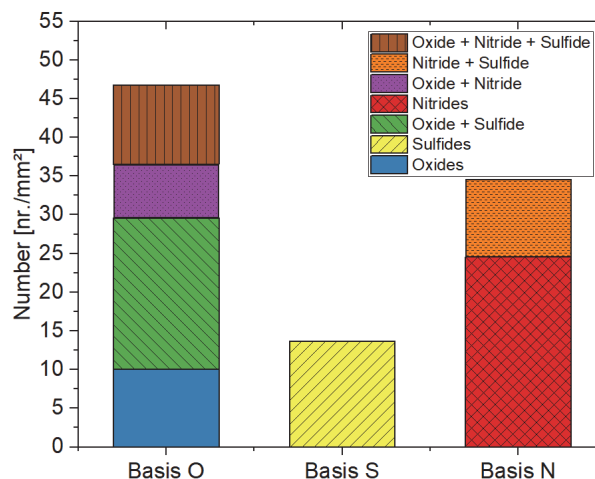


Figure 60: Reinterpretation of inclusion population according to non-metallic bonding partners.

According to manual evaluations with element concentration mappings shown in Figure 62, particle heterogeneity is caused by typical nucleation effects. Often, after automated

measurements, extensive manual evaluations need to be performed to determine further inclusions' characteristics.

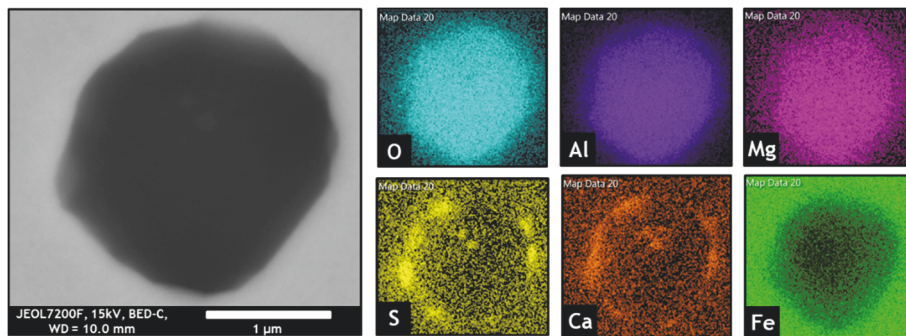


Figure 61: Element mapping of heterogeneous oxide-sulfide inclusion.

The F.E.T. also provides tools for more precise differentiation of multi-phase inclusions, according to Figure 62. Quantifying the relative shares of non-metallic phases with thresholds of 25 %, 50 %, or 75 %, multiphase particle populations' general characteristics can be deduced.

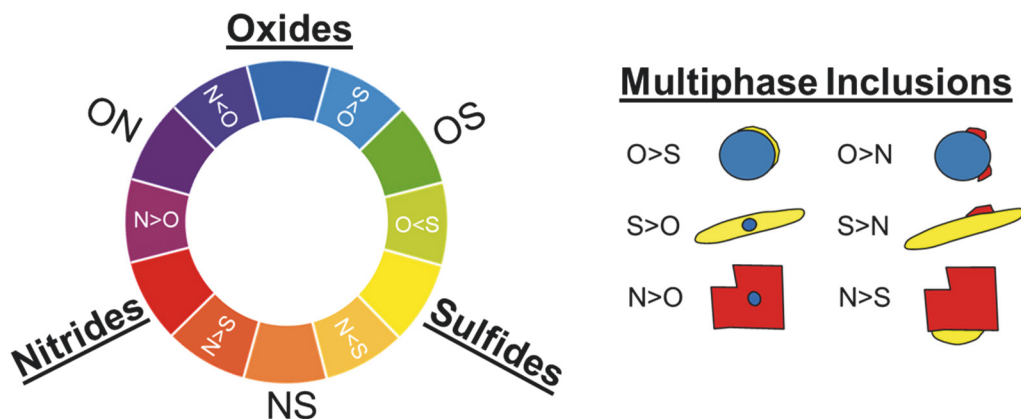


Figure 62: Improved inclusion classification for further categorization.

O>S and O>N inclusions are identified as mainly oxide NMIs with nitride or sulfide nucleation sights. In contrast, S>O and S>N particles are generally sulfide inclusions with minor oxide and nitride components depending on the formation mechanism, similar to N>O and N>S particles displayed in Figure 62. Morphological differentiation of complex O>NS, S>ON, and N>OS is difficult, and a general categorization can't be determined by composition data. With

higher complexity, additional manual verifications of particle heterogeneity, including high-resolution images and concentration mappings, are essential.

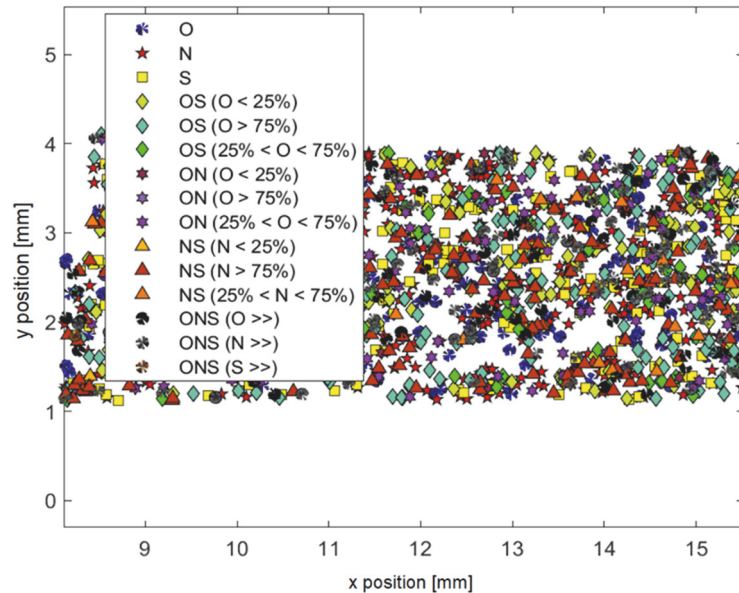


Figure 63: XY-distribution of different classification categories.

Additionally, the program illustrates particle categories considering the leading non-metallic partner of multiphase inclusions and their spatial distribution to determine clustering effects of specific particle classes. In Figure 63, no explicit grouping of inclusion categories can be found. Strong segregation effects can result in an appearing sulfidic or nitride network depicting the primary dendritic structure. Described steel cleanliness evaluation can be performed for a large variety of different steel grades.

5 Implementation of Improved Steel Cleanness Evaluations for Industry Demands

Demonstrating the application of enhanced steel cleanliness evaluations of automated SEM/EDS analysis, five industry inclusion populations of industry samples are discussed. The effect of general steel composition, cooling conditions, and different production concepts on particles' characteristics is evaluated using F.E.T. and mathematical iron correction. Table 17 gives a short overview of the general characteristics of the used samples. Three different steel grades, including ULC, LC micro-alloyed, and a high alloyed CrNi-austenite, are evaluated in this section.

Performed evaluations can be used to improve production, product developments, quality control, or fundamental research. With more data stored and published, new quality standards for different steel grades can be formulated based on described steel cleanliness characteristics. Applying mathematical matrix correction to single inclusion types, the quantifiable output increases for micro and sub-micro inclusions also enabling improved verification theories on particle formation.

Table 17: Industry steel samples for improved particle analysis.

Sample	Composition Wt%	Sample History	Manually evaluated NMI-characteristics
VIM	C: 0.01%, Si: 0.25%, Mn: 0.96%, P: 0.02%, S: 0.02%, Cr:0.93%.	Ingot casting, not remelted	MnS; micro range; spherical
LC-A	C: 0.06%, Si: 0.012%, Mn: 0.17%, P: 0.02%,	Ladle lollipop sample	(Al,Mg,Ca)OS; micro range; spherical
LC-B	S: 0.007%, Al: 0.04%.	Rolled bloom sample	(Al,Mg,Ca)ONS; micro range; angular and irregular
CrNi-A	C: 0.08%, Si: 0.8%, Mn: 1.9%, P: 0.03%,	Ingot casting producer A	TiN; micro and meso range; single inclusions
CrNi-B	Ti: 0.4% S: 0.02%, Cr: 17.4%, Ni: 9.5%.	Ingot casting producer B	TiN and TiS; micro and meso range; clustered areas

5.1 Chemical Classification and Typification Beyond Standards

The first steps of steel cleanliness evaluations should basically contain a general overview on existing classes and types of non-metallic particles in the analyzed sample. By their general non-metallic composition and combination of metallic partners, inclusions' origin can be conducted. Different steel grades result in varied non-metallic inclusion populations and particle densities according to varied input materials and production routes. The three exemplarily evaluated steel samples generally show comparably low particle numbers (54-170/mm²) and corresponding areas according to their sample history. Figure 64 displays the relative shares of inclusion classes within one sample demonstrating essential differences in the steels' inclusion classes. For classification, 0.1 % thresholds are used. For an element to be identified as a component of the inclusion, the inclusion's concentration must exceed matrix composition.

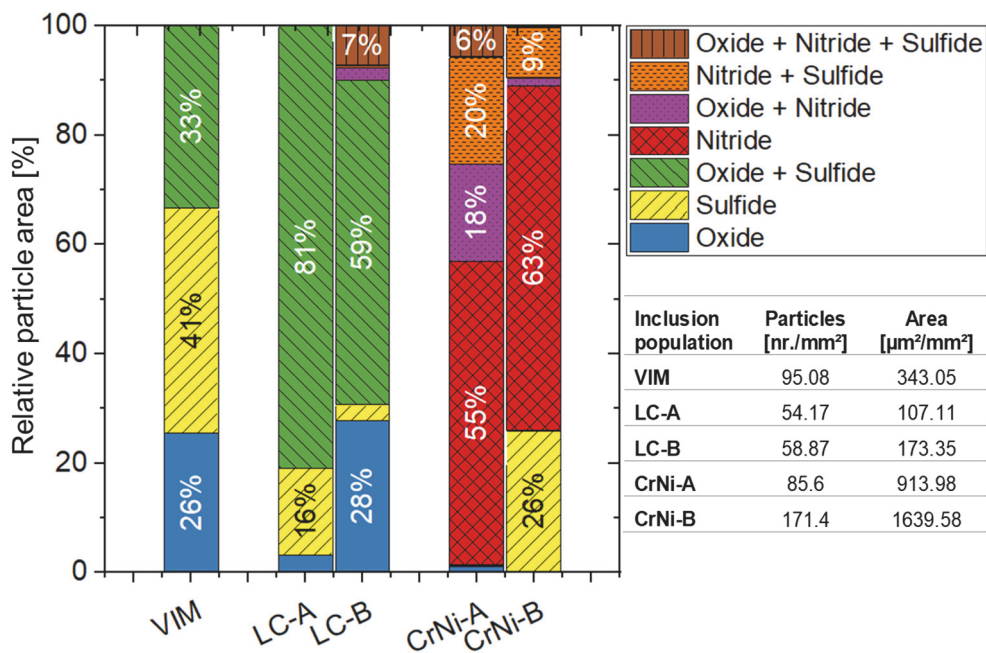


Figure 64: NMI population in different analysed steel samples.

Generally, vacuum induction melting (VIM) is used to produce steels with the highest purity restrictions, including the lowest numbers of oxide inclusions. According to the melting and casting procedure without atmosphere contact at any time, oxygen and nitrogen pickup are kept to a minimum at VIM samples. Good process control can be conducted by the resulting low absolute amount of oxide and any nitride formation with absolute numbers of 95 particles/mm² and 343 μm² inclusion area/mm². The existing non-metallic inclusion population is predominantly sulfidic with small remaining deoxidation products, caused by the lack of practicable slag metallurgy. The share of oxide inclusions at multiphase particles is low. The main inclusion types detected are (Mn)S, (Al,Si)OS, (Ca)OS, (Al,Mn)OS, (Si)O, (Al,Si)O, and (Al,Si,Ca)O. Based on the general steel cleanliness evaluation considering inclusion numbers, areas, and classes, no major indicators for improvements can be found. Increased purging can possibly enhance oxide particle separation and reduce the overall number and area of existing inclusions. By an subsequent remelting step after VIM production, the evaluated sample can reach the highest steel cleanliness with most sulfide inclusions removed.

In contrast, the evaluated micro-alloyed LC steels show a more complex NMI population. In the present case, the same melts' inclusion characteristics are determined by differing sampling methods. Caused by different cooling conditions, the same steel results in obviously differing inclusion classes. LC-A represents lollipop sampling taken before continuous casting, and LC-B is cut out of a cast and rolled bloom later in production. LC-A, undergoing fast cooling, results in about 54 inclusions/mm² with 107 μm²/mm² area, mainly oxide and oxide-

sulfide inclusions. Due to the larger product size and reduced heat transfer, LC-B creates different O-N-S particle variations. Particle numbers of 58 /mm² remain unaffected, but inclusion sizes increased to 170 $\mu\text{m}^2/\text{mm}^2$. Additionally, comparing LC-A and LC-B inclusion populations, an increase of pure oxide inclusions indicates slight oxygen pickup. Slower cooling conditions enable the formation of more complex nitride and sulfide inclusions. After F.E.T. typification, the samples' main types are (Al,Ca)OS, (Al)O, (Ca)O, (Al,Ca)O, and (Al,Ca,Mg)O inclusions for LC-A and (Al)O, (Al,Mg,Ca)O, (Al,Mg,Ca)OS, (Al,Mg,Ca,Ti)OS and (Mg,Al,Ca,Ti)ONS for LC-B. Evaluating the change in inclusions composition, an increased presence of Mg is detected. After CaS correction of multiphase inclusions, the particles' change in composition is determined by the ternary system illustrated in Figure 65. According to the following diagram, an apparent Mg pickup possibly caused by refractory dissolution can lead to a higher potential of crucial spinel-formation in the product. Mg pickup in inclusions combined with increased numbers of pure oxide inclusions affirms the refractory dissolution theory, supplying the melt with oxygen for new particle formation and magnesium for inclusion modification.

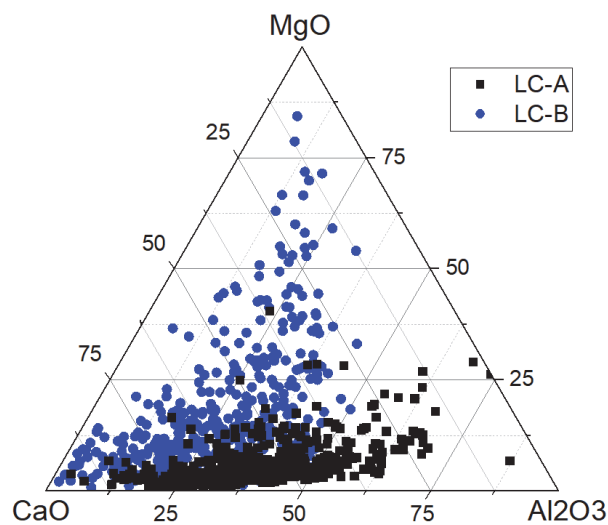


Figure 65: Ternary system of Al, Mg, and Ca containing inclusions.

A considerate sampling according to the research or quality evaluation task should be kept in mind. If products are compared, sampling must unavoidably be taken at the latest possible position. Otherwise, data interpretation is limited and influenced by changed cooling. As illustrated in the current case, the same steel results in significantly different non-metallic inclusion populations.

CrNi-A and CrNi-B samples represent high alloyed steels for turbine shafts and energy production. Due to the increased demand for large products for energy machines, steel producers try to improve their production. The present case contrasts two different suppliers

of the same steel grade and dimension. In difference to A, producer B has to deal with later complaints caused by material inhomogeneities revealing after machining the ingots. These steels have a high potential of nitride formation due to complex alloying concepts, including high nitrogen contents supporting the steels' high thermal stability and toughness. Present samples with 85 and 171 particles/mm² and areas of 913 and 1639 μm²/mm² predominantly nitrides indicate a difference in particle size, as illustrated in Figure 64. By the high tendency of nitrides to agglomerate, these steels are difficult to produce by large ingot casting. According to the applied F.E.T. analysis, CrNi-A and CrNi-B share a similar general inclusion classification. Sample A predominantly contains TiN, (Ti,Al)ON, (Mg,Ca,Ti)ON, (Mg,Ti)NS and (Al,Mg,Ca,Ti)ONS inclusions. In sample CrNi-B inclusions are similar, mainly nitride types but a general higher amount of sulfidic inclusions are present: (Ti)N, (Ti)S, (Ti)NS, (Mg,Ti)NS, (Al,Ti)ON, and (Al,Mg,Ti)NS. According to the increased formation of sulfide-containing inclusions in CrNi-B, differing cooling conditions at particle formation or the application of more sulfide-containing alloying materials can be assumed. Sulfide inclusions are generally not known to cause problems during or after machining. Therefore, more attention has been paid to oxide and nitride morphology of multiphase inclusions by manual evaluation. To determine the inclusions' element location within ON-particles, manual concentration mappings illustrated in Figure 66 are performed, showing common Al₂O₃-TiN multiphase inclusion.

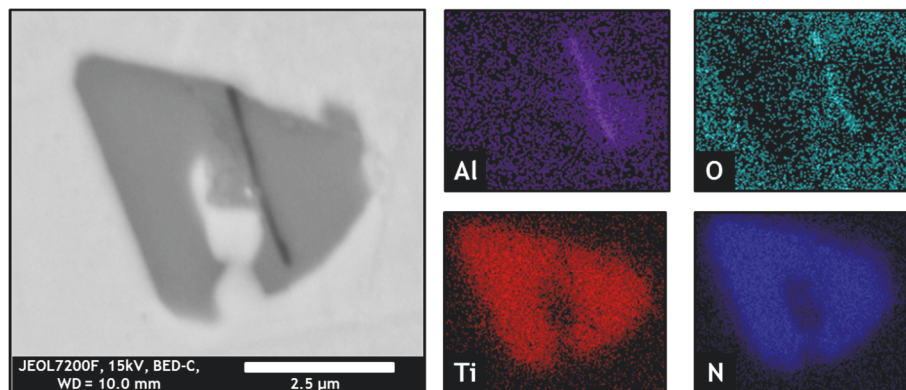


Figure 66: Element concentration mapping of a (Ti,Al)ON inclusion.

Following the methodology of Section 4.5.1, electrolytic extraction is applied at both samples to evaluate differences in particles' morphology and element distribution. According to Figure 67, appearance and element concentration mappings are similar. Chemical classification and typification did not reveal distinctive differences, including manual evaluations.

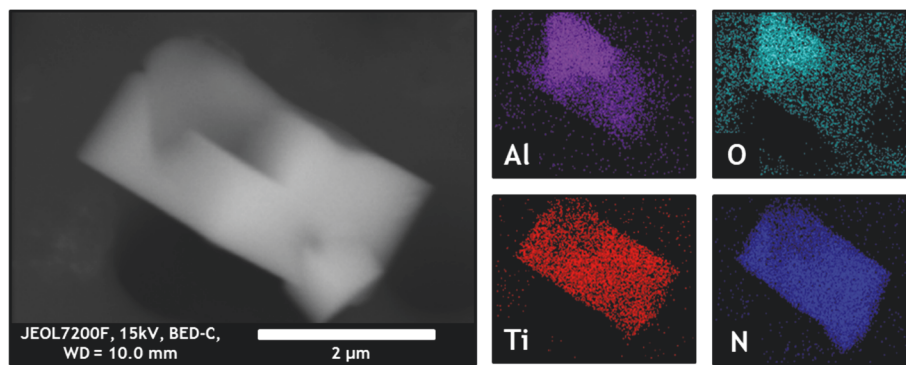


Figure 67: Element concentration mapping of an extracted (Ti,Al)ON inclusion.

5.2 Morphological Categorization

Applying the formulated MF categorization to industry samples, a good overview of particles' forms and morphological characteristics can be given. VIM samples and samples taken after ingot casting result in general spherical morphology of all inclusions. In contrast to that, LC-A and LC-B samples are evaluated using F.E.T. to determine the corresponding MF values for every particle. Then, categorization is applied based on developed classes and types of Section 4.8. Figure 68 displays the relative share of each morphological inclusion type in one sample. Generally, circular O and OS inclusions (82 %) are formed in LC-A samples according to high cooling speeds inhibiting the formation of large sulfide and nitride inclusions. LC-B, in contrast, shows an increased presence of angular and irregular appearing particles in cross-section analysis correlation. Different sampling results significantly varied morphological inclusion parameters due to the increased amount of multiphase sulfide and nitride inclusions.

Also, the applied rolling procedure to LC-B can be identified by an increase of elongated morphology types.

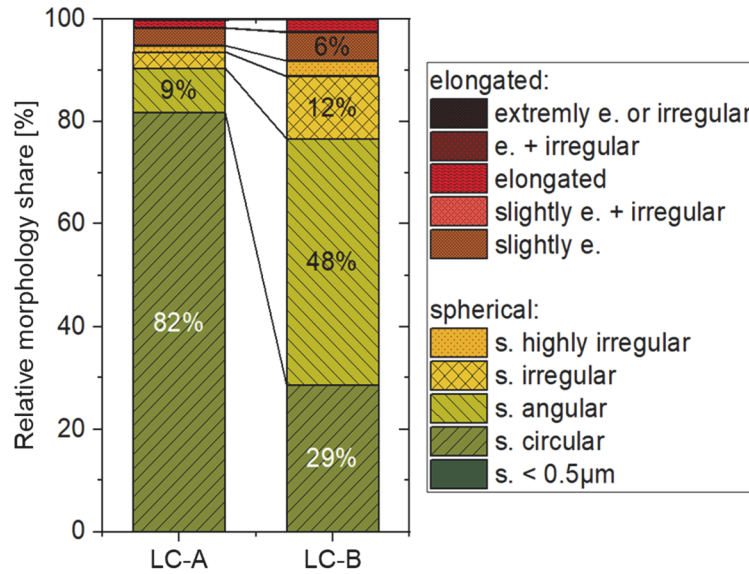


Figure 68: Morphology evaluation LC-A and LC-B samples.

Evaluating the morphological characteristics of high alloyed CrNi-steels, a relatively high amount of angular categories is detected correlating to mainly nitride inclusions in these samples. Comparing CrNi-A and CrNi-B, an increased share of elongation and irregular inclusion types are detected in sample B.

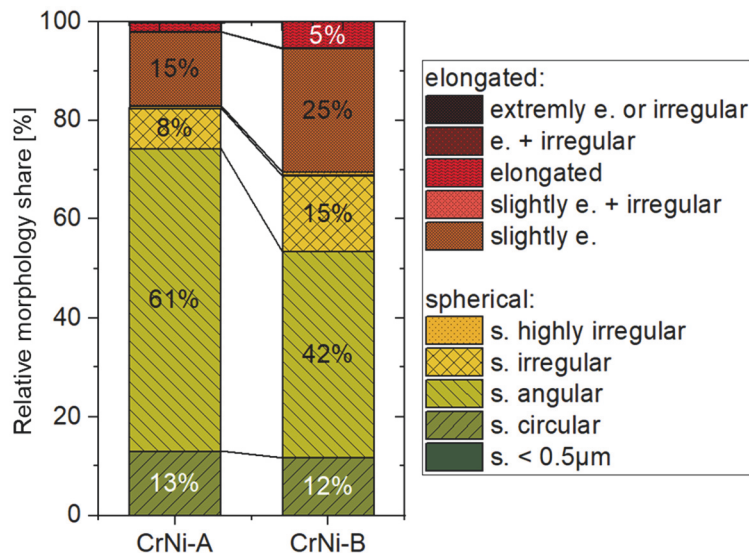


Figure 69: Morphology evaluation CrNi-A and CrNi-B samples.

Different morphological characteristics affirm the assumption of differential production concepts of the same steel. Although nitrides are hardly deformable and manual evaluation

did not result in morphological changes, an increased general elongation is detected in all types. Possibly this discrepancy can be correlated to inclusion strings or clusters formed in the liquid state.

5.3 Quantified Spatial NMI Distribution

Due to inconspicuous morphological appearance and good controlled solidification after VIM production, inclusions can be seen as generally randomly distributed. For evaluating general spatial particle distribution, inclusions position's and nearest-neighbor relations of LC and CrNi samples are discussed dealing with segregation and clustering. According to Section 4.9, the nearest-neighbor edge-to-edge distances are calculated and illustrated. Figure 70 displays the frequency of distances calculated in samples LC-A and LC-B. For comparison, the relative quantity of distances per area is discussed.

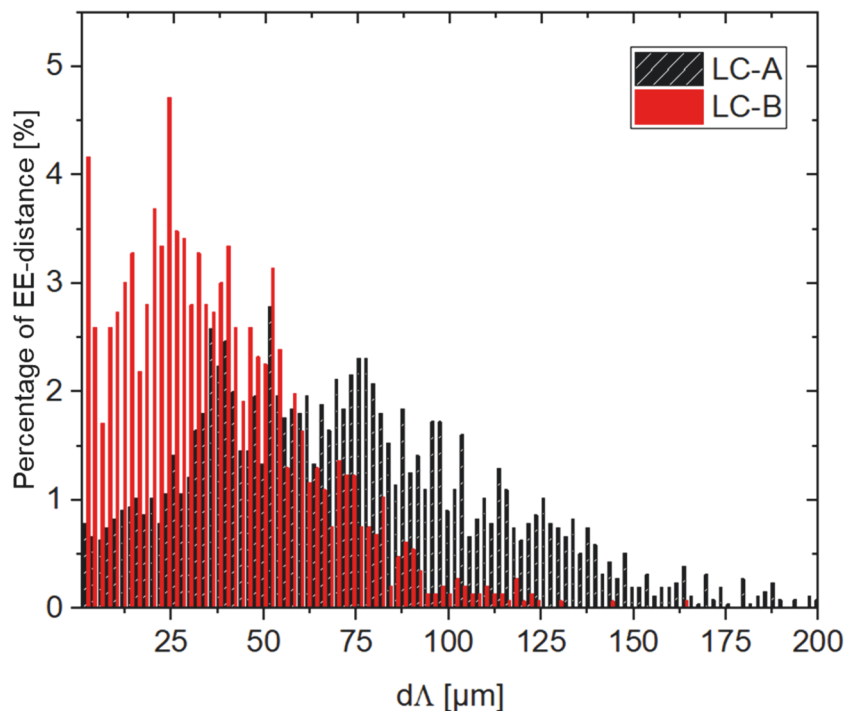


Figure 70: Nearest-neighbor (NN) distribution of LC-A and LC-B samples.

LC-A distances show a diversified distribution with similar amounts of detected lengths in the range of 0.2 – 200 μm . Interpreted as randomly distributed particles, LC-A affirms unaffection by any segregation phenomena during solidification. A higher amount of small distances is detected at sample LC-B, indicating regions with higher and lower particle densities. The main difference can be noted at distances below 40 μm . Caused by a generally slower cooling,

oriented solidification, and therefore more time for particles' formation, increased agglomeration in the bloom center can be conducted. Both particle populations appear randomly distributed to the operator due to small inclusions having relatively large distances between them. Nevertheless, a difference can be quantified by the F.E.T. affirming the sensitive quantification of morphological parameters and spatial distributions.

The same tendency but more distinctive difference in particle distance distribution can be seen in CrNi samples. Sample A shows a broad distance distribution, whereas particles in CrNi-B about 35 % of all inclusions are closer than 5 μm to their nearest-neighbor. This relatively high number of small distances indicates increased agglomeration of nitrides during ingot casting.

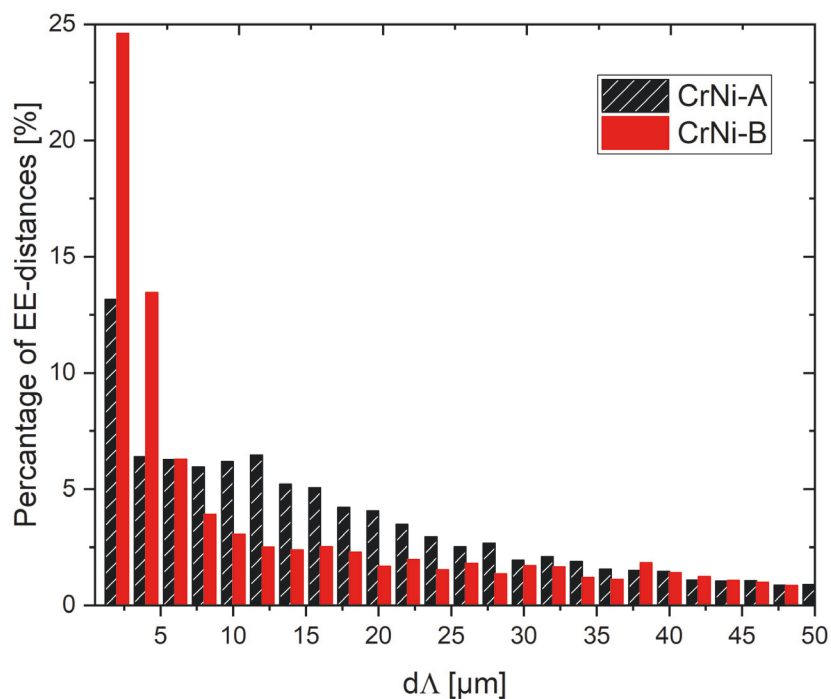


Figure 71: Nearest-neighbor (NN) distribution of CrNi-A and CrNi-B samples.

CrNi-A and CrNi-B are evaluated using the formulated 150 % ECD threshold for cluster identification according to Section 4.9. Particles having their nearest-neighbor within the criterion considering edge-to-edge distances can easily be correlated and identified. Figure 72, illustrating samples A and B, displays the difference in spatial particle distribution. Sample CrNi-A shows a generally randomly distributed inclusion population compared to massive clustering in CrNi-B.

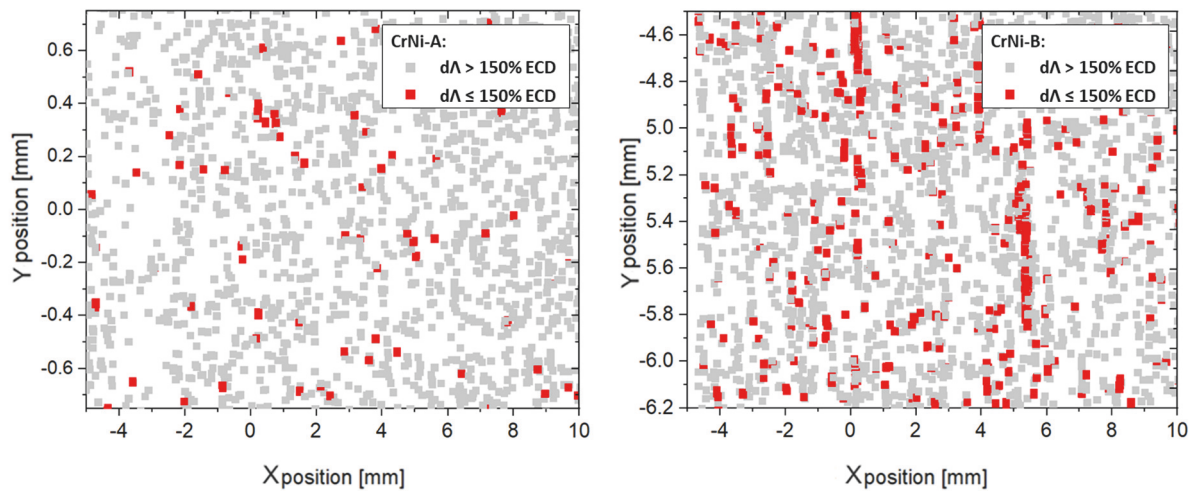


Figure 72: Evaluation of clustering by 150 % ECD threshold for nearest-neighbor distances.

Quantification of spatial distribution, including relative distance parameters, distance distributions, and the actual nearest-neighbor information, demonstrates noticeable differences in sample production. If the number of clusters can be reduced by improved production, the probability of customer complaints can be reduced to a minimum. Applying this evaluation procedure to any automated measurement performed in future clustering phenomena can be identified, quantified objectively, and categorized unaffected by absolute particle sizes.

5.4 Iron Correction at Industry Samples

Improved composition evaluation enables fundamental research and considerations. Therefore applying the mathematical matrix correction procedure described in Section 4.7, compositions of spherical single-phase inclusions are post-processed based on the mean interaction split approximated by Boltzmann-fit (Figure 23, Equation 15). To cover industry and research demands, inclusions larger than $1 \mu\text{m}$ are treated. For example, VIM sample's single-phase and randomly distributed MnS particles are displayed in Figure 73. The box whisker diagrams illustrate the initially detected EDS composition (blank box) and values after Fe-correction (filled box) of the detected MnS inclusions. By correcting detected $\text{Fe}^{\text{matrix}}$, S, and Mn compositions increase. A mean Fe value of approximately 29 % is reasonable considering sulfide formation during solidification undergoing Fe segregation similar to (Fe,Mn)oxide development in Section 4.6.1. Considering solute or bonded Fe, the more accurate typification is (Fe,Mn)S in this sample.

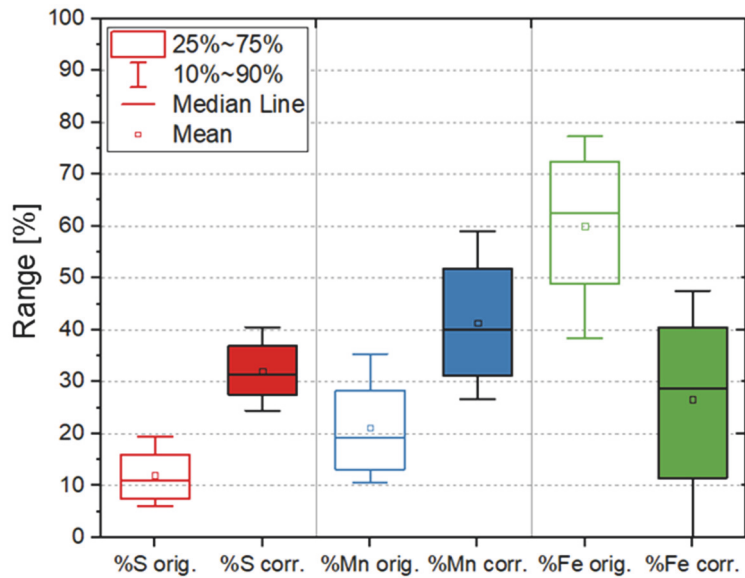


Figure 73: Composition Range (Fe, Mn)S inclusions.

To evaluate the iron content of non-metallic inclusions with a different particle formation history, correction is applied to primary, randomly distributed, single-phase TiN inclusions of CrNi-A sample. Due to enforced development in the melt by 0.4 % Ti, lowest Fe contents in particles are assumed. Before matrix correction, approximately 20 % Fe is detected in inclusions illustrated in Figure 74.

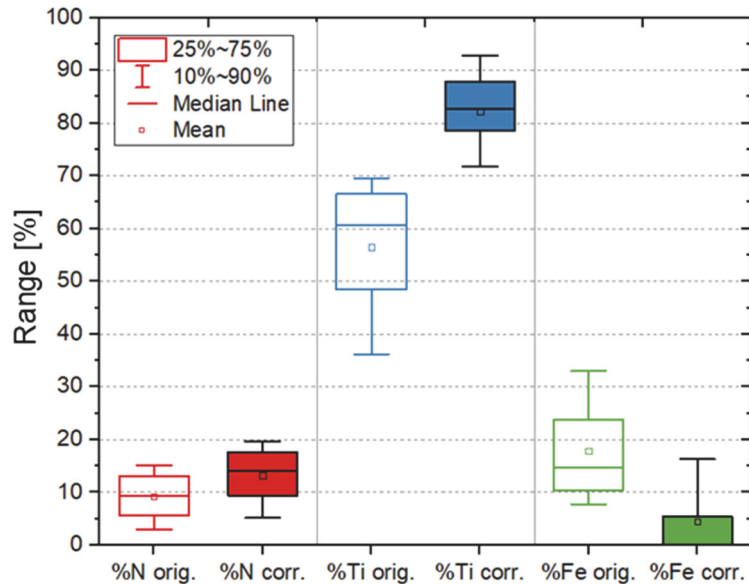


Figure 74: Composition range TiN inclusions.

After interaction bulb correction, box whisker plots are narrowed, and a mean composition of 13 %N, 82 %Ti, and 5% Fe can be noted. Composition determined after electrolytic extraction

of pure TiN inclusions resulted in 72 %Ti, 27 %N, and 1 %Fe. Mathematical matrix correction obviously improves the EDS result, leading to a more comprehensible and representative overall inclusion composition. According to Section 4.7, the formulated consideration of matrix effects can be applied to any typical homogenous non-metallic inclusion phase in steels. If matrix element concentrations in sub-micro particles shall be evaluated, a combination of electrolytic extraction and automated inclusion with subsequent matrix correction is recommended. Comprehensive and statistically reliable composition ranges of non-metallic inclusions combined with three-dimensional morphology evaluation can be discussed and interpreted.

6 Conclusion and Outlook

With the ongoing development of steel and its increasing demands in applications, steel cleanliness has become an essential parameter for high-quality products. Due to the wide range of non-metallic inclusions influencing steels' performance positively and negatively, the field of particle analysis and cleanliness determination (see Chapter 2) has become an essential part of steel production and research. Knowledge about particles' formation and behavior is used to optimize process parameters, verify simulation models, and to develop new steelmaking concepts. One of the most common methods of the last decades with probably the most significant potential to support and further develop metallurgical research is SEM/EDS analysis. By quantifying macro to sub-micro sizes, spatial distributions, morphologies, and the precise determination of chemical composition, most critical parameters of non-metallic inclusions are determined manually or automated. The Ph.D. thesis's particular focus is on phenomena, limits, and potentials of SEM/EDS analysis for inclusion characterization. Selected aspects including electron interaction, particle cutting position, digital image recording, and evaluation of detected chemical and morphological data for various metallurgical demands are discussed and evaluated. The thesis's main findings include guidelines, formulated procedures, and developed equations clarifying distinct challenges:

- Fundamental considerations of sample interaction during SEM/EDS analysis study occurring phenomena and simulated electron interaction at non-metallic inclusion analysis for metallurgical tasks.
- A developed digital replica of automated non-metallic inclusion analysis examines theoretical influences of X-ray matrix interaction, preparation effects, and relative cutting positions of inclusions in case of cross-section analysis.
- A revised guideline considers particle sizes in the micrometer range allowing detailed quantification of solute or bonded matrix elements at manual analysis.
- Different defined procedures for dissolution experiments depending on the non-metallic inclusion population enable improved particle quantification and three-

dimensional morphology evaluation using electrolytic extraction, chemical extraction, or twin jet electro-polishing.

- Production of non-metallic inclusion standard and cross-section reference samples based on thermodynamics and kinetics describe an alternative referencing method of matrix interaction during automated measurements. 80 % of matrix interaction has been determined for 0.3 - 0.5 μ m (Fe,Mn)oxide inclusions using automated single point analysis. This is a very significant finding and should absolutely be considered for future inclusion characterization, especial in the sub-micro range.
- A formulated equation including consideration of matrix interaction for automated area scan settings is formulated based on particle sizes, morphology, and electron interaction simulation.
- Based on the gained knowledge in EDS phenomena, limits and potentials of non-metallic inclusion analysis, alternative particle classification and typification routines are developed. An optimized morphological categorization for digitalized inclusion images is formulated and enables improved determination of sphericity, angularity, irregularity, and elongation. By calculation of so called MF values, the inclusions' two-dimensional appearance is categorized by 10 distinctive morphology classes. Additionally, a new approach calculating particle nearest-neighbor relations based on automated SEM/EDS data is worked out for easy particle correlations and cluster identifications. Evaluation and interpretation of particles' chemical composition are improved by an adapted data correction procedure including consideration of measured artifacts, non-metallic partners, and a most objective inclusion typification.
- The newly established procedures and criteria are finally applied to different industry samples illustrating the manifold application and the benefits of the formulated evaluation procedures for divers metallurgical demands.

In the future, SEM operators, researchers, or quality engineers can use the formulated guidelines and procedures to optimize experiment conduction, inclusion analysis, and evaluation. Most essential innovations of the thesis achieved by fundamental research and new analysis approaches can be summarized as follows:

- The application of performed electron interaction simulations as easy-to-use measurement guidelines combined with equations dealing with matrix interactions improve metallurgical particle analysis on a fundamental basis.
- An extensively formulated procedure explains the production of non-metallic inclusion standard- and reference samples combined with electrolytic extraction,

which enables fundamental research of particles' compositions and morphology at sub-micro size ranges.

- The development of measurement guidelines and mathematical descriptions of matrix interaction during SEM/EDS analyses enables qualitative and quantitative correction of detected iron contents in inclusions.
- Formulated categorization guidelines for chemical and morphological classification generate an objective and size-independent evaluation of inclusions characteristics. Determining particle distance values for each particle enables the specification as a future performance indicator for steel cleanliness evaluations and cluster identification.

Considering the main findings, inclusion characterization has been essentially improved in different aspects. Guidelines and methodologies can selectively be used for varied metallurgical research and industry tasks. With further evaluation and interpretation of automated SEM/EDS data, new research areas can be established, and existing research topics will profit of the new possibilities in analysis and evaluation. Due to the still constantly increasing cleanliness requirements for steels and consequently decreasing sizes of the analysis's point of interest, the current work allows direct comparison of different particle size ranges and product groups. Especially in the upcoming field of data science, the current work has established a profound basis to subsequently use artificial intelligence and supervised machine learning programs to evaluate, interpret and discover new correlations in automated measurements' data in the field of inclusion metallurgy. Future research projects of metallurgists and material scientists will significantly benefit from the described approaches towards more efficient and comprehensible evaluations and interpretations.

Bibliography

- [1] McCance, A., *Non-metallic Inclusions: Their Constitution and Occurrence in Steel* (1918).
- [2] Holappa, L. and Wijk, O., *Inclusion Engineering, Industrial processes*, Elsevier, Amsterdam, 2014, pp. 347–372.
- [3] Wohrman, C., *Inclusions in Iron*, American O Society for steel treating (1928).
- [4] Benedicks, C. and Löfquist, H., *Non-metallic inclusions in iron and steel*, John Wiley & Sons Inc., New York, 1931.
- [5] Sims, C.E. and Lillieqvist, G.A., *Inclusions—Their Effect, Solubility and Control in Cast Steel*, *Trans. AIME* (1932), 100, pp. 154–195.
- [6] Costa e Silva, A.L.V., *The effects of non-metallic inclusions on properties relevant to the performance of steel in structural and mechanical applications*, *Journal of Materials Research and Technology* 8 (2019), 2, pp. 2408–2422.
- [7] Abbel, G. and Santillana, B., *Non-metallic Particles Benefit or Burden for AHSS*, *Advanced High Strength Steel*, Springer Singapore, Singapore, 2018, pp. 171–180.
- [8] Bhadeshia, H.K.D.H., *Steels for bearings*, *Progress in Materials Science* 57 (2012), 2, pp. 268–435.
- [9] Kaushik, P., Pielet, H. and Yin, H., *Inclusion characterisation – tool for measurement of steel cleanliness and process control: Part 2*, *Ironmaking & Steelmaking* 36 (2009), 8, pp. 572–582.
- [10] Zhang, L. and Thomas, B.G., *State of the Art in Evaluation and Control of Steel Cleanliness*, *ISIJ Int.* 43 (2003), 3, pp. 271–291.
- [11] Salgado, U. D., *Investigation of particle attraction by steel/refractory and steel/gas interfaces and the associated relevance for clogging in casting processes* (2018).

- [12] Salgado, U.D., Michelic, S., Bernhard, C., MPPE. Investigation of metallurgical phenomena related to process and product development by means of High Temperature Confocal Scanning Laser Microscopy, MPPE, Leoben, Austria (2015), 10.
- [13] Sasai, K. and Misukami, Y., Mechanism of Alumina to continuous caster nozzle reoxidation of molten steel, *ISIJ International* 41 (2001), 11, pp. 1331–1339.
- [14] Makino, T., Neishi, Y., Shiozawa, D., Kikuchi, S., Saito, H., Kajiwara, K. and Nakai, Y., Rolling Contact Fatigue Damage from Artificial Defects and Sulphide Inclusions in High Strength Steel, *Procedia Structural Integrity* 7 (2017), pp. 468–475.
- [15] Garrison, W.M. and Wojcieszynski, A.L., A discussion of the effect of inclusion volume fraction on the toughness of steel, *Materials Science and Engineering: A* 464 (2007), 1-2, pp. 321–329.
- [16] Murakami, Y., *Metal fatigue: Effects of small defects and nonmetallic inclusions*, first edition, Elsevier Science Ltd, Oxford, UK, 2002.
- [17] Sandaiji, Y., Tamura, E. and Tsuchida, T., Influence of Inclusion Type on Internal Fatigue Fracture under Cyclic Shear Stress, *Procedia Materials Science* 3 (2014), pp. 894–899.
- [18] Baker, T.J., Use of Scanning Electron Microscopy in Studying Sulphide Morphology on Fracture Surfaces, *Metallogr. Microstruct. Anal.* 5 (2016), 1, pp. 69–79.
- [19] Garrison, W.M. and Wojcieszynski, A.L., A discussion of the spacing of inclusions in the volume and of the spacing of inclusion nucleated voids on fracture surfaces of steels, *Materials Science and Engineering: A* 505 (2009), 1-2, pp. 52–61.
- [20] Bytyqi, A., Jenko, M. and Godec, M., Analysis of inclusions in spring steel using scanning electron microscopy and auger spectroscopy, *Vacuum* 86 (2012), 6, pp. 648–651.
- [21] Alvarez de Toledo, G., Influence of sulfur and Mn/S ratio on the hot ductility of steels during continuous casting, *Process Metallurgy, steel research* 64 (1993), 6, pp. 292-299.
- [22] Schmuki, P., Hildebrand, H., Friedrich, A. and Virtanen, S., The composition of the boundary region of MnS inclusions in stainless steel and its relevance in triggering pitting corrosion, *Corrosion Science* 47 (2005), 5, pp. 1239–1250.
- [23] Wang, Y., Cheng, G., Wu, W. and Li, Y., Role of inclusions in the pitting initiation of pipeline steel and the effect of electron irradiation in SEM, *Corrosion Science* 130 (2018), pp. 252–260.

- [24] Tervo, H., Kaijalainen, A., Pikkarainen, T., Mehtonen, S. and Porter, D., Effect of impurity level and inclusions on the ductility and toughness of an ultra-high-strength steel, *Materials Science and Engineering: A* 697 (2017), pp. 184–193.
- [25] Kundu, A., Austenite Grain Boundary Pinning during Reheating by Mixed AlN and Nb(C,N) Particles, *ISIJ Int.* 54 (2014), 3, pp. 677–684.
- [26] Moon, J., Lee, J. and Lee, C., Prediction for the austenite grain size in the presence of growing particles in the weld HAZ of Ti-microalloyed steel, *Materials Science and Engineering: A* 459 (2007), 1-2, pp. 40–46.
- [27] Wang, B., Liu, X. and Wang, G., Inclusion Characteristics and Acicular Ferrite Nucleation in Ti-Containing Weld Metals of X70 Pipeline Steel, *steel research int.* 89 (2018), 2, pp. 1700316.
- [28] Loder D., On the Formation Potential of Acicular Ferrite Microstructure in Different Steel Grades Focusing on the Influence of Carbon Content, *AISTEch* (2016), 10.
- [29] Ånmark, N., Karasev, A. and Jönsson, P.G., The Effect of Different Non-Metallic Inclusions on the Machinability of Steels, *Materials (Basel, Switzerland)* 8 (2015), 2, pp. 751–783.
- [30] Sui, H., Wang, L., Wang, Q., Wang, H., Che, D., Li, J. and Chou, K., The Formation and Growth of Sulfides in Free-Cutting Stainless Steel, *steel research int.* 89 (2018), 10, pp. 1800179.
- [31] Holappa, L. and Wijk, O., Chapter 1.7 - Inclusion Engineering, *Industrial processes*, Elsevier, Amsterdam, 2014, pp. 347–372.
- [32] You, D., Michelic, S. and Bernhard, C., Formation of Multi-Type Inclusions during the Cooling and Solidification of Steel: A Trend Model, *Metals* 8 (2018), 6, pp. 452.
- [33] You, D., Michelic, S.K., Wieser, G. and Bernhard, C., Modeling of manganese sulfide formation during the solidification of steel, *J Mater Sci* 52 (2017), 3, pp. 1797–1812.
- [34] You, D., Bernhard, C., Wieser, G. and Michelic, S., Microsegregation Model with Local Equilibrium Partition Coefficients During Solidification of Steels, *steel research int.* 87 (2016), 7, pp. 840–849.
- [35] Lehmann, J., Rocabois, P. and Gaye, H., Kinetic model of non-metallic inclusions' precipitation during steel solidification, *Journal of non-crystalline Solids* (2001), 282, pp. 61-71.

- [36] Wintz, M., Bobadilla, Lehmann, J. and Gaye, H., Experimental Study and Modeling of the Precipitation metallic Inclusions during Solidification of Steel, *ISIJ International*, Vol.35 (1995), No.6, pp.715-722.
- [37] Buck C., Computerbasierte Modellierung und Analyse der Gestalt und Verteilung von Partikeln zur Optimierung des Reinheitsgrades von Stahlwerkstoffen: Konzeption und Implementierung eines Rahmenwerks, Dissertation, 2016.
- [38] Beretta, S., Anderson, C. and Murakami, Y., Extreme value models for the assessment of steels containing multiple types of inclusion, *Acta Materialia* 54 (2006), 8, pp. 2277–2289.
- [39] Dilner, D., Mao, H. and Selleby, M., Thermodynamic assessment of the Mn–S and Fe–Mn–S systems, *Calphad* 48 (2015), pp. 95–105.
- [40] Park, J.H., Thermodynamic investigation on the formation of inclusions containing MgAl₂O₄ spinel during 16Cr–14Ni austenitic stainless steel manufacturing processes, *Materials Science and Engineering, A* 472 (2008), 1-2, pp. 43–51.
- [41] Jo, S.K., Song, B., and Kim, S.-H., Thermodynamics on the Formation of Spinel (MgOAl₂O₃) Inclusion in Liquid Iron Containing Chromium, *Metallurgical and materials transactions B*, Vol. 33B (2002), pp. 703-709.
- [42] Wang, G., Li, S., Ai, X., Zhang, C. and Lai, C., Characterization and Thermodynamics of Al₂O₃-MnO-SiO₂(-MnS) Inclusion Formation in Carbon steel billet (2016).
- [43] Sipola, T., Alatarvas, T., Heikkinen, E.-P. and Fabritius, T., Determination of Alloying Elements Ti, Nb, Mn, Ni, and Cr in Double-Stabilized Ferritic Stainless Steel Process Sample Using an Electrolytic Extraction Method and Separate Analysis of Inclusions, *Metall and Materi Trans B* 46 (2015), 4, pp. 1775–1781.
- [44] Anderson, C.W., Shi, G., Atkinson, H.V., Sellars, C.M. and Yates, J.R., Interrelationship between statistical methods for estimating the size of the maximum inclusion in clean steels, *Acta Materialia* 51 (2003), 8, pp. 2331–2343.
- [45] Turkdogan, E.T., *Fundamentals of Steelmaking*, The Inst. of Materials 298 (1996).
- [46] Turkdogan, E.T., Ladle deoxidation, desulphurisation and inclusions in steel - Part 1: Fundamentals, *Archiv für das Eisenhüttenwesen* 54 (1983), 1, pp. 1–10.
- [47] Flemings, M.C., Solidification processing, *Metall Mater Trans B* 5 (1974), 10, pp. 2121-2134.
- [48] Turkdogan, E.T., Microsegregation in steel, *J Iron Steel Inst* 208 (1970), 5, pp. 482-494.

- [49] Turkdogan, E.T., Causes and effects of deoxidation occurring during cooling and solidification of steel, *Trans TMS-AIME* (1965), 233.
- [50] Kaushik, P., Lehmann, J. and Nadif, M., State of the Art in Control of Inclusions, Their Characterization, and Future Requirements, *Metall and Materi Trans B* 43B (2012), 4, pp. 710–725.
- [51] Kawakami, M., Nishimura, T., Takenaka, T. and Yokoyama, S., Characterization of relieved non-metallic inclusions in stainless steel by image processing micrographs, *ISIJ International*, Vol39 (1999), 2, pp. 194-170.
- [52] Barbosa, C., Brant de Campos, J., Lopes do Nascimento, J. and Caminha, I.M.V., Quantitative Study on Nonmetallic Inclusion Particles in Steels by Automatic Image Analysis With Extreme Values Method, *Journal of Iron and Steel Research* 16 (2009), pp. 18-21.
- [53] Newbury, D.E., X-ray spectrometry and spectrum image mapping at output count rates above 100 kHz with a silicon drift detector on a scanning electron microscope, *Scanning* 5 (2005), 27, pp. 27-39.
- [54] Barcosa, C., Brant, J.C., Nascimento, J.L. and Caminha I.M.V., Quantitative Study on Nonmetallic Inclusion Particles in Steels by Automatic Image Analysis With Extreme Values Method, *Iron and Steel Research Int.* 16 (2009), 4, pp. 18–21.
- [55] Tang, D., Ferreira, M.E. and Pistorius, P.C., Automated Inclusion Microanalysis in Steel by Computer-Based Scanning Electron Microscopy: Accelerating Voltage, Backscattered Electron Image Quality, and Analysis Time, *Microscopy and microanalysis the official journal of Microscopy Society of America, Microbeam Analysis Society, Microscopical Society of Canada* 23 (2017), 6, pp. 1082–1090.
- [56] Müller, G., Stahnke, F. and Bleiner, D., Fast steel-cleanness characterization by means of laser-assisted plasma spectrometric methods, *Talanta* 70 (2006), 5, pp. 991–995.
- [57] Wang, H., Jia, Y., Li, Y., Zhao, L., Yang, C. and Cheng, D., Rapid analysis of content and particle sizes of aluminum inclusions in low and middle alloy steel by laser-induced breakdown spectroscopy, *Spectrochimica Acta Part B: Atomic Spectroscopy* 171 (2020), pp. 105927.
- [58] Hudson, S.W., Craparo, J., Saro, R. de and Apelian, D., Inclusion Detection in Aluminum Alloys Via Laser-Induced Breakdown Spectroscopy, *Metall and Materi Trans B* 49 (2018), 2, pp. 658–665.

- [59] Kuss, H.-M., Mittelstädt, H., Müller, G. and Nazikkol, C., Fast Scanning Laser-OES. I. Characterization of Non-metallic Inclusions in Steel, *Analytical Letters* 36 (2003), 3, pp. 659–665.
- [60] Atkinson, H.V. and Shi, G., Characterization of inclusions in clean steels: a review including the statistics of extremes methods, *Progress in Materials Science* 48 (2003), 5, pp. 457–520.
- [61] Bengtson, A., LIBS compared with conventional plasma optical emission techniques for the analysis of metals – A review of applications and analytical performance, *Spectrochimica Acta Part B - Atomic Spectroscopy* 134 (2017), pp. 123–132.
- [62] Kumar, D., Nuhfer, N.T., Ferreira, M.E. and Pistorius, P.C., Application of Plasma FIB to Analyze a Single Oxide Inclusion in Steel, *Metall and Materi Trans B* 50 (2019), 3, pp. 1124–1127.
- [63] Imashuku, S. and Wagatsuma, K., Rapid Identification of Calcium Aluminate Inclusions in Steels Using Cathodoluminescence Analysis, *Metall and Materi Trans B* 49 (2018), 5, pp. 2868–2874.
- [64] Cabalín, L.M., Mateo, M.P. and Laserna, J.J., Large area mapping of non-metallic inclusions in stainless steel by an automated system based on laser ablation, *Spectrochimica Acta Part B: Atomic Spectroscopy* 59 (2004), 4, pp. 567–575.
- [65] Atkinson, H.V. and Shi, G., Characterization of inclusions in clean steels: a review including the statistics of extremes methods, *Progress in Materials Science* 48 (2003), 5, pp. 457–520.
- [66] Takahashi, J. and Suito, H., Effect of omitting small sectioned particles with limited cross-sectional area on characterisation of secondary phase particles, *Materials Science and Technology* 18 (2002), 1, pp. 103–110.
- [67] Anderson, C.W., Shi, G., Atkinson, H.V. and Sellars, C.M., The precision of methods using the statistics of extremes for the estimation of the maximum size of inclusions in clean steels, *Acta Materialia* (2000), 48, pp. 4235–4246.
- [68] Kiessling, R. and N. Lange, Non-metallic inclusions in steel, United Kingdom. Iron and Steel Institute, 1968.
- [69] Bock, D.N. and Labusov, V.A., Determination of Nonmetallic Inclusions in Metal Alloys by the Method of Spark Atomic Emission Spectroscopy, *Inorg Mater* 55 (2019), 14, pp. 1415–1427.

- [70] Janis, D., Karasev, A. and Jönsson, P.G., Evaluation of Inclusion Characteristics in Low-Alloyed Steels by Mainly Using PDA/OES Method, *ISIJ Int.* 55 (2015), 10, pp. 2173–2181.
- [71] Pande, M.M., Guo, M., Dumarey, R., Devisscher, S. and Blanpain, B., Determination of Steel Cleanliness in Ultra Low Carbon Steel by Pulse Discrimination Analysis-Optical Emission Spectroscopy Technique, *ISIJ Int.* 51 (2011), 11, pp. 1778–1787.
- [72] Li, X.P., Choi, J., Kwon, O.D. and Yim, C., Investigation of inclusion detection by acoustic microscope, *Metals and Materials* 5 (1999), 3, pp. 241–249.
- [73] Sawafuji, Y., Automatic Ultrasonic Testing of Non-metallic Inclusions Detectable with Size of Several Tens of Micrometers Using a Double Probe Technique along the Longitudinal Axis of a Small-diameter Bar, *ISIJ Int.* 61 (2021), 1, pp. 248–257.
- [74] Wang, M., Bao, Y.P., Yang, Q., He, F., Wang, X.C., Ma, C. and Liang, Z.G., The Ultrasonic Detection of Macro-Inclusions in Steel, *AMR* 572 (2012), pp. 334–337.
- [75] Weinberg, M. and Meuser, H., Integrated Process- and Quality Control to Secure the Production of Slabs for Plates for Line Pipe Application, *Proceedings of the 11th International Pipeline Conference - 2016: Presented at 2016 11th International Pipeline Conference, September 26-30, 2016, Calgary, Alberta, Canada, Calgary, Alberta, Canada (2017).*
- [76] Weinberg, M. and Meuser, H., Integrated Process- and Quality Control to Secure the Production of Slabs for Plates for Line Pipe Application, *Proceedings of the 11th International Pipeline Conference - 2016: Presented at 2016 11th International Pipeline Conference, September 26-30, 2016, Calgary, Alberta, Canada, Calgary, Alberta, Canada (2017).*
- [77] Gorecki, C., Asundi, A.K., Osten, W., *Optical Micro- and Nanometrology IV, SPIE Photonics Europe, Brussels, Belgium (2012).*
- [78] Herwig, J., Buck, C., Thureau, M., Pauli, J. and Luther, W., Real-time characterization of non-metallic inclusions by optical scanning and milling of steel samples, *Optical Micro- and Nanometrology IV, Brussels, Belgium (2012), 843010.*
- [79] Schuermann, M., On the influence of non-metallic inclusions on HIC susceptibility of low carbon bainitic steels.
- [80] DIN, EN 10247:2017-09: Metallographische Prüfung des Gehaltes nichtmetallischer Einschlüsse in Stählen mit Bildreihen, Beuth Verlag GmbH, Berlin. doi:10.31030/2690587.

- [81] E04 Committee, Test Methods for Determining the Inclusion Content of Steel, ASTM International, West Conshohocken, PA. doi:10.1520/E0045-18A.
- [82] Gorkusha, D., Karasev, A.V., Komolova, O., Grigorovich, K.V. and Jönsson, P.G., Characterization of Non-metallic Inclusions and Clusters during Production of Low-carbon IF Steel, *ISIJ Int.* 60 (2020), 12, pp. 2819–2828.
- [83] Schützenhöfer, W., Tatzreiter, A., Plank, B. and Schumacher, P., Determination of cleanliness different special steels comparison of different methods, *iCT Conference* (2014), pp. 159–165.
- [84] Bandi, B., Santillana, B., Tiekink, W., Koura, N., Williams, M. and Srirangam, P., 2D automated SEM and 3D X-ray computed tomography study on inclusion analysis of steels, *Ironmaking & Steelmaking* 47 (2020), 1, pp. 47–50.
- [85] Shang, Z., Li, T., Yang, S., Yan, J. and Guo, H., Three-dimensional characterization of typical inclusions in steel by X-ray Micro-CT, *Journal of Materials Research and Technology* 9 (2020), 3, pp. 3686–3698.
- [86] Li, T., Shimasaki, S.-i., Taniguchi, S., Uesugi, K. and Narita, S., Particle Coagulation in Molten Metal Based on Three-Dimensional Analysis of Cluster by X-Ray Micro-Computer Tomography (CT), *ISIJ Int.* 53 (2013), 11, pp. 1958–1967.
- [87] Muhammad Nabeel, Michelia Alba, Andrey Karasev, Pär G. Jönsson and Neslihan Dogan, Characterization of Inclusions in 3rd Generation Advanced High-Strength Steels, *Metall Mater Trans B* 50 (2019), 4, pp. 1674–1685.
- [88] Faraji, M., Wilcox, D.P., Thackray, R., Howe, A.A., Todd, I. and Tsakiroopoulos, P., Quantitative Characterization of Inclusions in Continuously Cast High-Carbon Steel, *Metall and Materi Trans B* 46 (2015), 6, pp. 2490–2502.
- [89] Webler, B. A. and Pistorius, P. C., A Review of Steel Processing Considerations for Oxide Cleanliness, *Metall Mater Trans B* 51 (2020), 6, pp. 2437–2452.
- [90] Tuttle, R. and Song, K., Characterization of Rare Earth Inclusions from Cast 1010 Steel, *Inter Metalcast* 9 (2015), 1, pp. 23–31.
- [91] Goldstein, J.I., D.E. Newbury, J.R. Michael, N.W.M. Ritchie, J.H.J. Scott and D.C. Joy, *Scanning Electron Microscopy and X-Ray Microanalysis*, Springer, New York, NY, 2018.
- [92] Michelic S.K., Wieser, G. and Bernhard, C., On the Representativeness of Automated SEM/EDS Analyses for Inclusion Characterisation with Special Regard to the Measured Sample Area, *ISIJ Int.* 51(5): 769-775 (2011).

- [93] Mayerhofer, A., Michelic S.K. and Bernhard, C., Analyse von Fe,Mn-Oxiden mittels REM/EDX: Bringt die elektrolytische Extraktion was sie verspricht?, *Prakt.Met.Sonderband 53*, Dresden (2019), pp. 181–186.
- [94] Newbury, D.E. and Williams, D.B., The electron microscope: the materials characterization tool of the millennium, *Acta Materialia* 48 (2000), 1, pp. 323–346.
- [95] Newbury, D.E. and Ritchie, N.W.M., Electron-Excited X-ray Microanalysis by Energy Dispersive Spectrometry at 50: Analytical Accuracy, Precision, Trace Sensitivity, and Quantitative Compositional Mapping, *Microscopy and microanalysis the official journal of Microscopy Society of America, Microbeam Analysis Society, Microscopical Society of Canada* 25 (2019), 5, pp. 1075–1105.
- [96] Gao, S., Wang, M., Guo, J.-l., Wang, H., Zhi, J.-g. and Bao, Y.-p., Extraction, Distribution, and Precipitation Mechanism of TiN–MnS Complex Inclusions in Al-Killed Titanium Alloyed Interstitial Free Steel, *Met. Mater. Int.* 46 (2019), pp. 522.
- [97] Karasev A. and Glaser B., *Investigations of non-metallic inclusions and their behavior in the liquid steels and alloys*, 2019.
- [98] Bi, Y., Karasev, A. and Jönsson, P.G., Three-Dimensional Investigations of Inclusions in Ferroalloys, *steel research int.* 85 (2014), 4, pp. 659–669.
- [99] E04 Committee, *Practice for Electrolytic Extraction of Phases from Ni and Ni-Fe Base Superalloys Using a Hydrochloric-Methanol Electrolyte*, ASTM International, West Conshohocken, PA, 2010. doi:10.1520/E0963-95R10.
- [100] Preis, G. and Lennartz, G., Erfahrung bei der Isolierung von Schnellarbeitsstahlcarbiden sowie der Trennung von MC und M₆C, *Arch.Eisenhüttenwesen* 46 (1975), 8, pp. 509–514.
- [101] Fernandes, M., Cheung, N. and Garcia, A., Investigation of nonmetallic inclusions in continuously cast carbon steel by dissolution of the ferritic matrix, *Materials Characterization* 48 (2002), 4, pp. 255–261
- [102] Fernandes, M., and Garcia, A., Influence of refining time on nonmetallic inclusions in a low-carbon, silicon-killed steel, *Materials Characterization* 51 (2003), 4, pp.301-308
- [103] Reed, S.J.B. and Ware, N.G., Quantitative electron microprobe analysis using a lithium drifted silicon detector, *X-Ray Spectrom.* 2 (1973), 2, pp. 69–74.
- [104] Newbury, D.E., Mistakes Encountered during Automatic Peak Identification in Low Beam Energy X-ray Microanalysis, *Scanning* (2007), 29, pp. 137–151.

- [105] Ritchie, N.W.M., Newbury, D.E., Lowers, H. and Mengason, M., Exploring the limits of EDS microanalysis: rare earth element analyses, IOP Conf. Ser.: Mater. Sci. Eng. 304 (2018), pp. 12013.
- [106] Newbury, D.E., Mistakes encountered during automatic peak identification of minor and trace constituents in electron-excited energy dispersive X-ray microanalysis, Scanning 31 (2009), 3, pp. 91–101.
- [107] Newbury, D.E. and Ritchie, N.W.M., Is scanning electron microscopy/energy dispersive X-ray spectrometry (SEM/EDS) quantitative?, Scanning 35 (2013), 3, pp. 141–168.
- [108] Newbury, D.E. and Ritchie, N.W.M., Performing elemental microanalysis with high accuracy and high precision by scanning electron microscopy/silicon drift detector energy-dispersive X-ray spectrometry (SEM/SDD-EDS), Journal of materials science 50 (2015), 2, pp. 493–518.
- [109] Piños, J., Mikmeková, Š. and Frank, L., About the information depth of backscattered electron imaging, Journal of microscopy 266 (2017), 3, pp. 335–342.
- [110] Pistorius, P.C. and Verma, N., Matrix effects in the energy dispersive X-ray analysis of CaO-Al₂O₃-MgO inclusions in steel, Microscopy and microanalysis 17 (2011), 6, pp. 963–971.
- [111] Reischl, M., Frank, G., Augner, S., Lederhaas, B. and Michleic, S., Automated SEM/EDX Particle Analysis to Determinate Non-Metallic Inclusions in Steel Samples: Round Robin Tests Aiming at Studying the Comparability of Results from Different Measurement Systems, Praktische Metallographie 48 (2011), 12, pp. 649–659.
- [112] Winkler, W. and Angeli, J. Mayr, M., Automated SEM-EDX Cleanness Analysis and its Application in Metallurgy.
- [113] Tang, D., Ferreira, M.E. and Pistorius, P.C., Automated Inclusion Microanalysis in Steel by Computer-Based Scanning Electron Microscopy: Accelerating Voltage, Backscattered Electron Image Quality, and Analysis Time, Microscopy and microanalysis 23 (2017), 6, pp. 1082–1090.
- [114] Bartosiaki, B.G., Pereira, J.A.M., Bielefeldt, W.V. and Vilela, A.C.F., Assessment of inclusion analysis via manual and automated SEM and total oxygen content of steel, Journal of Materials Research and Technology 4 (2015), 3, pp. 235–240.
- [115] Lentz H.P., Potter, M.S. and Casuccio G.S., Detection, Measurement and Characterization of Inclusions Using Automated SEM Techniques Part 1: The Effects of Pixel Spacing, X-Ray Collection Time and Accelerating Voltage.

- [116] Nuspl, M., Wegscheider, W., Angeli, J., Posch, W. and Mayr, M., Qualitative and quantitative determination of micro-inclusions by automated SEM/EDX analysis, *Analytical and bioanalytical chemistry* 379 (2004), 4, pp. 640–645.
- [117] Izraeli, E.S., Tsach, T. and Levin, N., Optimizing FEG-SEM combined with an SDD EDX system for automated GSR analysis, *X-Ray Spectrom.* 43 (2014), 1, pp. 29–37.
- [118] Newbury, D.E. and Ritchie, N.W.M., Can X-ray spectrum imaging replace backscattered electrons for compositional contrast in the scanning electron microscope?, *Scanning* 33 (2011), 3, pp. 174–192.
- [119] Janis, D., Inoue, R., Karasev, A. and Jönsson, P.G., Application of Different Extraction Methods for Investigation of Nonmetallic Inclusions and Clusters in Steels and Alloys, *Advances in Materials Science and Engineering* (2014), 2, pp. 1–7.
- [120] Zheng, L., Malfliet, A., Wollants, P., Blanpain, B. and Guo, M., Effect of Alumina Morphology on the Clustering of Alumina Inclusions in Molten Iron, *ISIJ International* 56 (2016), 6, pp. 926–935.
- [121] Bommareddy, A. and Tuttle, R.B., Study of Electrolytic Dissolution in Steels and Rare Earth Oxide Stability, *Inter Metalcast* 10 (2016), 2, pp. 201–207.
- [122] Keller H., Die elektrochemischen Eigenschaften einiger Carbide im Hinblick auf ihre Isolierung aus Stählen_Keller, *Arch.Eisenhüttenwesen* 43 (1974), 9.
- [123] Baeumel, A. and Thomich, W., Über die Erprobung eines Salzsäure-Glykol-Elektrolyten für die Rückstandsisolierung bei chemisch beständigen Stählen, *Arch.Eisenhüttenwesen* 33 (1962), 2, pp. 91–101.
- [124] Zhang, X., Zhang, L., Yang, W. and Dong, Y., Characterization of MnS Particles in Heavy Rail Steels Using Different Methods, *steel research int.* 88 (2017), 1, pp. 1600080.
- [125] Inoue, R., Ueda, S., Ariyama, T. and Suito, H., Extraction of Nonmetallic Inclusion Particles Containing MgO from Steel, *ISIJ International* 51 (2011)), 12, pp. 2050–2055.
- [126] Lu, J., Wiskel, J.B., Omotoso, O., Henein, H. and Ivey, D.G., Matrix Dissolution Techniques Applied to Extract and Quantify Precipitates from a Microalloyed Steel, *Metall and Mat Trans A* 42 (2011), 7, pp. 1767–1784.
- [127] Zhang, X., Zhang, L., Yang, W., Wang, Y., Liu, Y. and Dong, Y., Characterization of the Three-Dimensional Morphology and Formation Mechanism of Inclusions in Linepipe Steels, *Metall and Materi Trans B* 48 (2017), 1, pp. 701–712.
- [128] Schickbichler M., Extraktion sulfidischer Einschlüsse aus Stahl, 2020.

- [129] Liu, Y., Zhang, L., Duan, H., Zhang, Y., Luo, Y. and Conejo, A.N., Extraction, Thermodynamic Analysis, and Precipitation Mechanism of MnS-TiN Complex Inclusions in Low-Sulfur Steels, *Metall and Mat Trans A* 47 (2016), 6, pp. 3015–3025.
- [130] Li, X., Wang, M., Bao, Y.P., Xing, L.D. and Chu, J.H., Characterization of 2D and 3D morphology of Al₂O₃ inclusion in hot rolled ultra-low carbon steel sheets, *Ironmaking & Steelmaking* 47 (2020), 4, pp. 437–441.
- [131] Doostmohammadi, H., Karasev, A. and Jönsson, P.G., A Comparison of a Two-Dimensional and a Three-Dimensional Method for Inclusion Determinations in Tool Steel, *steel research int.* 81 (2010), 5, pp. 398–406.
- [132] Park, J.H., Kim, D.-J. and Min, D.J., Characterization of Nonmetallic Inclusions in High-Manganese and Aluminum-Alloyed Austenitic Steels, *Metall and Mat Trans A* 43 (2012), 7, pp. 2316–2324.
- [133] Bi, Y., Karasev, A.V. and Jönsson, P.G., Evolution of Different Inclusions during Ladle Treatment and Continuous Casting of Stainless Steel, *ISIJ Int.* 53 (2013), 12, pp. 2099–2109.
- [134] Ryo Inoue, Rika Kimura, Shigeru Ueda and Hideaki Suito, Applicability of Nonaqueous Electrolytes for Electrolytic Extraction of Inclusion Particles Containing Zr, Ti, and Ce, *ISIJ Int.* 53 (2013), 11, pp. 1906–1912.
- [135] Brandner Karin, Isolation und Charakterisierung unterschiedlicher Karbidphasen in Stählen, Bachelorthesis, Leoben, 2019.
- [136] Voort, G.F.V., Metallographic Specimen Preparation for Electron Backscattered Diffraction Part I, *PM* 48 (2011), 9, pp. 454–473.
- [137] Echlin, P., Handbook of Sample Preparation for Scanning Electron Microscopy and X-Ray Microanalysis, Springer US, Boston, MA, 2009.
- [138] Pistorius, P.C., Patadia, A.: The steel matrix affects microanalysis of CaO-Al₂O₃-CaS inclusions, *Clean Steel* 8, Budapest, HU (2012), 12.
- [139] Hubbel J.H. and Stelzer, Tables of X-Ray Mass Attenuation Coefficients and Mass Energy-Absorption Coefficients, NIST Standard Reference Database 126, National Institute of Standards and Technology.
- [140] Saltykov, S.A., Stereometrische Metallographie, VEB Deutscher Verlag für Grundstoffindustrie, Leipzig, 1974.

- [141] Pistorius, P.C., Tang, D., Ferreira, M.E., Clean Steel 9 Consistency in automated inclusion analysis, Clean Steel 9, Hungary (2015), 8.
- [142] Pistorius, P.C., Patadia, A., Lee, J., AISTEch 2013 Proceedings Correction of Mtarix Effects on Microanalysis of Calcium Aluminate Inclusions, AISTech, USA (2013), 8.
- [143] Newbury, D.E., Mistakes Encountered during Automatic Peak Identification in Low Beam Energy X-ray Microanalysis, Scanning 29 (2007), 4, pp. 137-151.
- [144] Newbury, D.E. and Ritchie, N.W.M., Elemental mapping of microstructures by scanning electron microscopy-energy dispersive X-ray spectrometry (SEM-EDS): extraordinary advances with the silicon drift detector (SDD), J. Anal. At. Spectrom. 28 (2013), 7, pp. 973.
- [145] Warttinen, A.-M., Harju, M., Tamminen, S., Määttä, L., Alatarvas, T. and Röning, J., A tool for finding inclusion clusters in steel SEM specimens, Open Engineering 10 (2020), 1, pp. 642–648.
- [146] Seleznev, M., Wong, K.Y., Stoyan, D., Weidner, A. and Biermann, H., Cluster Detection of Non-Metallic Inclusions in 42CrMo4 Steel, steel research int. 89 (2018), 11, pp. 1800216.
- [147] Drouin, D., Couture, A.R., Joly, D., Tastet, X., Aimez, V. and Gauvin, R., CASINO V2.42: a fast and easy-to-use modeling tool for scanning electron microscopy and microanalysis users, Scanning 29 (2007), 3, pp. 92–101.
- [148] Pierre H., Dominique D. and Raynald G., CASINO: A new monte carlo code in C language for electron beam interaction —part I: Description of the program, Scanning 19 (1997), 1, pp. 1–14.
- [149] Österreicher, J.A., Grabner, F., Schiffli, A., Schwarz, S. and Bourret, G.R., Information depth in backscattered electron microscopy of nanoparticles within a solid matrix, Materials Characterization 138 (2018), pp. 145–153.
- [150] Takahashi, J, and Suito, H., Evaluation of the Accuracy of the Three-Dimensional Size Distribution Estimated from the Schwartz–Saltykov Method, Metallurgical and Materials Transactions A 34 (2003), pp. 171-181
- [151] Fernandes, M., Cheung, N. and Garcia, A., Investigation of nonmetallic inclusions in continuously cast carbon steel by dissolution of the ferritic matrix, Materials Characterization 48 (2002), 4, pp. 255–261.
- [152] Rivas, A.L., Vidal, E., Matlock, D.K. and Speer, J.G., Electrochemical extraction of microalloy carbides in Nb-steel, Rev. metal. 44 (2008), 5.

- [153] Verma, N., Pistorius, P.C., Fruehan, R.J., Potter, M., Lind, M. and Story, S., Transient Inclusion Evolution During Modification of Alumina Inclusions by Calcium in Liquid Steel: Part I. Background, Experimental Techniques and Analysis Methods, *Metall and Materi Trans B* 42 (2011), 4, pp. 711–719.
- [154] Kim, H.S., Lee, H.-G. and Oh, K.-S., MnS precipitation in association with manganese silicate inclusions in Si/Mn deoxidized steel, *Metall and Mat Trans A* 32 (2001), 6, pp. 1519–1525.
- [155] Booker, G.R., Norbury, J. and Sutton, A.L., X-ray diffraction studies on precipitates and inclusions in steels using an extraction replica technique, *Br. J. Appl. Phys.* 8 (1957), 4, pp. 155–157.
- [156] Luo, Y., Yang, W., Ren, Q., Hu, Z., Li, M. and Zhang, L., Evolution of Non-metallic Inclusions and Precipitates in Oriented Silicon Steel, *Metall and Materi Trans B* 49 (2018), 3, pp. 926–932.
- [157] Fischer, W.A. and Fleischer, H.J., Die Reaktionen von manganhaltigem Eisen mit seinen Oxyden im Kalktiegel bei 1600 bis 1800°C, *Archiv für Eisenhüttenwesen* 32 (1961), 6, pp. 305–313.
- [158] Steinmetz, E. Oxidmorphologie bei Mangan- und Mangan-Silizium-Desoxidation, *Arch.Eisenhüttenwesen* 47 (1976), 2 Februar, pp. 71–76.
- [159] Steinmetz, E. and Lindenberg, H.U., Morphologie der Einschlüsse bei der Desoxidation mit Aluminium, *Arch.Eisenhüttenwesen* 47 (1976), pp. 189–204.
- [160] Steinmetz E. and Andreae C., Einfluss des Sauerstoffs auf die Ausbildung von Aluminiumoxiden, *steel research int.* 62 (1991), 2, pp. 54–59.
- [161] You, D., Michelic, S.K., Bernhard, C., Loder, D. and Wieser, G., Modeling of Inclusion Formation during the Solidification of Steel, *ISIJ International* 56 (2016), 10, pp. 1770–1778.
- [162] Ohnaka, I., Mathematical Analysis of Solute Redistribution during solidification with diffusion in Solid Phase, *ISIJ Transactions* 26 (1986), pp. 1045–1051.
- [163] Mayerhofer, A., You, D., Presoly, P., Bernhard, C. and Michelic, S.K., Study on the Possible Error Due to Matrix Interaction in Automated SEM/EDS Analysis of Nonmetallic Inclusions in Steel by Thermodynamics, Kinetics and Electrolytic Extraction, *Metals* 10 (2020), 7, pp. 860.
- [164] Piskernik, J.E., Implementierung der Nahrungsbeziehung nichtmetallischer Einschlüsse zur erweiterten Analyse automatisierter REM/EDX, *Bachelorthesis, Leoben, 2021.*

Acronyms

AScan	Area scan
AScan	Area scan
BE	Backscattered electrons
CPM	Center-point-distance
CrNi	Chromium-Nickel-Steel
CS	Cross section
CT	Computer tomography
e ^{-prim}	Primary electrons
e ^{-prim*}	Primary electrons interacting with the material
EBSD	Electron backscattered diffraction detector
ECD	Equivalent circle diameter
EDS	Energy dispersive spectrometry
EEM	Edge-to-edge distance
FET	Feature Evaluation Tool
HFR	High frequency remelter
LC	Low carbon steel
LED	Lower electron detector
MF	Morphology factor
N	Nitride
NMI	Non-metallic inclusions
NS	Nitride-Sulfide
O	Oxide
OES	Optical emission spectrometry
OM	Optical microscope
ON	Oxide-Nitride
ONS	Oxide-Nitride-Sulfide
OPS	Oxide polish suspension
OS	Oxide-Sulfide
PC	Probe current
PDA	Pulse discrimination analysis
PP	Process parameter
PScan	Point scan
RBED	retractable backscattered electron detector
S	Sulfide
SE	Secondary electrons

SEM	Scanning electron microscope
SiC	Silicon carbide
STD	Standard
UED	Upper electron detector
US	Ultra sonic
VIM	Vacuum induction melting
WDS	Wavelength dispersive spectroscopy
X-ray	Röntgen radiation

List of Parameters

Δ	Delta
A	Absorption coefficient
A1	Boltzmann constant A1
A2	Boltzmann constant A2
b^{Fe}	Interaction width
c	Continuum
C_{std}	Concentration of the standard
C_{unk}	Concentration of the unknown
d	Apparent inclusion size
D	Actual inclusion size before sectioning
E^{depth}	Element content caused by depth interaction
E^{depth^*}	Element content caused by depth interaction after First correction without normalization
E^{EDS}	Detected Element content
E^{Matrix}	Matrix Element content
E^{NMI}	Actual Element content
E^{ring}	Element content caused by ring interaction
E^{ring^*}	Element content caused by ring interaction after First correction without normalization
F	Inner-shell ionization parameter
f^{s}	Solid fraction
h	Corresponding cutting height
I	Transmitted intensity
I_0	Initial intensity
I^{cum}	cumulative intensity
I_{s}	Intensity share
I_{std}	Intensity in the standard
I_{unk}	Intensity in the unknown
k	Intensity ratio
$K\alpha$	K-alpha radiation

L	Attenuation Length
L α	L-alpha radiation
M α	M-alpha radiation
V ^{nmi}	Corresponding volume inside inclusion
V _r	Volume ratio
V ^{ring}	Corresponding volume around the inclusion
Z	Particle depth
Z ^a	Atomic number
Z ^{Fe}	Interaction depth
Λ	Radiation type

List of Tables

Table 1: Constituent mass ratio classification [104]	7
Table 2: Analysis parameters for micro cleanness evaluations at the Chair of Ferrous Metallurgy	12
Table 3: Electrolytes and non-metallic inclusions extracted for research demands.	16
Table 4: Overlapping peaks problematic at automatic peak identification [106,143].....	23
Table 5: Calculated interaction depth depending on particle composition and density at 15kV.....	41
Table 6: Predicted wt% FeO composition ranges (10 K/s).....	53
Table 7: NMI populations in Mn deoxidized melts	55
Table 8: Application and results of ring correction.....	63
Table 9: Interaction depth correction	65
Table 10: MF values for elongated inclusions.	70
Table 11: Morphology factors (MF) for spherical inclusions	70
Table 12: MF values calculated for different (Fe,Mn)oxide populations.	71
Table 13: Data post-processing: correction criteria low, med, and high alloyed steels.	76
Table 14: General inclusion classification criteria.....	77
Table 15: Result of automated inclusion analysis.	78
Table 16: Typification of non-metallic inclusions.	80
Table 17: Industry steel samples for improved particle analysis.	84
Table 18: Data post-processing: simple correction criteria for carbide steels with low Si contents	122

Table 19: Examples of different morphologies and resulting MF-factors..... 122

Table 20: Essential parameters for automated inclusion analysis..... 123

Table 21: Input parameters for electron and X-ray interaction simulation 124

Table 22: Densities of non-metallic phases 124

List of Figures

Figure 1: Most established instruments steel cleanliness evaluations.....	5
Figure 2: Relative errors at non-standard analysis [108].....	9
Figure 3: JEOL 7200F system and illustration of gathered information during NMI analysis.....	10
Figure 4: Greyscale quantification and threshold setting.....	12
Figure 5: Concentration mapping of a heterogeneous (Al, Mg)oxide – (Ca, Mn, Mg)sulfide inclusion.	13
Figure 6: Comparison of electron interaction for cross-section and for extraction samples.	14
Figure 7: Different extraction methods for steels non-metallic inclusions [119].....	14
Figure 8: Local topography affecting EDS results [107].	18
Figure 9: Intensity depending on attenuation length in Fe matrix according to [138].	18
Figure 10: Increasing steel matrix interaction with decreasing particle size.	19
Figure 11: Different cutting position influencing EDS output.	20
Figure 12: Greyscale features and artifacts at automated SEM/EDS analysis.....	21
Figure 13: a) Suboptimal pixel limit b) Coarsening of inclusions appearance [115].	22
Figure 14: PScan and AScan settings creating different interaction volumes.	24
Figure 15: Detected particles' iron content for different scan parameters.....	24
Figure 16: Influence of the present work on metallurgical inclusion analysis by means of SEM/EDS.....	26
Figure 17: Parameters affecting the output of non-metallic inclusion analysis.	29

Figure 18: Simulated electron and X-ray interaction for 15KV in pure iron.....	30
Figure 19: Characteristic X-ray intensity according to interaction depth z.....	31
Figure 20: X-ray interaction for typical non-metallic inclusions in steels.....	32
Figure 21: Illustration of two-dimensional NMI layer assumption and interaction.....	33
Figure 22: X-ray interaction for a 500 nm thick NMI layer.	33
Figure 23: Intensity splits depending on particle composition and depth.	34
Figure 24: Volumetric spheres and cutting procedure determining characteristic geometry parameters.....	36
Figure 25: Imaging step and threshold definition and voxel generation.	36
Figure 26: Implementation of X-ray interaction and intensity decrease.....	37
Figure 27: Voxels' mean value generation.....	37
Figure 28: Comparison of simulated and measured EDS results.....	38
Figure 29: Favoured cutting position depending on inclusion size.	40
Figure 30: Minimum particle size avoiding matrix interaction for single-point analysis.....	42
Figure 31: Detected composition at single point analysis at Al ₂ O ₃ particles.	43
Figure 32: Installation for electrolytic extraction and filtrate processing.	44
Figure 33: Electrolytic extracted non-metallic inclusions enabling exceptional particle analysis.....	45
Figure 34: Oxidic inclusions with dissolved sulfide regions resulting in dimples and missing phases.....	46
Figure 35: Methodology of sequential chemical extraction.....	46
Figure 36: Clustered and complex sulfide inclusions after sequential chemical extraction.	47
Figure 37: (Mn)OS inclusion in cross-section and sequential chemical extraction.....	47
Figure 38: NMI still attached to extraction sample.....	48
Figure 39: Particles with dissolved or lost MnS.	48
Figure 40: EDS concentration mapping at 10kV.	49
Figure 41: Twin jet polished sample in different magnifications.	50

Figure 42: Phase diagram and Mn oxide morphology depending on oxygen activity. [157,158].....	52
Figure 43: Calculated Fe segregation effects during solidification.	52
Figure 44: Methodology of NMI reference and standard sample production.....	54
Figure 45: Calculated and measured FeO contents.....	56
Figure 46: Morphologies of CS and STD samples depending on Mn/O ratio.....	58
Figure 47: Referencing cross-section and extracted compositions detected [163].	59
Figure 48: Considered matrix interaction at area scan measurements.	60
Figure 49: reduced interaction dimensions.....	61
Figure 50: Detected and corrected particle composition.	63
Figure 51. Concentration ranges at the correction of matrix interaction.	66
Figure 52: Detected Fe contents compared to electrolytic extraction and mathematical correction.	67
Figure 53: 1) Imaging, 2) Greyscale threshold application, 3) Binary imaging, 4) Illustration of edge coarsening caused by binarization.	69
Figure 54: MF categorization with increasing Mn/O ratio.	72
Figure 55: Center point distance and edge-to-edge distance.....	73
Figure 56: Illustration of edge-to-edge approximation.	74
Figure 57: Possible nearest-neighbor relations.	74
Figure 58: Relative distance relation based on particle size.....	75
Figure 59: General classification of LC sample.	78
Figure 60: Reinterpretation of inclusion population according to non-metallic bonding partners.....	80
Figure 61: Element mapping of heterogeneous oxide-sulfide inclusion.	81
Figure 62: Improved inclusion classification for further categorization.	81
Figure 63: XY-distribution of different classification categories.	82
Figure 64: NMI population in different analysed steel samples.	85
Figure 65: Ternary system of Al, Mg, and Ca containing inclusions.....	86

Figure 66: Element concentration mapping of a (Ti,Al)ON inclusion.....	87
Figure 67: Element concentration mapping of an extracted (TiAl)ON inclusion.	88
Figure 68: Morphology evaluation LC-A and LC-B samples.....	89
Figure 69: Morphology evaluation CrNi-A and CrNi-B samples.	89
Figure 70: Nearest-neighbor (NN) distribution of LC-A and LC-B samples.....	90
Figure 71: Nearest-neighbor (NN) distribution of CrNi-A and CrNi-B samples.....	91
Figure 72: Evaluation of clustering by 150% ECD threshold for nearest-neighbor distances.....	92
Figure 73: Composition Range (FeMn)S inclusions.	93
Figure 74: Composition range TiN inclusions.....	93

A Appendix

Background information of different sections according to their order of appearance.




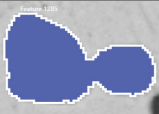


A.1 Data correction for carbide steels

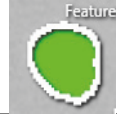




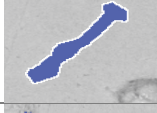









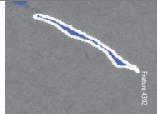

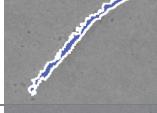

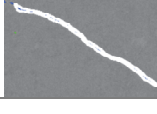
Table 18: Data post-processing: simple correction criteria for carbide steels with low Si contents

Artifact type	Criterion
Polishing residues	$F + Na + Cl + P + K > 0$.
Grinding residues	$Si > 1.5\%$
Carbide matrix I	$Al+Mg+Ca+Ti+Nb = 0$ & $O+N+S = 0$; "
Carbide matrix II	$Al+Mg+Ca+Ti+Nb = 0$ & $O+N+S > 0$;
Insufficient measurements	$Al+Mg+Ca+Ti+Nb > 0$ & $O+N+S = 0$.

A.2 Morphology Parameters

Table 19: Examples of different morphologies and resulting MF-factors

Spherical	MF1	MF2	MF3	Elongated	MF1	MF2	MF3
Spherical < 21pxl				Slightly elongated			
	-0,16	-0,06	-0,16		0,33	0,72	1,67
circular				slightly elongated and irregular			
	0,002	0,005	0,01		0,30	1,8	5,18
	0,004	0,01	0,03		0,69	4,70	15,61

	0,059	0,15	0,44		0,5	3,38	12,13
angular			elongated				
	0,03	0,24	0,70		1,26	6,74	14,66
	0,06	0,51	1,41		0,85	7,39	17,51
	0,11	0,67	1,93		2,0	26,8	59,53
angular and irregular			elongated and irregular				
	0,25	1,38	4,08		2,07	19,31	90,75
	0,35	1,87	5,87		1,14	22,33	97,06
	0,74	4,83	18,3		5,14	27,25	103,88
spherical and highly irregular			highly elongated or irregular				
	0,88	10,31	48,8		2,85	30,01	63,11
	1,25	12,79	66,69		3,22	50,59	137,91
	5,22	21,69	162,22		4,48	112,91	236,58

A.3 SEM/EDS Parameters

Table 20: Essential parameters for automated inclusion analysis

General Information			
Chemical composition	-	[%]	
Measured area	~100	[mm ²]	
Termination criterion	8	[h]	
parameter microscope		parameter analysis	
acc. voltage	15	[KV]	resolution 2048 [pxl]

current	13 [PC]	ECD-range	1-max [μm]
process parameter	4 [-]	pxl/feature	9 [pxl]
downtime	25-30 [%]	magnification	200 [-]
counts IN	40000 [cps]	measuring time/particle	3 [s]
counts OUT	30000 [cps]	Grey scale treshhold	20000 [-]

A.4 Casino Simulation

Table 21: Input parameters for electron and X-ray interaction simulation

Edit Layers Options	
Used substrates	Multi-layer
Microscope and Simulation Properties	
KeV Start	15
Number electrons simulated	2000
Conserve data for each simulated point	yes
Distributions min/max	Auto
Distribution of maximum depth of electrons	1000
Distribution of the energy of backscattered electrons (BE)	500
Distribution of the energy of transmitted electron	500
Distribution of surface radius (BE)	500
Distribution of the backscattered electron angle	91
Distribution of the backscattered electron angle VS their energy	91
Max Range Parameters	simulated
Distribution of energy by position	X=50, Y=50, Z=50
Generate X-ray	Yes 500
Options	
Number of displayed trajectories	2000
Time between backups	5 min
Minimum electron energy	0.05keV
Conserve electron trajectory	Displayed only
Selected Physical Model	
Total Cross Section	Mott by Interpolation
Partial Cross Section	Mott by Interpolation
Effective Sunction Ionisation	Casnati
Ionisation Potential	Joy and Luo [1989]
Random Number Generator	Press et al. [1986]
Directing Cosin	Drouin [1996]
dE/dS Calculation	Joy and Luo [1989]

Table 22: Densities of non-metallic phases

NMI	CaS	MgO	Al2O3	MnS	MnO	TiN	AlN	Mn2O3	Ti2O3
[g/cm³]	2.8	3.58	3.94	3.99	5.45	5.22	3.6	4.5	4.49